analytical chemistry

pubs.acs.org/ac

Review

Raman Spectroscopy and Imaging in Bioanalytics

Dana Cialla-May, Christoph Krafft, Petra Rösch, Tanja Deckert-Gaudig, Torsten Frosch, Izabella J. Jahn, Susanne Pahlow, Clara Stiebing, Tobias Meyer-Zedler, Thomas Bocklitz, Iwan Schie, Volker Deckert, and Jürgen Popp*

Cite This: *Anal. Chem.* 2022, 94, 86−119

Read Online

CONTENTS

Since the discovery of the inelastic scattering of light, i.e., the so-called Raman effect,[1] Raman spectroscopy has become an attractive tool in a high number of research fields including biology, chemistry, and medicine. The use of lasers as an excitation source and the combination of Raman spectroscopy with microscopes have dramatically increased the applicability for bioanalytical questions and research tasks since the 1970s, which has been accompanied by the system development and product launch of Raman microspectroscopic devices.[2] In particular, the Raman spectroscopic investigation of the protein lysozyme nicely demonstrates the development of this technique in bioanalytics.[3] In 1958, the first Raman spectrum of the biopolymer lysozyme was published showing 14 faint lines, recorded by using a mercury source excitation. Ten years later, 21 modes were identified using laser Raman spectroscopy. In 1970, a study was published to assign and interpret the origin of the modes in the Raman spectrum of native lysozyme by comparison with spectra obtained from mixtures of the constituent amino acids.[4] Since the early development of laser-excited Raman spectroscopy, this technique and its variants have proven to be a powerful tool in bioanalytics. Initially, pure substances and biomolecules were investigated. Step by step, the samples studied gained complexity, achieving Raman spectroscopic characterization of cells and tissue, identification of bacteria on the strain level and tumor margins, and detection of low molecular weight substances in body fluids.

The aim of this Review is to provide the interested reader detailed information and necessary knowledge to decide on the most promising Raman-based analytical detection scheme for

Special Issue: Fundamental and Applied Reviews in Analytical Chemistry 2022

Published: December 17, 2021

https://doi.org/10.1021/acs.analchem.1c03235
Anal. Chem. 2022, 94, 86−119

the specific planned application scenario. Thus, we address young researchers and beginners in the field approaching the topic of Raman spectroscopy and encourage the pursuit of Raman-based techniques in bioanalytics. As not every spontaneous and coherent Raman-based technique combines all advantages in a single method, the researcher must decide on the most appropriate analytical approach to address the specific analytical question. Therefore, in Raman Spectroscopy and Related Techniques, the theoretical background of Raman spectroscopy and related techniques is provided.

Chemistry, physics, materials sciences, mineralogy, art and archeology, biology, biochemistry, and pharmacy as well as biomedicine are mentioned as applied fields of Raman spectroscopic approaches, which illustrates the huge potential of this method in (bio)analytics.[5] To understand the development of diseases, Raman spectroscopy and its variants are applied in cancer diagnosis to detect tumor markers, to investigate body fluids, to characterize cell lines, and to monitor tissue samples.[6] This provides molecular information that allows one to correctly identify tumor margins in tissue or a cancer noninvasively. In addition to the development of powerful and portable Raman spectrometers suitable for use in a clinical environment, the generation of comprehensive databases in combination with data analysis tools is important for a successful translation of Raman spectroscopic approaches into clinics. In the case of cardiovascular diseases, Raman-based techniques are used to detect biomarkers as well as to investigate cells and tissues up to the organ level, i.e., the heart.[7] As another example of an application, Raman spectroscopy and its variants are used in the study and diagnosis of neurodegenerative diseases, which are associated with conformational changes, as Raman spectroscopy is sensitive to such structural changes and post-translational modifications of proteins.[8] Raman spectroscopy further demonstrated its potential in the field of malaria.[9] Here, monitoring biological processes of the parasite and the interaction with antimalarial drugs is summarized. Vibrational spectroscopic methods have gained importance for the analysis of body fluids such as urine, tear fluid, blood, or saliva. However, as those body fluids have a mixed composition, standardized sample collection and pretreatment protocols as well as detection procedures have to be developed to enable the translation into clinical practice.[10] Surface enhanced Raman spectroscopy (SERS) is known as a powerful analytical method to investigate and identify bacteria in clinical biochemistry.[11] Other popular and promising Raman-based approaches are the determination of the antioxidant status in humans by resonance Raman (RR) spectroscopy of carotene in skin,[12] which has already been commercialized as the Pharmanex BioPhotonic Scanner in 2003, and the near real-time intraoperative assessment of brain tumors by stimulated Raman scattering (SRS) microscopy, where convolution neural networks have already been trained on over 2.5 million images.[13] We summarize the application in bioanalytics starting from low molecular weight substances followed by biomacromolecules, viruses, bacteria, and cells up to tissue and organs in Application in Bioanalytics. It is shown that a large number of bioanalytical tasks and questions can be addressed with Raman-based techniques, as they provide molecular and chemical structural information at different levels of lateral resolution and sensitivity.

All discussed applied fields of Raman spectroscopy and its variants have the following in common: a database in combination with suitable data analysis tools is of great importance to ensure a translation into clinical application in the future.[14] Therefore, in Data Analysis Concepts in Raman-Based Methods in Biophotonics, the data analysis concepts of Raman-based methods will be introduced. Finally, the Conclusion and Outlook will summarize the discussion and will provide an outlook.

RAMAN SPECTROSCOPY AND RELATED TECHNIQUES

Linear, Spontaneous Raman-Spectroscopic Techniques. When an incident photon interacts with a crystal lattice or molecule, it can be scattered either elastically or inelastically. The inelastic scattering of light by matter is known as the Raman effect. In the first approximation of the theory, the Raman process is spontaneous and depends linearly on the intensity of the exciting monochromatic light. For the measurement of either very small or heterogeneous samples with a high spatial resolution, a Raman setup is coupled to an optical microscope. Here, the objective lens is used to focus the laser light on the sample, and the scattered light is collected by the same objective lens and then analyzed with a spectrometer and a detector, usually a CCD.[2] A laser line filter cleans up the monochromatic excitation light from laser plasma lines or Raman signals generated in the excitation fiber core. A long pass or Notch filter in the collection path suppresses the elastic, Rayleigh scattered light. In principle, all excitation wavelengths can be used. However, excitations in the UV (below 400 nm) or the NIR region (above 800 nm) require special optical components. When one focuses a visible excitation laser light through a microscope objective lens, it usually allows for a lateral resolution below 1 μm and an axial resolution of approximately 3 μm.[15]

Larger sampling areas up to centimeters can be analyzed with several approaches. A simple approach is to expand the laser focus or to move the laser focus during signal acquisition. Another possibility is point-by-point mapping, where the sample is moved under the laser or the laser is scanned over the fixed samples followed by measuring a complete Raman spectrum at every position. In the serial point mapping acquisition mode, the total time depends on the number of measurement positions times the integration time per measurement point. All in all this might lead to analysis times of several hours or for large samples even days. The spatially resolved data sets are arranged in a data matrix. Either univariate information such as the intensity or the wavenumber maximum of a Raman band is displayed via the analysis area or areas of similar composition are displayed in a false color by multivariate chemometric methods.[16]

More advanced and faster Raman techniques use laser line, light sheet, or wide-field illumination with dedicated signal collection schemes. Line illumination would allow one to measure the y direction simultaneously, whereas the x direction will still be mapped. The spectral separation of the y direction is then performed line wise on the CCD, which might also enhance the spatial resolution in this direction.[16] In global or wide-field imaging, the complete area is illuminated by the excitation laser. The desired spectral range of the scattered light is selected with a filter element instead of a spectrometer. The scattered light is then focused on the CCD with an image conserving optic, whereby the intensity of the selected spectral range per pixel element is read out. This leads to a very high spatial resolution with shorter measurement times, but the spectral resolution is often reduced by the selected filter elements.[16] All three approaches can then be combined with a z moving element like a

https://doi.org/10.1021/acs.analchem.1c03235
Anal. Chem. 2022, 94, 86−119

piezo to measure other planes of the samples and establish a 3D cube.

To enhance the spatial resolution of a Raman experiment, a confocal Raman microscope with a high numerical aperture objective lens above 0.9 can be used. In such a setup, a confocal aperture is placed at the back focal plane. As this aperture blocks out of focus signals, only signals in a very small sample volume can be registered by the detector. This leads to a better effective axial spatial resolution and to some extent also improves the lateral resolution. Nevertheless, blocking a part of the scattered light also leads to a significant loss in the signal-to-noise ratio, which most of the time needs to be compensated by using higher laser intensity or longer integration times. In addition, the effective axial resolution changes depending on the focus depth inside the sample.[15]

In addition to coupling to microscopes, Raman spectrometers can be coupled to fiber optic probes. Whereas the coupling of lasers and spectrometers to fiber optic cables offers convenient alignment and low losses compared to the guidance via a series of mirrors, all optical components that are used in the beam path of the microscope such as the laser line filter, long pass/Notch filter, and lenses need to be integrated into the probe head. The integration is challenging for miniaturized probes with a small diameter for insertion in the working channel of the endoscopes. Other requirements of biomedical fiber optic Raman probes for *in vivo* application are flexibility and sterilizability. Several fiber probe designs have been developed for *in vivo* applications within the last few years.[17] Relatively simple hand-held Raman probes use one excitation fiber and one collection fiber with beam steering components, filters, and a lens to focus the laser light and collect the Raman scattered light. More sophisticated Raman probes arrange multiple collection fibers around a central excitation fiber, and the collection fiber cores are aligned along the entrance slit of the spectrometer.[18] Without a lens at the probe tip, the laser excitation light is emitted divergently and the illuminated sample area does not overlap well with the detection area. Beveled fibers,[18,19] a ball lens,[20−22] or a two-component converging lens[23] are introduced into the probe tip to improve the laser focus and signal detection, which further increases the complexity of the optical layout. Usually, the signal from all fiber cores is binned at the CCD detector and only a single spectrum is obtained at each sampling position. Images can be registered by sequential acquisition of Raman spectra and moving the sample or the probe. Recently, the position of the probe was tracked by a computer vision-based assessment system upon continuous registration of Raman spectra.[24] The resulting Raman image was projected onto a photo of the sample toward augmented chemical reality. Raman probes with multiple fibers have also been combined with complementary modalities such as fluorescence lifetime imaging[25] and narrow band imaging[26] or have included autofluorescence imaging and white light reflectance imaging.[27] Another technique, Raman hyperspectral imaging, was presented that allows one to capture an entire Raman image with only one exposure.[28] Key elements were an array of 20 × 20 fibers, arrangement of 400 fiber cores in one row as a pseudoslit, and a fiber coupled integral field spectrograph with a large (4096 × 4096 pixel) CCD. The pitch between the fiber centers was 0.5 mm, resulting in a sampling area of 9.5 × 9.5 mm^2. As the laser excitation intensity is distributed over 400 cores, higher intensities can be applied without inducing laser-induced damages. Microstructured hollow core fibers were suggested as the excitation because the laser is guided in air, which avoids the generation of background signals from the fiber core.[29,30] Consequently, a filter for laser cleanup is not required anymore in the probe tip.

A variation of Raman fiber approaches also uses microstructured hollow core fibers.[31,32] The principle is that the liquid[33] or gaseous analytes[34,35] are filled in the central fiber hollow core, the excitation light is guided with low attenuation, and the generated Raman signals are guided back also with low losses. Thus, the laser light interacts with the analyte molecules very efficiently over an extended path length, and the number of scattering molecules that contribute to the Raman signal is strongly increased in comparison to the small conventional scattering volume.[33] The hollow fiber also acts as a miniaturized sample container with significantly reduced sample demand.[33] Fiber enhanced Raman spectroscopy (FERS) was exploited for the monitoring of small molecules (biomarkers and drugs) in gases[36−38] and in liquids[39−46] with an emphasis on body fluids.[47] Microstructured sensor fibers provide a filigree network of thin silica bridges in the cladding region to achieve light guidance in the central hollow core.[32] In order to develop an optimized sensor fiber for the analysis of gases and liquids, various approaches were discovered to account for the differences in refractive indices. For FERS of gaseous biomarkers, novel developments of photonic crystal fibers[35,48] and kagome fibers[37,49] have been exploited and the performance of the sensor fiber was evaluated.[50] To achieve light guidance in aqueous media and body liquids, liquid samples were filled into the fiber core and, thus, the fiber had to be specially prepared.[40,41,45,47,51]

Resonance Raman Spectroscopy. Resonance Raman (RR) spectroscopy utilizes the frequency dependence of the polarizability to enhance the weak Raman scattering cross sections and consequently the signal intensities up to 6 orders of magnitude. If a Raman excitation wavelength is selected in resonance with an electronic absorption band of an analyte, the polarizability increases, allowing the detection of low concentrations. Such RR spectra are dominated by vibrational bands of molecular groups that are assigned to electronically resonant chromophores. Therefore, fewer vibrations contribute to the overall RR spectrum compared to the nonresonant Raman spectrum. RR spectroscopy is restricted to molecules with chromophores and requires an excitation laser tuned to the electronic absorption. Another restriction is that the electronic excitation of the molecules of interest often leads to rapid photodegradation, which can be overcome by rotating the sample. Furthermore, the simultaneous excitation of fluorescence can obscure the RR spectrum in the case of small Stokes shifts (i.e., spectral separation of absorption and fluorescence spectra). Common electronic chromophores utilized in RR spectroscopy are $\pi \rightarrow \pi^*$ transitions due to conjugated π-bonds and are usually the basis for RR enhancements observed in biologically relevant molecules. Terpene-based unsaturated aliphatic compounds that play a role as antioxidants or serve as precursors such as carotenoids and can sensitively be detected by RR spectroscopy are quite abundant.[12] Another family of biological chromophores are porphyrin derivatives as complexing ligands for various metal ions that are important for oxygen transportation such as hemoglobin[52] and often function as catalytic reaction center for electron transition reactions in enzymes such as cytochromes.[53] As the absorption bands are relatively broad compared to the monochromatic excitation laser, standard Raman systems can be applied to RRS studies. Green laser wavelengths such as 514.5 nm from Argon ion emission and 532 nm from frequency doubled Nd:YAG

https://doi.org/10.1021/acs.analchem.1c03235
Anal. Chem. 2022, 94, 86−119

emission give good RRS enhancement for terpene-based compounds and porphyrin derivatives. At 785 nm excitation, a preresonant effect is observed for terpene-based compounds. Applications of RR spectroscopy to study these molecules are presented in Resonance Raman Spectroscopy of Proteins and Nucleic Acids.

Ultraviolet resonance Raman (UVRR) spectroscopy to probe selective nucleic acid and protein residues in nucleoprotein complexes were reviewed.[54] UVRR spectroscopy probes specific bonds of aromatic amino acids phenylalanine, tyrosine and tryptophan near 280 nm, nucleobases adenine, cytosine, guanine, thymine and uracil near 260 nm, and the peptide bonds of proteins below 220 nm. A UVRR spectrometer was described for structural studies of biological macromolecules and their assemblies and included a continuous wave, intracavity frequency doubled Argon ion laser for excitation.[55] UVRR spectra of aromatic amino acids and nucleotides of H_2O and D_2O solutions were reported for laser excitation wavelengths of 257, 244, 238, and 229 nm together with scattering cross sections for all prominent bands using the 981 cm^{-1} marker of SO_4^{2-} as an internal standard.[56] However, reports on cell and tissue samples are less frequent, probably due to the higher susceptibility of biological samples to UV radiation compared to RR spectroscopy in the visible and near-infrared spectral range.

Further signal amplification in studies of hemeproteins and those in biological systems can be achieved by combining RRS with surface enhanced Raman scattering (SERS), which is called surface enhanced resonance Raman scattering (SERRS).[57] Details of SERS will be covered in the next section.

Plasmonic-Enhanced Raman Techniques. *Surface Enhanced Raman Spectroscopy (SERS).* To enhance the Raman scattered light by 6 to 10 orders of magnitude, plasmonic active nanostructures are used in surface enhanced Raman spectroscopy (SERS).[58−61] The Raman signal enhancement is associated with the optical properties of metallic nanostructures, i.e., the interaction of light with metallic nanostructures. If their sizes are much smaller than the incident wavelength, a displacement of the electron cloud and thus a polarization within the metallic particle are induced.[62] The resonant excitation is described as a localized surface plasmon polariton; its spectral position is defined by the plasmon resonance condition and depends on the dielectric constant of the surrounding medium as well as the material, size, and shape of the metallic nanoparticle. At the interface between a metallic waveguide, e.g., a regular nanostructured grating, and a dielectric, propagating surface plasmon polariton modes are observed. These plasmonic effects result in a strong electromagnetic field enhancement in SERS and are described as electromagnetic enhancement, the main contribution to the overall SERS signal (enhancement factor, EF, of 10^4−10^8). Additionally, the chemical enhancement, described as the first layer effect, contributes to the SERS spectrum (EF < 10^2). Consequently, SERS is a molecular fingerprint detection scheme with high sensitivity, enabling the analysis of trace amounts and even single molecules. As SERS active substrates, mostly Ag (excitation in the visible range) and Au (excitation in the red and NIR spectral region) nanostructures are employed. In general, Au is preferred over Ag as a plasmonic active material for biomedical applications.[62] To evaluate the quality of the enhancing sensor surface, i.e., the SERS substrate, both the EF value and limit of detection (LOD) should be estimated.[60] Under SERS conditions, the Raman modes of the target analyte perpendicular to the metallic surface get preferentially enhanced (i.e., surface selection rules[63]) and the spectroscopic selection rules are altered due to the gradient of the evanescent electromagnetic field on the SERS substrate.[64]

Employing SERS as an analytical method, researchers can choose between various detection modes to determine different chemical properties of the analyte molecules and affinities toward the sensor surface: (i) Label-free SERS is characterized by a direct detection scheme; i.e., the target analyte is in close proximity to the metallic sensor surface (up to a distance of 5 nm), and the SERS spectrum is dominated by its contribution.[62] To enable sensitive detection in complex matrices, a high affinity of the target molecule toward the metallic surface is required. This can be achieved via S or N containing chemical moieties, or cleanup processes have to be combined with the detection scheme.[65] Mostly, label-free SERS sensing is applied for low molecular weight substances such as drugs, metabolites, or small biomolecules. A modification of the sensor surface with zwitterions, molecular brushes, or lipophilic sensor layers might increase the affinity of the target analyte toward the sensor surface and result in a better signal-to-noise ratio of the SERS spectra. (ii) In the case of large biomolecules such as proteins or DNA, label-free SERS spectra of the macromolecule vary if no reproducible orientation toward the metallic surface can be achieved. Thus, SERS tags or labels, Au nanoparticles equipped with a Raman reporter, and recognition elements such as antibodies or aptamers are applied in immunoassays and comparable sensing strategies.[58,62,65] This way, proteins, antigens, or DNA strands are bound to the surface, and the binding event is detected by the appearance of a strong SERS signal of the Raman reporter. Such an approach is applied to lateral flow assays and the recognition of overexpressed surface proteins on cells or in tissue.[66] Moreover, reporter DNA strands can be equipped with various dye labels (showing different Raman marker modes), and the detection scheme is performed on a SERS-active sensor allowing a sequence-specific and sensitive detection of the target DNA strands from pathogens via multiplexing SERS analysis.[67] (iii) For the SERS-based detection of small molecules showing no or a very weak SERS signal and inorganic ions, molecular sensors are developed.[66,68] Here, the SERS-active metallic surface is modified with a sensor molecule undergoing a chemical reaction or reorientation upon the interaction with the target analyte. Thus, a high specificity is achieved, and an interference with SERS signals of the molecules from the matrix is suppressed. (iv) Finally, shell-isolated nanoparticle-enhanced Raman spectroscopy (SHINERS) is a modification of SERS in which the nanoparticles coated with a thin protection layer are placed directly on the surfaces and buried interfaces to allow for *in situ* measurements.[69] This prevents direct contact with the sample, which is important for biological samples as the structure of large biomolecules could be affected by the metal surface.

Tip-Enhanced Raman Scattering (TERS). TERS extends the application of SERS to analyses where the highest lateral resolution is required. This is realized by implementing a scanning probe microscope to a Raman setup, i.e., an atomic force microscope (AFM) and/or a scanning tunneling microscope (STM). As conductive samples are indispensable for STM-TERS experiments, biological samples are mainly studied with AFM-TERS. Briefly, a commercially available cantilever tip covered with silver or gold nanoparticles is positioned in the focus of a Raman laser, and the sample is scanned. Simultaneous to the topography imaging, TERS spectra are recorded. The vibrational modes of the molecules in the immediate vicinity to

https://doi.org/10.1021/acs.analchem.1c03235
Anal. Chem. 2022, 94, 86−119

the tip are maximally enhanced if the laser wavelength matches the plasmon resonance of the SERS active particle at the tip apex. Thus, the detection sensitivity can be increased down to the single molecule level with a spatial resolution in the (sub)nanometer regime.[70−74] The crucial part in any TERS experiment is the plasmonic probe, which determines the quality of the results. Since it is very susceptible to mechanical and environmental influences, care must be taken that the sample−tip interactions are well controlled during the entire experiment. Otherwise, the silver particle can be scraped off. In addition, when working with soft samples or molecules with a high affinity toward silver, molecules from the surface can easily be picked up, leading to tip contamination. Therefore, a check of the tip for possible contamination and destruction is strongly recommended by recording a reference spectrum on a sample-free spot on the substrate.

It is important to note that in TERS generally vibrational modes with a preferred orientation parallel to the main axis of the tip are enhanced while modes perpendicular to the tip axis remain almost silent, i.e., absent in the spectra. Similar to SERS, the selection rules are altered, and the TERS spectra, especially band intensity ratios, can significantly differ from conventional Raman spectra.[75,76] An advantageous side effect of combining scanning probe microscopy with Raman spectroscopy is that the morphological and spectroscopic data acquisition is performed in a single experiment and thus can be directly correlated. Depending on the experimental setup, either the spectra are recorded pixel by pixel over the entire scan range or individual measurement points are specifically selected. So far, this near-field technique has been used to investigate very different materials ranging from carbon-based and 2D materials to catalytic reactions and biological specimen. In all questions, one aims at highly sensitive chemical characterization or identification of specific components, structural changes, or defects far beyond the diffraction limit.

Nonlinear, Coherent Raman Spectroscopy. When using temporally overlapping ultrashort laser pulses with high intensities and difference frequencies spectrally covering a part of the vibrational spectrum, nonlinear Raman processes can be excited. Because the emission of inelastically scattering photons is coherently induced, coherent Raman scattering (CRS) has been introduced as the collective term for the associated tools: coherent anti-Stokes Raman scattering (CARS)[77] and stimulated Raman scattering (SRS)[78] as well as the Raman induced Kerr effect (RIKE).[79] Similar to TERS, SERS, and RRS, CRS also enhances the Raman scattering signal by orders of magnitude. In contrast to the before mentioned methods, two different enhancement mechanisms contribute to the CRS signal. First, the nonlinear dependence on the excitation laser intensity increases the CRS signal. The higher the peak intensity, the higher is this enhancement. In order to selectively address specific Raman resonances of bandwidths on the order of 2−10 cm^{-1}, excitation pulses of ps duration are employed, which provide simultaneously high peak intensities and high spectral resolution of a few cm^{-1}. Second, the electromagnetic fields scattered off the individual molecules of interest within the laser focus are coherently added, which increases the Raman signal by several orders of magnitude. In spontaneous Raman scattering, the intensity of the individual emissions is added. As a result, the coherent enhancement factor of CRS is particularly large for concentrated species. Thus, CRS enables chemical imaging of concentrated species, i.e., lipids and proteins in tissue specimen, with subμs pixel dwell time and video-rate image acquisition, which is orders of magnitude faster compared to spontaneous Raman scattering. However, this advantage typically comes at the cost of investigating the spatial distribution of a single or few molecular bonds within the specimen. Due to the coherent addition of the scattered signal of individual molecules, CRS imaging is less sensitive to low concentrations compared to spontaneous Raman scattering.[80] However, in many applications, this is not a limitation since CRS enables the investigation of label-free and noninvasive processes where there is no alternative imaging tool and spontaneous Raman scattering imaging is simply too slow.

Technically, CRS is realized by coupling a dual-wavelength ps-laser source[81] into a laser scanning microscope optimized for nonlinear multiphoton microscopy using near-infrared excitation lasers and non-descanned large area detectors for the collection of scattered photons. Both excitation wavelengths are spatially and temporally overlapped at the focus position for efficient signal generation. While CARS is implemented using synchronized ps excitation lasers, it suffers from interference with the nonresonant background generated by four wave mixing, which results in line shape distortions, spectral shifts of the peak position, and other interference effects. SRS provides the same line shape as spontaneous Raman scattering but poses much stricter constraints on the laser source and requires special detection systems. SRS and CARS will be briefly described in the following sections.

Stimulated Raman Scattering (SRS). SRS has become an established method in biomedical research for label-free imaging of lipids, proteins, and DNA.[82] The method can be used to visualize several molecular markers.[83] Major applications in medical research focus on brain tumor imaging[13,84,85] and Alzheimer's disease.[86] Technically, both CRS processes SRS and CARS take place simultaneously when focusing two synchronized and spatially overlapping laser beams of a difference frequency matching the frequency of a molecular vibration into a specimen containing this molecular species. However, the SRS process cannot be directly detected because the SRS process results in the conversion of high energy pump photons into Stokes photons by exciting a vibration. Since the photon flux in the ultrashort pulses is high, the conversion of the pump into the Stokes photons is on the order of 10^{-4} and below. This is typically lower than the root-mean-square (RMS) noise of typical laser sources, which are on the order of 10^{-3}. Therefore, the method of modulation transfer is used for detecting the SRS signal. Here, one of the two lasers is modulated at high frequency, e.g., in the range of 1−20 MHz, and the modulation transfer is detected on the other beam. If the Stokes beam is modulated, the modulation transfer on the pump beam is detected. Here, the number of photons of the pump beam decreases in the presence of the Stokes beam. This process is called stimulated Raman loss. If the pump beam is modulated, the modulation transfer on the Stokes beam is detected. Here, the number of photons increases in the presence of SRS, which is called stimulated Raman gain, but in order to detect the SRS signal, not only does the laser need to be modulated, but also a special detection system needs to be used, which provides a high dynamic range for detecting a large number of photons and detects small fluctuations in the intensity at the laser modulation frequency. As a detector, large area photo diodes are used. A bias voltage is applied in order to increase the bandwidth of the detector, since the maximum frequency needs to be in the range of the modulation frequency. This is a critical point, since the cutoff frequency of the photodiodes is larger for smaller active

https://doi.org/10.1021/acs.analchem.1c03235
Anal. Chem. 2022, 94, 86−119

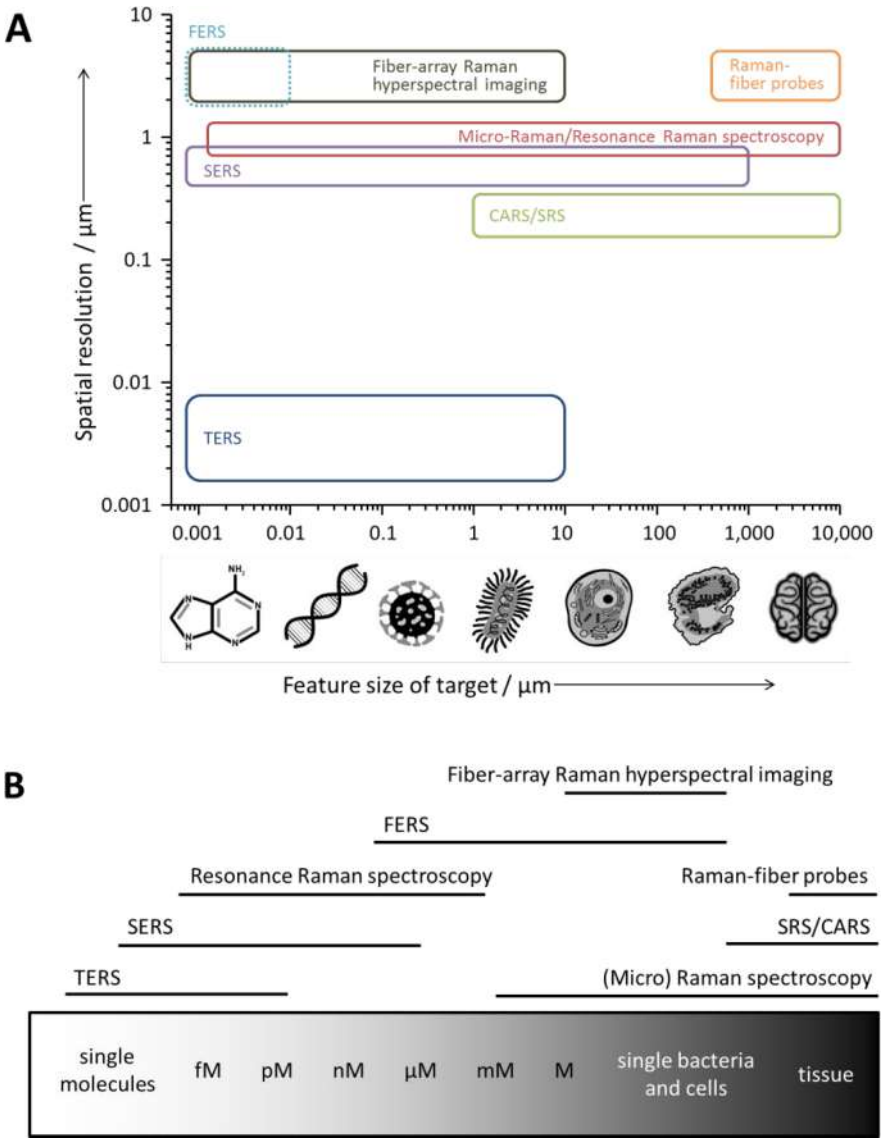

Figure 1. (A) Illustration of the spatial resolution and feature size of the target for various Raman-based techniques. (B) Sensitivity scale of various Raman-based methods.

areas, while the dynamic range is larger for larger active areas. Typically, 1 cm^2 active area photodiodes can be used at modulation frequencies of 20 MHz and for 50 mW of average laser power. In order to extract the SRS signal, lock-in detectors[78] or tuned amplifiers[87] need to be used to extract the small signal variation at the modulation frequency. Current technological research is focusing on speeding up the data acquisition in order to image whole volumes using sparse spectral and spatial sampling.[88]

While a huge advantage of CRS is label-free imaging, the sensitivity is still limited to visualize the distribution of abundant biomarkers. The detection limit is in the mM range. For visualizing molecules at lower concentrations, vibrational imaging has emerged on the basis of either isotope labeling, e.g., exchanging hydrogen by deuterium, or alkyne tagging. In comparison to fluorescence labeling, the structural changes induced by vibrational labels are smaller, such that the molecular mass and chemistry are significantly less affected. Therefore, vibrational labeling can be performed for much smaller molecules. In addition, alkyne tagging enables a significantly lower limit of detection on the order of 100 μM or 10000 alkyne molecules only.[89]

For visualizing even lower concentrations, fluorescence molecules can be modified by alkyne tags but using SRS as a read out mechanism. This approach has two advantages: the limit of detection is on the order of 250 nM due to preresonance enhancement; there is no photobleaching, and since Raman bands are spectrally narrow, many more molecules can be simultaneously tracked; e.g., 24 labels can be used simultaneously.[90] When using fluorescence as read-out and resonance enhancement, even single molecule sensitivity can be achieved.[91]

Coherent Anti-stokes Raman Scattering (CARS). From all CRS techniques, CARS has been applied first for imaging. In comparison to SRS, CARS is technically simpler to realize: no low noise laser source is needed; no laser modulation and frequency selective detection system is needed, and the same laser scanning microscopes and detectors can be used for CARS, which are also used for fluorescence. However, since the signal is mostly emitted in the forward direction, the use of non-

https://doi.org/10.1021/acs.analchem.1c03235
Anal. Chem. 2022, 94, 86−119

descanned PMT detectors in the forward direction provides the largest detection efficiency for CARS signals. Four wave mixing is limiting the sensitivity by generating the so-called nonresonant background. In comparison to SRS, the intensity dependence of CARS is higher, $I(\mathrm{CARS}) \sim I^2(\mathrm{pump})I(\mathrm{Stokes})$, while for SRS, $I(\mathrm{SRS}) \sim I(\mathrm{pump})I(\mathrm{Stokes})$. In addition, the emission wavelength is lower than the excitation. Both properties result in a potentially higher spatial resolution of CARS with respect to SRS since the focal volume is smaller. In addition, scattering in tissue of the lower wavelength CARS signal is higher compared to that in the excitation lasers, which results in larger detection efficiency in the backward direction when imaging bulk tissue. Finally, broadband CARS using spectral detection is rather simple using spectrographs and broadband lasers[92] since the signal is spectrally separated, while in the case of SRS, multielement lock-in amplifiers or other advanced instruments are needed for broadband SRS detection.

Due to its simplicity and the larger detection efficiency in the backward direction, CARS is the method of choice for *in vivo* applications, in particular endoscopy. Here, several concepts have been realized during the past years. A rigid endoscope of 2 mm diameter provides almost a 20 cm working distance for brain imaging combining CARS, two-photon excited fluorescence (TPEF), and second harmonic generation (SHG).[93] A semiflexible endoscope of 8 mm diameter based on an imaging fiber enables endoscopy without moving or electric parts.[94] Smaller probes have been realized using piezo-scanners in a compact format of 4.2 mm diameter, 71 mm length, and 320 μm field of view, generating CARS and SHG images at 0.8 frames per second.[95]

Summary of Raman-Based Techniques. In summary, Raman spectroscopy is a molecular specific, powerful tool for label-free chemical characterization and identification of complex biological systems. The method works nondestructively, which is a crucial parameter when working with delicate samples. Conventional Raman spectroscopy is suited for highly concentrated solutions of (bio)molecules and bulk material as well as single cells and tissue samples. In combination with microscopy, a spatial resolution of about 1 μm can be achieved, allowing for the detection of Raman spectra of single bacterial cells or the identification of tissue features. Compared to conventional Raman spectroscopy, in SERS, the spatial resolution is decreased since only molecules in close vicinity to the metallic nanostructures contribute to a fingerprint spectrum. Simultaneously, the detection sensitivity is increased by several orders of magnitude. As a result, low molecular weight substances in trace concentrations up to single cells and tissue sections can be probed. The detection volume can be confined even more if TERS is used. In this method, the spatial resolution is in the nanometer range as the detection device is a single plasmonic active nanoparticle at the apex of a scanning tip. CARS and SRS provide diffraction limited spatial resolution below 250 nm in combination with high-NA microscopic objectives. Both techniques are mostly applied to investigate tissue sections up to organs, illustrating the spatial distribution of marker molecules such as the key groups of macromolecules in cells such as proteins, lipids, and DNA but also molecular markers, e.g., glycogen,[96] cholesterol, acetylcholine, or retinoic acid by targeting chemical bonds directly. In contrast to fluorescence, CRS enables the investigation of the spatial distribution of small marker molecules. When Raman-fiber probes are employed, noninvasive applications to identify tumor margins are envisaged and a spatial resolution in the micrometer range is achieved. Fiber-array Raman hyperspectral imaging allows for the detection of low molecular weight substances with a spatial resolution of 1 μm.[97−99] The spatial resolution as well as the feature size of the targets is illustrated for all discussed Raman-based methods in Figure 1A.

Raman spectroscopy records molecular specific signals that are used to identify biomolecules and their complex mixtures. However, due to the inherent weak Raman intensities, the detection limit is usually in the millimolar range for typical biomolecules in tissues, cells, and bacteria (see Figure 1B). In order to increase the sensitivity, FERS can be applied. Here, the signal enhancement is associated with an extended beam path in a fiber.[43] Moreover, RR spectroscopy shows enhancement factors in the range of 6 orders of magnitude, allowing for the detection of resonant molecules down to the picomolar and femtomolar regime. In the case of SERS, enhancement factors are reported in the range of 10^6 to 10^{10}.[58−60] As a consequence, SERS shows sensitivity down to single molecules. From all herein introduced Raman-based methods, the TERS technique is considered the most sensitive as it allows for the investigations of subunits of single biomolecules such as DNA or proteins due to the nanometric spatial resolution. Finally, Raman-fiber probes as well as CRS techniques are applied to characterize tissue sections or investigate organs.

For more information on the advantages and disadvantages of all Raman-based methods, the interested reader is referred to the literature.[6] Within the next paragraph, applied fields of Raman spectroscopy and its variants will be discussed, including low molecular weight substances, biomacromolecules, cells, tissue sections, and organs.

APPLICATION IN BIOANALYTICS

Detection of Low Molecular Weight Substances. The characterization of low molecular weight substances by means of Raman spectroscopy is well suited to record vibrational fingerprints of bulk material. However, as the Raman cross section is inherently small, signal enhancing processes are required to allow for the detection of low molecular weight substances in trace concentrations. Within this section, recently published examples are summarized employing SERS and FERS as well as RR spectroscopy for readout.

Medical Applications of Signal Enhancing Processes. In order to address low molecular weight substances in medical applications, the detection of drug molecules, biomarkers, or metabolites is envisaged. For the detection of the drug 2-thiouracil, a silver nanoparticle modified graphene SERS substrate was developed.[100] The linear detection is achieved between 1 and 0.1 μM, and the detection limit is 10 nM. To allow for a sensitive detection of the antibiotic levofloxacin in urine, a microfluidic-based sensing concept was developed using colloidal silver nanoparticles as SERS-active substrate.[101] The measuring conditions were defined by using artificial urine as the matrix, and upon dilution with water, the limit of detection (LOD) is improved to 0.07 mM, which is attributed to the decreased competition between target molecule and matrix molecules for free binding sites at the nanoparticle's surface. Moreover, levofloxacin was spiked into individual and pooled human urine samples, and SERS spectra for urinary concentration between 0.45 and 1.8 mM were recorded. The root-mean-square error of prediction was between 0.058 and 0.16 mM for all investigated human urine samples, illustrating the potential of the method for monitoring the drug's clearance. The same sensing platform was applied to detect nitroxoline in

https://doi.org/10.1021/acs.analchem.1c03235
Anal. Chem. 2022, 94, 86−119

spiked human urine.[102] Here, the standard addition method was used for the analysis, allowing the application of the clinical samples to record the calibration curve. A linear dependency of the SERS signal is found between the concentrations of 4.28 and 42.8 μM, and the LOD is around 3 μM. Moreover, the detection of the neurotransmitter dopamine is performed in artificial cerebrospinal fluid and in extracts from mouse striatum.[103] To allow for a very specific and sensitive detection, magnetic beads are coupled with silver nanoparticles as well as a reporter molecule specific for dopamine. In the presence of the target dopamine, it is bound selectively toward the surface of the molecular sensor, and via magnetic separation, matrix molecules could be separated. As a result, SERS spectra are recorded down to concentrations of 50 fM. Thus, selective enrichment of the target analyte accompanied by a separation from matrix molecules allows for both specific and sensitive detection of biomolecules in complex matrices at clinically relevant concentration levels. Finally, when label-free SERS is employed, the antitumor drug 6-mercaptopurine and its metabolite 6-mercaptopurine-ribose is investigated in living cells.[104] Due to the different orientation of the two analyte molecules toward the metallic surface, the SERS spectra show a different peak ratio of two marker modes, which allows the identification of the drug and its metabolite even in a complex matrix of a living cell. Thus, the metabolism process is monitored for a deeper insight into the molecular mechanism of antitumor drugs at the cellular level.

In order to detect glucose and lactate in living tissue, a highly porous nanoscalic metal−organic framework (MOF) structure was equipped with leucomalachite green modified gold nanoparticles and glucose oxidase or lactate oxidase.[105] Due to the reaction with glucose and lactate, respectively, hydrogen peroxide is produced, which facilitates the reaction of the reporter molecule on the surface of gold nanoparticles to malachite green. As a consequence, intense SERS spectra dominated by the contributions of malachite green are recorded upon the presence of both glucose and lactate in living brains and tumor tissue and changes in concentration can be monitored and associated with physiological and pathological conditions.

Moreover, the enhancement provided by elaborated hollow sensor fibers (FERS) is applied to the highly sensitive monitoring of antibiotics.[106] Low LOD values have been achieved for the antibiotics moxifloxacin (LOD: 1.7 μM)[45] and levofloxacin (LOD: 20 μM)[41] in water. Going a step further, cefuroxime was quantified (in human urine, down to 100 μM).[47] To prove clinical applicability, urine samples were collected from volunteers after different oral doses of the antibiotic cefuroxime and were measured with the standard method HPLC and FERS. The results of the FERS measurements were in very good agreement with HPLC results. Thus, FERS was validated and proven as a very promising technique for therapeutic drug monitoring in urine.[47] FERS has also been exploited for biomarker detection. Khetani et al. quantified heparin in blood serum down to 12 USP/mL with a near-infrared excitation wavelength of 785 nm.[46] For the detection of adenosine, FERS was successfully combined with SERS.[42] Yan et al. reported about the FERS analysis of hyperbilirubinemia and hyperbiliverdinemia related diseases.[43] Clinically relevant concentrations of bilirubin and biliverdin were simultaneously quantified in the micromolar range. The concentrations of 1 μM biliverdin and 50 μM bilirubin were chosen to simulate hyperbilirubinemia due to malignancy, infectious hepatitis, cirrhosis, or stenosis of the common bile duct and 25 μM biliverdin and 75 μM bilirubin for the case of the rare hyperbiliverdinemia.[43] Besides standard silica fibers, microstructured polymer optical fibers (LC-mPOFs) were also applied. The aim of this study was to prove the suitability of this platform for glucose detection[107] and for drug monitoring during the sodium−glucose cotransporter 2 inhibitor therapy in diabetes mellitus type 2.[107] During the therapy with these kind of drugs, high glucose amounts are excreted via urine. Therefore, it is proposed that the combined monitoring of urinary glucose levels and blood glucose indices would be beneficial for an optimal antidiabetic therapy.[107] The novel LC-mPOF glucose detection approach has the advantage that the sensor fiber can be used as a one-way product. Furthermore, FERS was recently applied to monitor the Alzheimer disease biomarker β-amyloid plaques (100 μg/mL) using a flow through principle.[44]

SERS as the Detection Scheme in Food Analytics and Agriculture. In agricultural processes, a large amount of chemicals are applied to ensure high yield; thus, their residues are found in food products.[108] As SERS provides fast, specific, and sensitive chemical information, this detection scheme is applied for the detection of pesticides, antibiotics, and β_2-adrenergic agonists in crops, milk, surface water, meat, and animal urine as summarized within the review article by Jiang et al.[108] To detect pesticides by means of SERS, enrichment and purification processes need to be applied to allow for a sensitive detection of the target analyte in food matrix or crops.[109] Analytics of pesticide trace levels in liquid samples or on surfaces of solids could be performed by employing a simple extraction protocol; however, the inhomogeneous distribution on or in the food matrix and the internalization of pesticides in crops will improve the complexity of the sample treatment procedure. In the case of interfering matrix molecules avoiding the enhancement of the Raman signals of pesticides on the sensor surface, separation techniques need to be established. In the case of the detection of the fungicide thiophanate-methyl and its metabolite carbendazim on the surface of red bell pepper, the targets were immobilized on the sample surface and the SERS-active silver sol was added.[110] Subsequently, SERS spectra were recorded, and prediction models were developed. For the fast detection of difenoconazole in grapes, the samples were first homogenized before applying the extraction protocol and finally SERS as the readout method.[111] As SERS substrates, core−shell gold silver nanoparticles are used, and the authors found a linear dependency in a double-logarithmic plot between 5×10^{-7} and 2.5×10^{-5} M with a LOD of 5×10^{-8} M.

The SERS-based molecular sensor concept is applied for the detection of nitrite in meat products.[112] Due to the presence of nitrite, a chemical reaction takes place, producing azo groups on the sensor surface, and consequently, the SERS spectrum is changed due to the concentration-dependent appearance of three marker modes. The authors demonstrate the readout by three different techniques, i.e., colorimetry, fluorescence, and SERS, whereas the lowest LOD of 0.8 nM was achieved by employing SERS.

Besides the matrix of body fluids, researchers challenged the SERS technique toward the specific detection of contamination within milk and milk products. One example is the detection of melamine in milk extracts by using gold nanoparticles as the SERS substrate.[113] A linear dependency of the SERS signal and the melamine concentration was found between 0.31 and 5.0 mg/L, and the LOD is 0.17 mg/L, meeting legal requirements (1 mg/L limit for powder infant products and 2.5 mg/L for food and stuffs). The authors reported a total analysis time of <30

https://doi.org/10.1021/acs.analchem.1c03235
Anal. Chem. 2022, 94, 86−119

min. Moreover, molecular-imprinted polymers (MIPs) were applied to enrich and separate melamine from whole milk.[114] With silver dendrites as the SERS substrate, a linear signal dependency was found between 0.005 mmol/L (0.63 mg/L) and 0.05 mmol/L (6.31 mg/L). The LOD value was estimated to be 0.012 mmol/L (1.51 mg/L). Another investigated milk contaminant is the herbicide 2,4-dichlorophenoxyacetic acid, which was extracted from milk, and subsequently, SERS spectra of the extracts were recorded.[115] The LOD was 0.01 ng/mL, and the linear range of the concentration-dependent SERS measurements was between 10^{-2} and 10^{6} ng/mL, showing the potential of SERS in quality monitoring of milk and its products. The broad application of penicillin in livestock farming results in the appearance of its metabolite penicilloic acid in milk and milk products, and a sensitive detection is required, which was achieved using label-free SERS.[116] Here, gold nanoparticles were modified with a silver shell acting as a powerful SERS substrate, and the authors reported on a specific and sensitive detection of penicilloic acid in milk (LOD: 3 ppm), yogurt (LOD: 3 ppm), and milk powder (LOD: 4 ppm) within 3 min. The marker mode at 882 cm^{-1} was not interfering with contributions from the matrix.

Resonance Raman Spectroscopy to Detect Chromophores. RR spectroscopy is especially suited for detecting low concentrations of certain substances if they absorb in the spectral region of the excitation laser. Such substances can even be detected in complex matrices since all other nonabsorbing chemicals do not exhibit RR spectra. Chromophores that are especially suited for RR spectroscopy are carotenoids. Carotenoids (hydrocarbons) such as tetraterpenes and xanthophylls (contain oxygen) consist of a polyene chain with several methyl side groups. The RR spectra of such substances exhibit three main signals, namely, the C=C stretching vibration around 1520 cm^{-1}, the C−C stretching vibration at 1168 cm^{-1}, and the C−CH_3 deformation vibration at 1003 cm^{-1}. Depending on the size of the π system, the position of the C=C stretching vibration varies significantly.[117] In addition, side chains (with or without oxygen) or ionone rings slightly vary the position of the carotenoid signals.[118]

The relative concentration of carotenoids in various vegetables can be estimated by fitting the intensity of the C=C stretching vibration. During boiling, the carotenoid signals varies over time, but the rate depends on the specific vegetable. In addition, peeled and unpeeled vegetables show some variations in the carotenoid content and boiling behavior.[119] This method can be extended to mixtures of carotenoids when the exact spectral band positions of different carotenoids or xanthophylls in, e.g., plants or algae are known. The intensity of these marker bands can then be used to determine the concentration of different xanthophylls, like, e.g., violaxanthin, zeaxanthin, diadinoxanthin, and diatoxanthin, and their behavior over different illumination cycles[120] and after the administration of drugs.[121]

Carotenoids are not only found in plants. Typical pigments in mollusk shells are normally carotenoids or porphyrins. Even in bivalve larval shells, the type and distribution of various carotenoids can be observed.[122] Bacteria normally use carotenoids as photoprotection from exposure to sunlight, especially the UV fraction. Here, the photostability of the pigments toward UV light depends on the type of carotenoid or xanthophyll.[118] Using the typical information on the carotenoids even allows one to differentiate between various pigmented species.[123] Apart from such naturally occurring chromophores, also pharmaceutically important substances can be monitored by means of RR spectroscopy. Using a competitive assay, it is possible to detect the concentration of cortisol in serum samples.[124]

RR spectroscopy is a noninvasive optical quantitative method to measure carotenoid antioxidant levels in human skin *in vivo*.[12] Raman spectrometers were designed to monitor carotenoids in the skin with the main RR bands near 1520, 1168, and 1003 cm^{-1}. The system suggested by Darvin et al. used an Ar+ laser that excited at either 488 or 514.5 nm, an excitation fiber, a fiber bundle for the collection of the Raman scattered light, and appropriate optical elements. To have a feasible field of view, the laser beam was expanded to 6.5 mm.[125] The penetration depth into the skin was estimated to be about 150 μm. A commercial confocal RR setup (RiverD, The Netherlands) uses 785 nm excitation, which offers higher penetration depth in tissue. In the case of carotenoids, especially β-carotene, substantial enhancements have still been observed for excitations in the preresonance region shifted into the near-infrared about 800 nm. The instrument was recently applied to quantify the *in vivo* skin penetration of topical applied materials including retinol, another group of molecules with conjugated double bonds.[126] After these initial proof-of-principle developments, the concept has been picked up by the nutritional supplement industry to develop a miniaturized platform with 473 nm light for excitation (Biophotonic Scanner, NuSkin/Pharmanex Inc., USA). A recent clinical trial concluded that the skin carotenoids status as measured by RR spectroscopy is moderately to strongly correlated with plasma carotenoid concentrations, indicating that it can be a powerful tool to assess carotenoid-rich vegetable and fruit intake.[127]

The shift of the excitation wavelength to the UV enables one to monitor even more chemicals that do not show electronic excitation in the visible range. The application of a wavelength of, e.g., 244 or 257 nm allows one to monitor some antibiotics in human urine samples. Since an excitation of 257 nm exhibits fluorescence, the analysis with a laser wavelength of 244 nm is better suited for the quantitative evaluation of the antibiotics in physiological reasonable concentrations.[128] In addition, cocaine in oral fluid can be detected by the means of UVRR spectroscopy and an excitation wavelength of 239 nm. With such a setup, 10 μg/mL could be detected, which is a remarkable result but is still 3 orders of magnitude too insensitive.[129]

In conclusion, a high number of signal enhancing Raman-based detection schemes are available to monitor low molecular weight substances in trace concentrations. When the measurements are performed in real matrices with a high complexity, contributions from matrix components can interfere with the overall fingerprint spectrum. Due to the high affinity of the target molecule toward the metallic surface, the signal originating from the background could be suppressed in the case of SERS. As a further strategy, cleanup processes and purification steps should be included in the overall analysis protocol when matrix components hinder the Raman-based detection of low molecular weight substances in trace concentrations. In the case of resonant molecules, the RR spectrum is dominated by contributions from the vibrational modes associated with the electronic transition, allowing for the detection of trace concentrations even in complex matrices such as cells and tissue.

Raman Spectroscopic Characterization and Detection of Biomacromolecules. Raman spectroscopy allows the recording of molecular specific fingerprint information. However, due to the inherent weak Raman signal, only high

https://doi.org/10.1021/acs.analchem.1c03235
Anal. Chem. 2022, 94, 86−119

concentrated substances could be investigated. In order to allow for an investigation of low concentrated biomacromolecules such as nucleic acids, peptides, or proteins, signal enhancing processes, i.e., SERS and RR spectroscopy, are applied. If additional detection with a high spatial resolution is required, TERS is the method of choice.

Raman Spectroscopic Approaches. Biomolecules such as DNA or proteins are highly relevant analytes in the biomedical field as they are basic components of any cell or tissue sample. Due to the chemical information concealed in the fingerprint region of the spectra, Raman spectroscopy is ideally suited for detecting changes in the DNA or protein content of a sample. Since Raman spectroscopic techniques are extremely sensitive toward alterations in the molecular structure, not only can the presence and amount of these biomolecules be investigated, but also their higher order structures or conformation are obtainable. For example, Bhunia et al. studied ionic and tautomeric conformers of the nucleobase adenine in aqueous solution at different pH values via their characteristic Raman spectra.[130] For elucidation of the structural changes associated with the pH shift, they performed DFT calculations that allowed them to determine which conformers of adenine dominate at certain pH values. Marini et al. designed a superhydrophobic substrate and a corresponding sample preparation protocol enabling them to identify the constitution of the DNA backbone (A-DNA or B-DNA) using Raman spectroscopy.[131] Another DNA structure of interest is the so-called G-quadruplexes, which can be formed by nucleic acid sequences that feature a high guanine content. Friedman and Terentis combined conventional and polarized Raman spectroscopy to characterize these four-stranded DNA structures.[132] They found that their approach is well capable of identifying the different intramolecular structures that are typical for G-quadruplexes. Their results support previously proposed structures deduced by NMR measurements. Generally, it is desirable not only to study the status of a cell at a certain moment but also to track dynamic processes in real time. As a first step toward that goal, Muntean et al. conducted Raman spectroscopic experiments for probing molecular relaxation processes in different nucleic acid components.[133] They determined the vibrational total half bandwidths of functional groups in these samples and derived the corresponding global relaxation times. Next to these fundamental investigations concerning nucleic acids, it is also possible to use Raman spectroscopy to monitor the solid phase synthesis of oligonucleotides. Rydzak et al. implemented both mid-infrared and Raman spectroscopy for surveilling different crucial steps during the automated manufacturing process.[134] By employing these vibrational spectroscopic techniques, they could eliminate several key risks for errors that might occur during the solid phase synthesis.

Further examples illustrating the usefulness of Raman spectroscopy as a tool for quality control can be found in the food analytics sector. Chen et al. developed an online-monitoring system for four important nutrients (protein, fat, sucrose, and total solids) in yogurt by applying digitally labeled Raman spectroscopy.[135] Due to the complex sample composition, advanced chemometric methods such as the Monte Carlo competitive adaptive reweighted sampling selection (MCCARSS) in the higher-density wavelet transform (HDWT) domain were implemented in order to master this challenging task. Jiao et al. investigated different chemometric models to identify adulterants such as creatine, L-glutamine, and taurine in whey protein supplements based on the corresponding Raman spectra.[136] In their study, the soft independent modeling class analogy (SIMCA) model proved to be the most effective choice. Singh et al. applied transmission Raman spectroscopy to determine the protein and oil content in soybeans.[137] Again, statistical methods were used to gain the maximum content of information from the spectroscopic data. The authors considered not only whole beans but also differently processed meals. Overall, the metric-based multiple linear regression (metric-MLR) approach yielded the most robust prediction models for oil and protein content. Mandrile et al. investigated the potential of Raman microspectroscopy to identify prohibited processed animal proteins (PAPs) in feed.[138] Due to the outbreak of bovine spongiform encephalopathy (BSE), these PAPs have been banned by the European Union in order to prevent the transmission of the disease via the food chain. The proposed method combines Raman microspectroscopic measurements followed by an automated data analysis based on a multivariate classification model. The main advantages over other methods, which are currently applied to detect PAPs, are the speed as well as the essential operator independent results.

SERS as a Powerful Tool to Detect Nucleic Acids and Proteins. To achieve a sensitive detection of DNA, the metal/liquid interface of the sensor surface plays an important role, as small changes in the affinity and adsorption to the metallic surface results in a modified orientation of the DNA strand, and thus, the SERS spectral profile is varied.[139] The authors found that two main interaction mechanisms can coexist to influence the Raman mode intensity ratios within the overall SERS spectrum: (i) the adsorption of DNA strands via the nucleobases is accompanied by a displacement of surface ions or molecules on negatively charged surfaces, and (ii) when the metallic surface is modified with positively charged molecules, an electrostatic interaction occurs with the negatively charged phosphate backbone. To improve the reproducibility of DNA SERS spectra, the surface of silver nanoparticles was modified with iodine ions, and thus, surface impurities were removed.[140] This allows a reproducible orientation of the target DNA strands to the metallic surface; with this, replicable SERS spectra of different DNA sequences are recorded showing the potential of label-free SERS in the identification of DNA strands with single-base sensitivity, and hybridization events are observed. To achieve this goal, the SERS spectra are normalized to the phosphate backbone vibration as illustrated in Figure 2. As a further strategy, silver nanoparticles were coated with spermine, and thus, an adhesion of DNA strands via the backbone was achieved, promoting the formation of stable clusters.[141] The authors illustrated the identification and relative quantification of the cytosine modifications 5-methylcytosine, 5-hydroxymethylcytosine, 5-bromocytosine, and 5-hydroxycytosine employing a classification model (partial least-squares discriminant analysis). Moreover, the identification and classification of similar RNA structures was achieved by label-free SERS as the profile of the SERS spectrum is dependent on conformation and composition.[142] The authors illustrated the investigation on conformational differences, i.e., in complementary duplex structures and small interfering and short hairpin RNA molecules, and the characterization of chemical variations, such as single-base mismatches and modifications on nucleobases or the backbone. Recently, a review article was published summarizing label-free SERS approaches on the investigation of nucleic acids.[143] The application of label-free SERS detection on the identification of nucleic acids in complex

https://doi.org/10.1021/acs.analchem.1c03235
Anal. Chem. 2022, 94, 86−119

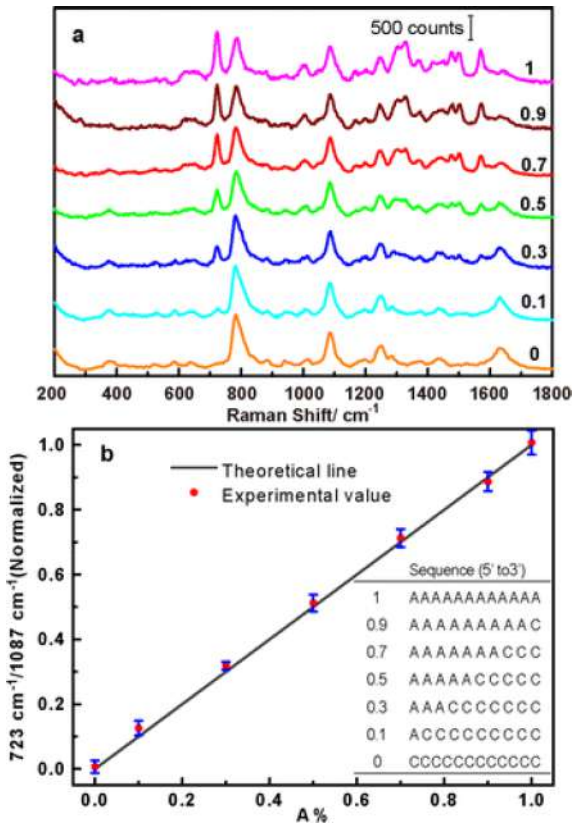

Figure 2. (a) Normalized SERS spectra of DNA strands with different composition in adenine (A) and cytosine (C) with A% = A/(A + C) = 1, 0.9, 0.7, 0.5, 0.3, 0.1, and 0. (b) Illustration of the linear dependency of the marker mode at 723 cm^{-1} normalized to the phosphate backbone mode at 1087 cm^{-1} on the DNA strand composition. Reproduced from Xu, L.-J.; Lei, Z.-C.; Li, J.; Zong, C.; Yang, C. J.; Ren, B. *J. Am. Chem. Soc.* **2015**, *137*, 5149−5154 (ref 140). Copyright 2015 American Chemical Society.

matrices such as the cell interior or body fluids might be hampered by the presence of matrix molecules, e.g., proteins, showing a high affinity toward the metallic surface and, thus, preventing the adsorption of DNA or RNA strands to the metallic sensor surface. Therefore, separation techniques will be required.

A further strategy to allow for the detection of nucleic acids in complex matrices might be the application of SERS nanoprobes also known as SERS labels or tags. A multiplexing strategy was illustrated by creating four kinds of SERS nanoprobes with a mushroom-like shape using DNA capture sequences labeled with four different reporter molecules.[144] Upon the presence of target DNA or RNA, sandwich complexes were formed and the authors showed the detection of three DNA targets and three microRNA targets, respectively, down to the pM concentration range. Finally, the aim in using these SERS nanoprobes in complex matrices was demonstrated by using diluted (20%) serum samples. Moreover, the parallel quantification of microRNA and telomerase in the complex matrix of living cells was reported.[145] Here, a platform was developed to allow for readout via SERS and luminescence. In the presence of microRNA, the specific binding toward a molecular beacon structure resulted in a splitting of gold nanorod dimers, and as a consequence, the SERS signal of the reporter molecule decreased as a function of the microRNA concentration. Due to the interaction of telomerase with the sensor platform, telomerase primer strands were elongated, accompanied by a release of upconversion nanoparticles from the senor surface and an increase in the luminescent signal.

Interactions between proteins and the metallic surface might induce conformational changes or even denaturation. These inherent issues for the label-free SERS investigation of proteins were recently reviewed.[146] Therefore, biocompatible SERS-active nanostructures need to be applied to allow for the characterization of proteins in their native state, which could be achieved via surface modifications. As an example, metallic nanocubes were coated with polyvinylpirrolidone (PVP), and due to the submonolayer at the curvatures, proteins preferentially bind to these spots with the highest electromagnetic field enhancement resulting in SERS spectra with a good signal-to-noise ratio.[147] The authors found no differences between Raman and SERS spectra and concluded that the native state of the protein of interest was conserved for the label-free SERS-based detection.

More often, proteins are detected by the use of immunoassays, where SERS nanoprobes instead of fluorescent labels are applied. Typically, a SERS label is a gold or silver nanoparticle modified with a Raman reporter molecule showing very intense Raman signals and equipped with a recognition antibody to bind specifically toward the target protein.[148,149] Moreover, no bleaching occurs, as it is known for being a fluorescent dye label. A SERS-based immunoassay is a sandwich-based detection scheme, whereas a primary antibody is bound on a surface capturing the antigen from complex matrices, and finally, the SERS tag is bound to the antigen allowing for a fast SERS readout. Here, the binding event is detected by recording typical SERS fingerprint spectra of the reporter molecule. In the case of an application on cellular walls or *in vivo*, SERS labels were bound to the target (surface) protein structure. The application of suited Raman reporter molecules allows for detection even in highly complex biological systems when the Raman fingerprint marker peaks of the reporter molecules do not overlap with the Raman fingerprint information from the biological matrix; i.e., the application of Raman labels with C≡C or C≡N bonds are preferred according to the Raman silent region. The applied SERS probes, barcoding capabilities, and applications are summarized in the literature.[149] As an example, a lateral flow assay was developed for the quantitative and sensitive detection of the cardiac biomarkers myoglobin, cardiac troponin I, and creatine kinase-MB isoenzymes from serum samples.[150] Here, serum was placed on the sample pad, and by means of lateral flow, the SERS tags and the biomarkers were transported to the individual test lines forming sandwich aggregates. The detection could be performed with the bare eye; however, lower detection limits were achieved via SERS readout. The authors also tested for the clinical applicability by analyzing 50 serum samples from acute myocardial infarction patients. For validation, a FDA (U.S. Food and Drug Administration) approved chemiluminescence immunoassay was used. For all three biomarkers, a good linearity was achieved. In comparison to the applied chemiluminescence immunoassay, the SERS assay needs no sample preparation, can provide results after 15 min, and shows a one order higher sensitivity. A further excellent example of a SERS-based lateral flow assay was demonstrated by the detection of the pregnancy hormone human chorionic gonadotropin (hCG) in clinical samples.[151] Therefore, a portable Raman reader with line illumination was developed, allowing for a fast and sensitive point-of-care test in a clinical setting. Capture and control antibodies were arranged on a test

https://doi.org/10.1021/acs.analchem.1c03235
Anal. Chem. 2022, 94, 86−119

strip, and the SERS-labeled anti-hCG detection antibodies were mixed with the serum samples from clinics. In the presence of the pregnancy hormone, a sandwich was formed, which was detected by the portable Raman reader. The detection was achieved in 2 to 5 s, and the detection limit was in the range of 1.6 mIU/mL. The authors illustrated that the applied method was 15 times more sensitive in comparison to commercial available test kits.

TERS on Single Biomolecules. TERS in biological material analysis is often used to identify and differentiate surface components like lipids, proteins, and nucleic acids, e.g., on cells,[152] bacterial spores,[153] and viruses.[154−156] In addition, the high lateral resolution enables the identification of specific building blocks within aggregated peptides[157−160] and nucleic acids.[161−164] Due to space restrictions, the following section will briefly introduce selected works from the field of amyloid fibril and DNA analysis. For a detailed review of the application of TERS to biorelated samples, the reader is referred to Bonhommeau et al.[165] and the literature cited therein. Amyloid structures can be described as misfolded protein aggregates, which are associated with the development of various neurodegenerative diseases. During fibril growth, the native protein conformation changes drastically to β-sheet rich structures, which has been the subject of several near-field Raman spectroscopic studies. Using the amide I or III band positions, which are indicative for the protein secondary structure, it has been demonstrated that amyloid fibril surfaces contain a mixture of α-helix, unordered, and β-sheet structures, independent of the underlying peptide.[157,159,160] In Figure 3a, the spectra from an experiment across a single amylin amyloid fibril are given. The transition from α-helix to β-sheet structures including an area with mixed conformations is clearly visible by changes in the amide I band position.[159] In the second work given in Figure 3b, α-helix and β-sheet structures on an amyloid-b(1−42) fibril could be imaged from amide III band position variations.[157]

Independent investigations of fibrils from other peptides reported similar results, and it was concluded that fibril surfaces generally contain well- and less-ordered areas. The near-field spectroscopic results have been complemented by far-field spectroscopic data where only β-sheet structures have been identified. Evidently, the conformation of the fibril core and surface differs, which was used to propose possible growing mechanisms.[157,160]

TERS analysis of single DNA and RNA molecules intends to distinguish single nucleobases and conformations or to detect defects. An important prerequisite is the distinction of the individual nucleobases from each other as well as from the backbone, which was demonstrated in several works.[161−164,166] Nucleic acid studies often use stretched strands, and the substrate and its pretreatment play an important role. With a defined and reproducible sample preparation, a homogeneous orientation of the delicate sample on the substrate can be achieved. It was, e.g., found that the cation used to modify a mica substrate can influence the DNA conformation.[163] A first indicator was the change of the contour length of the strands. Spectroscopically, this was supported by the shape and position of the phosphate backbone bands.

Depending on the sites of the DNA/RNA strands facing the tip, nucleobases, phosphate, and ribose signals can be detected and differentiated.[161,162,164,166] Single stranded DNA/RNA can be immobilized via the phosphate backbone to a mica substrate with the nucleobases pointing upward. Since the detection depth of the evanescent field at a TERS tip apex decreases

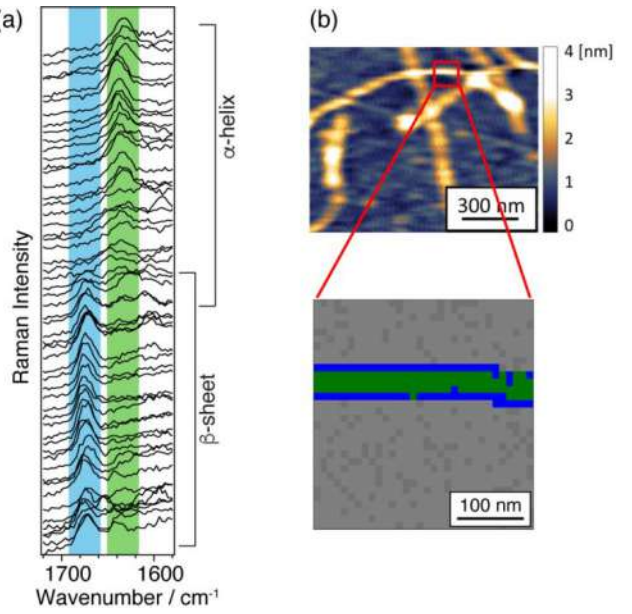

Figure 3. Monitoring the different secondary structures on single amyloid fibrils with TERS. (a) Spectra recorded on consecutive 0.5 nm distant measurement points across an amylin fibril show an α-helix to β-sheet structure transition by changes in the amide I band position. Reproduced from Nanoscale Heterogeneity of the Molecular Structure of Individual hIAPP Amyloid Fibrils Revealed with Tip-Enhanced Raman Spectroscopy, vandenAkker, C.; Deckert-Gaudig, T.; Schleeger, M.; Velikov, K. P.; Deckert, V.; Bonn, M.; Koenderink, G. H., *Small*, Vol. *11*, Issue 33 (ref 159). Copyright 2015 Wiley. (b) AFM topography and secondary structure imaging of an amyloid-b(1−42) fibril. α-Helix and β-sheet structures were identified by changes in the amide III band position. Reproduced from Direct Nanospectroscopic Verification of the Amyloid Aggregation Pathway, Lipiec, E.; Perez-Guaita, D.; Kaderli, J.; Wood, B. R.; Zenobi, R., *Angew. Chem. Int. Ed.*, Vol. 57, Issue 28 (ref 157). Copyright 2018 Wiley. In both experiments, α-helix structures are highlighted in green and β-sheet structures are highlighted in blue.

exponentially in such a configuration, bands from the nucleobases dominate the spectra. Adenine, cytosine, thymine, uracil, and guanine can be identified by the respective ring-breathing mode, which does not overlap with other bands. For single stranded DNA, it was demonstrated that adenine embedded between cytosine units can be directly identified.[162] On the other hand, if all four nucleobases build the sequence, a complex data processing procedure has been demonstrated to be indispensable.[161]

Resonance Raman Spectroscopy of Proteins and Nucleic Acids. When the wavelength of the excitation laser coincides with that of an allowed electronic transition of a chromophore, the intensities of certain Raman bands are enhanced. Along with the increased sensitivity, the selectivity also becomes enhanced, as only the vibrational modes from the chromophore that gives the origin of the electronic spectrum become augmented, while those from other parts of the molecule typically remain weak.

Molecular insights of rhodopsin, a prototypical photoactive protein, were obtained from steady state and time-resolved RR studies and discussed in a review.[167] This review also included UVRR investigations of soluble and membrane-associated biomolecules, including integral membrane proteins and antimicrobial peptides.

Cytochromes are hemeproteins that contain iron as part of the reaction center. Cytochrome c is one of the most common and

https://doi.org/10.1021/acs.analchem.1c03235
Anal. Chem. 2022, 94, 86−119

important enzymes since it plays a key role in the respiratory system of eukaryotes usually located in the mitochondria. The predominant Soret band of cytochrome c is located around 420 nm. The Q-band of the absorption spectrum exhibits a maximum around 530 nm. Therefore, RR excitation can be generated using blue or green laser radiation with associated RR bands near 1590, 1313, 1150, and 750 cm^{-1}. RR spectroscopy studies of cytochromes in living cells are usually carried out at low laser power of 2 mW or less and short exposure time in order to increase cell viability. RR spectroscopy was applied to quantify the redox state of the cytochromes b and c in a living *Saccharomyces cerevisiae* cell as well as in isolated mitochondria with labeling or genetic manipulation.[168] Photobleaching effects that occur during RRS of the cytochrome were also studied in living *S. cerevisiae* as a model organism.[169]

In the context of hemoglobin, RR spectroscopy is very sensitive to structural changes associated with O_2 and CO_2 bonding of the iron core because RR excitation mainly probes bonds involved in complexation. The most common and persistent application of RR spectroscopy on the cellular level has been in line with current research on malaria, one of the most spread infectious diseases.[9] During the progression of the disease, the *Plasmodium falciparum* parasite digests hemoglobin and releases heme. Free heme is toxic to cells, so the parasites convert it into an insoluble crystalline form called hemozoin, often referred to as malaria pigment. An elegant way to study hemozoin formation in the early developmental stages within single erythrocytes is called fiber array-based Raman spectroscopy.[97] The interaction of novel drugs[170] with heme target structures is thoroughly analyzed to understand the molecular action. Further signal amplification in studies of hemeproteins and those in biological systems can be achieved by combining RR spectroscopy with surface enhanced Raman scattering (SERS), which is called surface enhanced resonance Raman scattering (SERRS).[57]

Besides hemic metalloproteins, other metalloproteins and metalloenzymes such as iron−sufur (Fe−S), diiron, and copper proteins have been studied by RR spectroscopy to characterize the metal (active) site and elucidate the structure−function relationship. RR spectroscopy of Fe−S proteins and their redox properties were recently reviewed.[171] Lasers of wavelengths between 400 and 500 nm that match the energy of S → Fe charge transfer transitions selectively enhance modes involving the metal−ligand stretching vibration, which can be observed in the low wavenumber region (200−450 cm^{-1}). RR spectra have been found to be sensitive to the nature of Fe ligands. Besides the most common S ligand from the aromatic acids cysteine, these may include N provided by histidine and arginine, O originating from aspartic acid, serine, glutamic acid, or tyrosine and exogenous ligands. When a proper excitation wavelength is chosen, RR spectroscopy can simultaneously probe different types of clusters in the same protein. For instance, the $[3Fe\text{-}4S]^{1+}$ and $[4Fe\text{-}4S]^{2+}$ centers of ferrodoxin can be observed at the 413 nm laser line, while the $[3Fe\text{-}4S]^{1+}$ center is selectively enhanced at 458 and 514 nm.

UVRR spectra of proteins and nucleic acids are dominated by nucleosides (dA, dG, dC, and dT) and aromatic amino acids (Phe, Trp, and Tyr) as these constituents show electronic absorption in the wavelength range from 230 to 280 nm. Main UVRR bands and cross sections of H_2O and D_2O solutions of nucleosides and aromatic amino acids were reported for laser excitation wavelengths of 257, 244, 238, and 229 nm.[56] For brevity, data are given for nucleosides in H_2O: dA (main bands 730, 1173, 1208, 1250, 1310, 1336, 1375, 1424. 1482, 1506, 1580, and 1603 cm^{-1}), dG (main bands 682, 1030, 1080, 1180, 1322, 1361, 1410, 1485, 1535, 1575, 1603, and 1685 cm^{-1}), and dT (main bands 785, 1190, 1241, 1373, 1414, 1481, and 1655 cm^{-1}) show maximum UVRR intensities at 257 nm, whereas dC (main bands 784, 1293, 1527, and 1650 cm^{-1}) shows maximum intensities at 229 nm excitation. Analogously, data are also given for aromatic amino acids in H_2O: Trp (main bands 757, 880, 1010, 1131, 1238, 1340, 1360, 1460, 1550, 1575, 1616, and 1767 cm^{-1}), Tyr (main bands 830, 1178, 1209, and 1613 cm^{-1}), and Phe (main bands 1002, 1030, 1205, and 1602 cm^{-1}) show maximum intensities at 229 nm, and the cross sections of Phe are less intense by roughly a factor of 100.

In summary, when Raman spectroscopy is utilized, structural changes or changes in confirmation states in nucleic acids and proteins, e.g., due to variations in the pH value, can be monitored. Thus, information on the structure as well as the formation of clusters is gained. The potential of Raman spectroscopy is illustrated in the quality control of the synthesis of the oligonucleotides and in food analytics. In the case of the SERS-based detection of biomacromolecules, the interface between the sample of interest and the metallic nanostructure plays an important role. Here, variations in the orientation of the macromolecule toward the metallic surface result in different spectral profiles. SERS can be applied in observing hybridization events or the relative quantification of modifications in amino acids. Moreover, the native state of the proteins was observed by using PVP-modified gold nanoparticles. As an alternative to label-free SERS, immunoassays based on stable SERS tags as labels are common for the detection of proteins. To achieve a nanometer-scaled spatial resolution, TERS is performed and allows for the investigation of confirmation or chemical changes on the submolecular level. As a consequence, the formation of fibrils, i.e., β-sheet rich structures, can be identified in single constructs and the differentiation between the spectral fingerprint information on the nucleic acids, ribose, and phosphate backbone in a single DNA or RNA strand became feasible. Finally, RR spectroscopy is associated with the enhanced signal intensity of Raman modes in chromophores due to electronic transitions. For example, structural changes due to the complexation of hemoglobin with O_2 or CO_2 can be monitored. Moreover, this technique is applied in malaria research studies to detect hemozoin, the insoluble crystalline form of free heme, in cells. By means of RR spectroscopy, the redox state of metalloproteins or metalloenzymes can be investigated. Thus, a high variety of Raman-based detection schemes are available to shed light into molecular processes of biomacromolecules such as nucleic acids and proteins.

Investigation of Viruses with High Sensitivity and Lateral Resolution in the Nanometer Range. As the direct investigation of single viruses with conventional Raman spectroscopy is not possible due to the optical resolution and sensitivity limits, signal enhancing approaches and nanometer resolutions using near-field and scanning probe microscopic approaches are required to detect small quantities or even individual virus particles as achieved by the techniques SERS and TERS, respectively, even though there are various options to utilize the Raman method for the detection of viral infections[172−175] as summarized in Application of Raman-Based Techniques in Liquid Biopsy.

A SERS-based detection of viruses could be achieved via capturing nucleic acid molecules on SERS active surfaces by complementary DNA sequences[176] as introduced in the

https://doi.org/10.1021/acs.analchem.1c03235
Anal. Chem. 2022, 94, 86−119

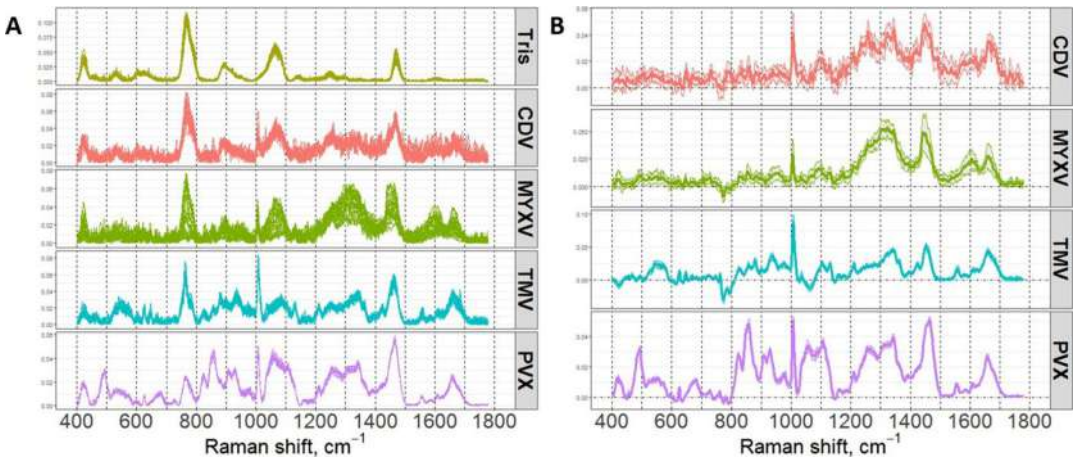

Figure 4. SERS spectroscopic fingerprint spectra of rabbit myxomatosis virus (MYXV), canine distemper virus (CDV), tobacco mosaic virus (TMV), and potato virus X (PVX). (A) SERS spectra without subtraction of the Tris control spectrum (background information). (B) Subtracted average SERS spectra ± the standard deviation. Reprinted from *Sens. Actuators, B*, Vol. *257*, Durmanov, N. N.; Guliev, R. R.; Eremenko, A. V.; Boginskaya, I. A.; Ryzhikov, I. A.; Trifonova, E. A.; Putlyaev, E. V.; Mukhin, A. N.; Kalnov, S. L.; Balandina, M. V.; Tkachuk, A. P.; Gushchin, V. A.; Sarychev, A. K.; Lagarkov, A. N.; Rodionov, I. A.; Gabidullin, A. R.; Kurochkin, I. N., Nonlabeled selective virus detection with novel SERS-active porous silver nanofilms fabricated by Electron Beam Physical Vapor Deposition, pp 37−47 (ref 182), Copyright 2018, with permission from Elsevier.

previous chapter on the detection of biomacromolecules such as DNA and RNA. However, the focus of this paragraph is on SERS methods for the investigation of the entire virus particle. Nanostructured SERS-active substrates are applied to detect viruses as multicomponent systems; however, many SERS sensor surfaces are lacking from reproducible SERS signal distribution and efficient signal enhancement.[177] To address this issue, gold nanostructures are fabricated on an indium tin oxide (ITO) substrate and fragmented antibodies were bound to the senor surface.[178] Then, HIV-1 virus-like particles were deposited on the surface, and due to the immunoreaction, they are bound to the gold nanopattern by the antibody fragments. Subsequently, the SERS spectra are recorded, which are dominated by typical marker modes of carbohydrates, proteins, and lipids. Concentration-dependent intensity variations are found for various Raman peaks. Moreover, gold nanoparticles were modified with antiflaviviral antibodies, and in the presence of Dengue as well as West Nile virus, the plasmonic nanoparticles are conjugated to the virus' surface.[179] As a consequence, hot spots are formed, and the authors recorded SERS spectra of the virus particles down to a concentration of 10 plaque forming units (PFU)/mL with high accuracy. As an alternative to enrichment of the virus particles on the SERS sensing surfaces employing antibodies, label-free SERS approaches were developed. A multilayered nanorod SERS array was developed to allow for a localization of virus particles in hot spots.[180] SERS spectra of three different strains of the influenza A virus were recorded, and fingerprint information was achieved for a concentration of 10^6 PFU/mL. Furthermore, porous carbon films modified with silver nanoparticles and SERS spectra of three different viruses were measured, demonstrating the potential in differentiating viruses based on their label-free SERS fingerprint.[181] Recently, a label-free SERS detection scheme was published to detect viruses qualitatively by using SERS substrates with nanoscale cavities.[182] The authors speculated that the virus particles are trapped in the pore-like structures, and they investigated four different virus species, i.e., rabbit myxomatosis virus (MYXV), canine distemper virus (CDV), tobacco mosaic virus (TMV), and potato virus X (PVX). In Figure 4, the representative SERS spectra of all investigated viruses before (A) and after (B) subtraction of the SERS spectrum of pure Tris solution are illustrated. The authors assigned all Raman modes to typical biomolecules such as amino acids, nucleobases, proteins, etc. By employing linear discriminant analysis, the authors showed the differentiation of the SERS spectra of all four viruses in different clusters and illustrated the potential of SERS for the qualitative detection of virus particles due to slight changes in the chemical composition.

When scanning probe microscopy in combination with signal enhancing processes, i.e., TERS, is employed, the investigation of even a single virus particle is achieved. The first TERS analysis on a virus particle was reported 10 years ago when the surface of a tobacco mosaic virus (TMV) was investigated.[156] In the near-field spectra along a single 20 nm thin and 200 nm long rod-shaped TMV, the contribution of RNA and proteins could be identified. In order to obtain comparable information in the far-field, high concentrations (mg/mL) are necessary; however, these are often not available or require time-consuming culturing. The studies have since been extended to other virus species, and it was demonstrated that it is possible to distinguish virus particles not only morphologically with the AFM technique but also by their chemical composition. For this purpose, viruses were selected with shells either containing solely proteins or having an additional lipid envelope.[154,155] A manual data evaluation enabled the assignment of the surface components by considering the different marker bands, which are ester and phosphate groups for lipids and amide bands and specific amino acids for proteins. In order to accelerate this process, an automated data evaluation procedure was developed that enabled the virus classification with an accuracy of 91%.[154]

In conclusion, due to the dimension of viruses, Raman investigations of single particles are hindered by the optical resolution and sensitivity limits. Therefore, SERS approaches are developed to enrich virus particles on metallic nanostructured surfaces to enhance the Raman fingerprint by several orders of magnitude. It was shown in literature that SERS spectra of various viruses could be differentiated by chemometrics, which is associated with the different chemical compositions of the viruses. Even the spectroscopic characterization of individual virus particles becomes feasible with the

https://doi.org/10.1021/acs.analchem.1c03235
Anal. Chem. 2022, 94, 86−119

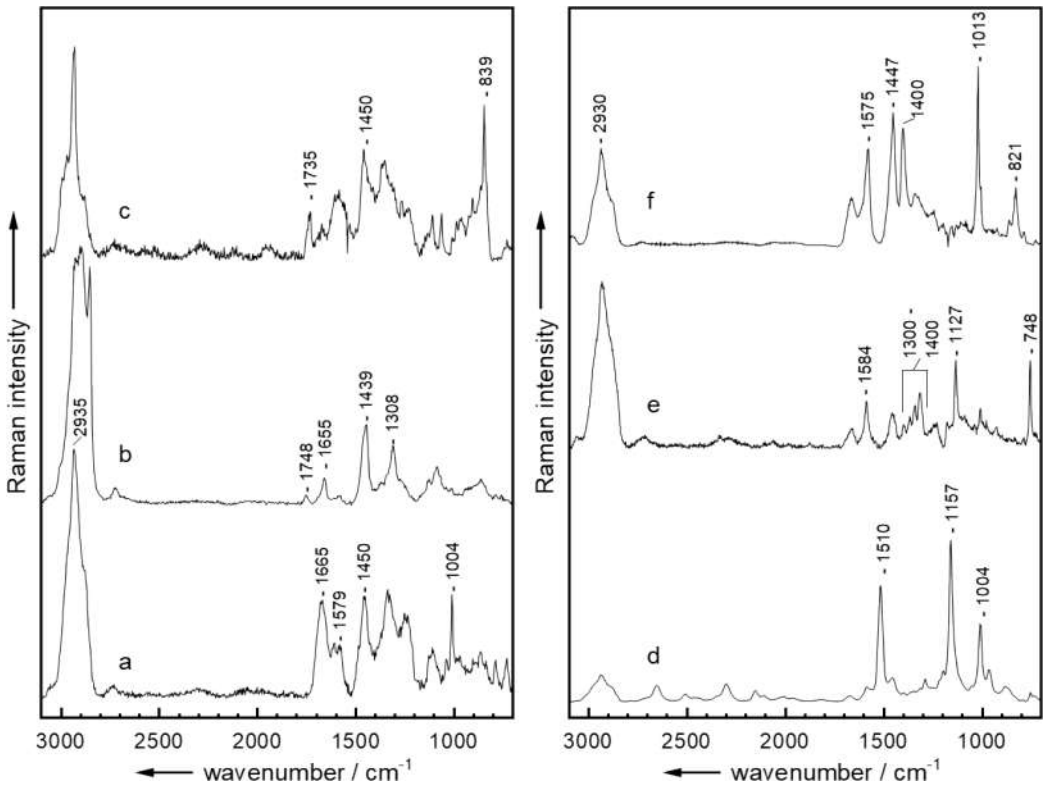

Figure 5. Examples of Raman spectra of single bacterial cells with an excitation wavelength of 532 nm: mean Raman spectra of vegetative cells (a); bacteria with an excess of lipids (b); PHB (c); carotenoids (d), or cytochrome (e); CaDPA in endospores (f).

application of TERS, allowing for an investigation with nanometer scale lateral resolution.

Raman Spectroscopic Characterization and Identification of Bacteria. When bacteria or other microorganisms are analyzed by means of Raman spectroscopy, a sum spectrum of all biochemical components in the sample volume is obtained. Therefore, the method is described as phenotypic, which holds true for Raman spectroscopy of biological material in general. In principle, a Raman spectrum of bacteria contains information about the main components of a cell as water, proteins, DNA/RNA, lipids, and carbohydrates. Figure 5a depicts a mean Raman spectrum of vegetative cells, which are normally growing bacteria capable of forming endospores, excited in the visible region with the C−H stretching vibration at 2935 cm^{-1}, the C−H deformation vibration at 1450 cm^{-1}, the C═C stretching vibration of adenine and guanine at 1579 cm^{-1}, and the amide I vibration at 1665 cm^{-1} as well as the ring breathing vibration of phenylalanine at 1004 cm^{-1}.[183] Nevertheless, when other laser excitation wavelengths are applied, there might be some differences in the Raman spectra mainly due to resonance effects.[184] Especially, when UV wavelengths are applied, only information on the DNA/RNA bases as well as aromatic amino acids are selectively enhanced. In addition, in this spectral region, fluorescence does not play a significant role.[184]

The excitation wavelength also defines the type of samples that can be measured. Normally for UV and NIR excitations, bulk samples are used, which require a sufficient amount of biomass and therefore a cultivation step. With sufficiently high optical magnification and visible light for detection of the Raman information, it is possible to analyze single bacterial cells.[184] Nevertheless, the Raman spectra of bacteria do not always exhibit the same signals as they are dependent on the metabolic state. In Figure 5, mean Raman spectra of bacteria with an excitation wavelength of 532 nm are depicted.[183] As already mentioned, spectrum a is a Raman spectrum from normal vegetative cells with information about the main cellular components, mainly protein and DNA. Spectra b−e show the Raman spectra of bacteria that exhibit a high amount of special substances. Raman spectrum b is nearly a pure (unsaturated) lipid signal, which can be very well observed on the special form of the C−H stretching vibration around 2930 cm^{-1} and the C═O stretching vibration of lipid esters at 1748 cm^{-1}. Since the Raman scattering cross section of lipids is very high, an increased lipid content may lead to such a spectrum. The bacterial spectrum c exhibit signals from a storage substance in this case polyhydroxybutyrate (PHB): The most characteristic marker bands for PHB can be found at 1735, 1450, and 839 cm^{-1}. Due to the resonance Raman effect, pigments might also be observable in the Raman spectra of bacteria. Spectrum d exclusively exhibits carotenoid signals around 1510, 1157, and 1004 cm^{-1}, which can be assigned to the ν(C═C), ν(C−C) and δ(C−CH$_3$) vibrations, respectively. Spectrum e belongs to bacteria with a high amount of cytochrome with characteristic signals at 1584, 1127, and 748 cm^{-1}. The last spectrum f belongs to *Bacillus* endospores. Here, the high content of calcium dipiculinate (CaDPA) in combination with the lack of water inside the endospores leads to the special spectral fingerprint. Especially, the signals at 1575, 1447, 1400 1013, and 821 cm^{-1} are typical for bacterial endospores.[183]

Since Raman spectroscopy is a phenotypic method, changes in the environmental condition such as cultivation age, temperature, pH, supplementary substances in the medium, light, etc. will influence the cell composition and therefore the Raman spectra.[183−185] Especially, the growth phases of liquid cultivation can clearly be observed by means of Raman spectroscopy.[186] Sometimes, these spectral variations are

https://doi.org/10.1021/acs.analchem.1c03235
Anal. Chem. 2022, 94, 86−119

especially pronounced when, e.g., carotenoids or lipids are produced at different time points during growth.[187]

The application of SERS to investigate bacteria lead to spectra that are normally very different from the Raman spectra of bacteria. Since there is a strong electromagnetic field on the SERS-active sensor surface, only the Raman fingerprint of the molecules in close proximity, which are a few nanometers, are enhanced. As a consequence, only selected areas of the bacteria, mostly the outer cell wall, contribute to the SERS spectra. Therefore, Zeiri et al. established protocols to synthesize silver colloids at different locations inside or outside the bacterial cell probing different cell regions.[188] In addition, different SERS substrates lead to variations in the SERS signals.[189] Therefore, it is mandatory to understand the influence of probing location and SERS substrate on the SERS spectra of bacteria.[190] In order to shed light on the dominant contributions from cellular components in SERS bacterial spectra, SERS spectra of bacteria were fitted by using SERS spectra of the single components adenine, xanthine, hypoxanthine, and guanine as well as uric acid and adenosine monophosphate.[191] Thus, the authors concluded that their presence in the outer cell wall is associated with degradation processes as a result from starvation of the investigated bacteria. Again, it illustrates that SERS spectra of bacteria are dominated by only a few substances, and it will not provide information on the entire chemical composition. The classification of SERS spectra recorded from 12 bacterial strains from urine samples of urinary tract infection patients illustrates the potential of SERS in clinical applications.[192]

Most studies concerning Raman spectroscopy and bacteria try to identify bacteria either from culture or from environmental, food, or patient samples. For cultivation-free Raman studies on such complex samples, an appropriate isolation step that does not alter the chemistry of the bacterial cells is necessary.[185] For example, for samples with only a few additional components besides the bacteria, capture molecules like siderophores[193] or antibodies[194] can be used for isolation. For samples with a high load of other nontarget cells such as whole blood, a combination of enzymatic digestion and centrifugation seems most suited.[195]

Raman spectroscopic identification of bacteria first requires a database of the Raman spectra from the bacteria of interest. Here, the cultivation respective isolation should be closely adapted to the estimated sampling procedure. For the database, enough biological and technical replicates should be included to guarantee a representative data collection. In addition, independent replicates should be used to validate the database, and finally, an identification step with the real samples from the environment, food production, medical treatment, etc. should be taken.[183]

Databases have been established to, e.g., differentiate 31 different *Acinetobacter baumanii* strains from culture.[196] A more complex database first differentiates 26 *Mycobacteria* spp. from non-*Mycobacteria* spp. Afterward, the database distinguishes between bacteria from the *M. tuberculosis* complex and non-*M. tuberculosis* bacteria, while the species of the two clusters are identified next. Afterward, independent strains of *M. tuberculosis* and other *Mycobacteria* were used for a successful identification.[197] Another approach directly localized *M. tuberculosis* in frozen tissue sections of guinea pigs. With this method, also lipid rich and lipid poor phenotypes of *Mycobacteria* can be distinguished, which allows an estimation of the resistance capability of the bacteria.[198]

For complex databases, also the isolation step needs to be included in the sample preprocessing part. On the basis of *Burkholderia* spp., it could be shown that it is possible to isolate a single bacteria from animal feed and to identify them afterward. A two-stage classification first differentiates between ten species of *Pseudomonas* and *Burkholderia* and afterward discriminates the very closely related *B. mallei* and *B. pseudomallei*. The quality of the data set was evaluated with the help of independent strains.[199,200]

Apart from the identification of pathogens, it is often mandatory to receive information about possible resistances against antibiotics since this will lead to an adaptation in the medical therapy. The combination of dielectrophoresis and Raman microscopy analyses the effect of an antibiotic on a special isolate and therefore simultaneously detects possible resistances and the minimal inhibitory concentration within 2 h.[201]

Isotope labeling can be applied to monitor all sorts of metabolic activity of bacterial cells. Due to the change in mass, the heavier isotopes shift the respective signal positions to lower wavenumbers. Therefore, the uptake of ^{2}H, ^{13}C, ^{15}N, or ^{18}O of metabolic precursors, e.g., sugars or amino acids, leads to very special changes in bacterial spectra.[183] Such changes in isotopic labeled cells can then be used to monitor different metabolic activities.[202] The application of D_2O for example allows one to differentiate between metabolic active and inactive bacterial cells in groundwater[203] or which bacterial species is most suited to degrade carboxymethylcellulose[204] or to solubilize phosphor.[205] The use of labeled $^{15}N_2$ allows one to distinguish nitrogen-fixing bacteria from other cells by evaluating the cytochrome signals.[206] In addition, when the bacteria are cultured with ^{2}H and ^{13}C labeled carbon sources, the method can also determine which carbon source is preferentially metabolized by certain species.[207] The same approach can be used to study metabolic interactions between two different species and therefore the interaction in microbial communities.[208]

Overall, the different Raman spectroscopic approaches have various possible applications. On the one hand, bacteria can be characterized and their spectral change can be observed due to variation in their cultivation or environment. On the other hand, Raman spectroscopy can be used to set up databases for the rapid and reliable identification of bacteria.

Spontaneous Raman Spectroscopy for the Analysis of Eukaryotic Cells. One of the most common applications of Raman spectroscopy in biology is the label-free characterization and classification of eukaryotic cells. The advantage of the method is that the cell characterization and differentiation can be solely performed on the basis of the intrinsic macromolecular fingerprint of the cell without the need for labeling or other cell preparation steps, and it is nondestructive. Because the differentiation and characterization depends only on the intracellular composition, a single device can be used to perform a variety of applications, such as the classification of cell types, e.g., stem cells,[209] and characterization of the drug−cell interaction,[210−212] intracellular lipodomics,[213,214] and others.[215−218] The informational wealth can be extracted through sophisticated machine learning approaches, which are widely established in the Raman community.

One of the current hot topics is the application of Raman spectroscopy to differentiate stem cells and to identify the developmental stage of these cells without the need for genetic manipulation or utilization of exogenous markers, as current enrichment procedures require staining or genetic modification of the cells. Here, a label-free and nondestructive approach would be significantly advantageous. For example, a significant

https://doi.org/10.1021/acs.analchem.1c03235
Anal. Chem. 2022, 94, 86−119

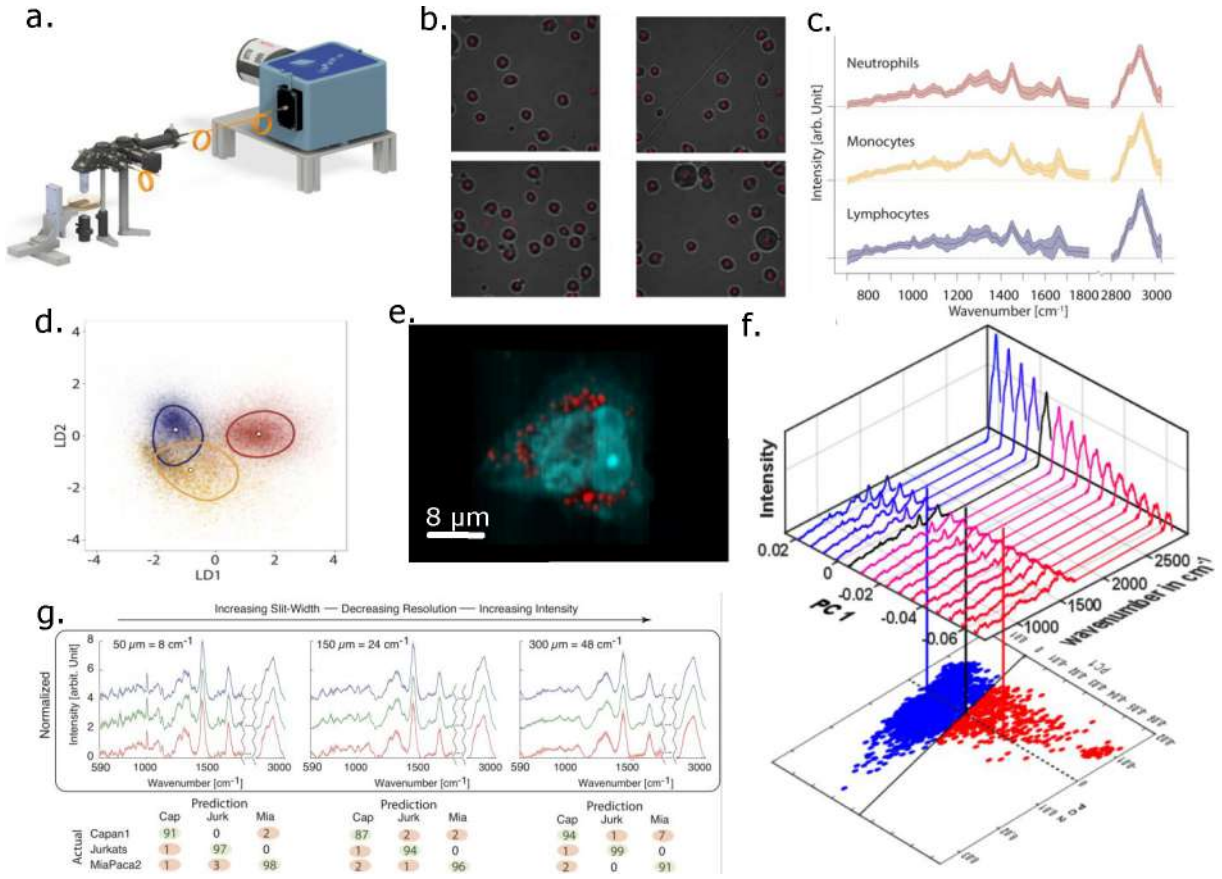

Figure 6. Raman spectroscopy offers abundant possibilities for single cell analysis. High-throughput screen Raman spectroscopy system, which allows the acquisition of thousands of cells in a short time (a). Reproduced from Schie, I. W.; Rüger, J.; Mondol, A. S.; Ramoji, A.; Neugebauer, U.; Krafft, C.; Popp, J., *Anal. Chem.* **2018**, *90*, 2023−2030 (ref 227). Copyright 2018 American Chemical Society. Cells are automatically recognized on a brightfield image and measured without human intervention (b). Mean Raman spectra from thousands of leukocytes for three different types acquired on the HTS-RS system (c). Multivariate statistical analysis shows that these cells are easily separated on the basis of the molecular signatures (d). Raman images enable the visualization of intracellular distribution of different macromolecules (e). Reprinted by permission from Springer Nature, *Anal. Bioanal. Chem.*[214] (Complexity of fatty acid distribution inside human macrophages on single cell level using Raman microspectroscopy, Stiebing, C.; Matthäus, C.; Krafft, C.; Keller, A.-A.; Weber, K.; Lorkowski, S.; Popp, J.), Copyright 2014. A Raman-based viability assay can easily differentiate viable and nonviable cells (f).[230] Examples from low-resolution Raman spectroscopy for the characterization of three different cell types shows that even with a reduced spectral resolution cells can be differentiated, enabling the implementation of low-cost high-throughput systems (g). Reproduced from Cell classification with low-resolution Raman spectroscopy (LRRS), Schie, I. W.; Krafft, C.; Popp, J., *J. Biophotonics*, Vol. 9, Issue 10 (ref 224). Copyright 2016 Wiley.

challenge to develop a specific type of hematopoietic cells for the treatment of blood cell pathologies is the identification of the combinations of cellular and matrix indications that direct hematopoietic stem cells (HSC) to self-renew or differentiate into cell populations *ex vivo*. To address this problem, Ilin et al. identified discrete cells along the HSC differentiation hierarchy via multivariate analysis of Raman spectra.[219] Raman spectroscopy allowed a lineage-specific state differentiation of cells of four subpopulations independent of the stiffness of the underlying biomaterial substrate. Ichimura et al. observed noteworthy molecular differences in the spectroscopic fingerprint in the cytosol and nucleus in different mouse cell lines, indicating that Raman spectra reflect differences in the cell state.[220] Moreover, the researchers observed subtle changes, which were visualized using principal component analysis (PCA), in the molecular fingerprint of cells at different cell states before and after the induction of differentiation in neuroblastoma and adipocytes, showing transition in the cell states during differentiation. Brauchle et al. used Raman spectroscopy to differentiate stem-cell derived cardiomyocytes (CMs) for disease modeling and clinical therapies.[221] In that study, the researchers demonstrated that Raman spectroscopy can noninvasively identify embryonic stem cell (ESC)-derived chamber-specific CMs and monitor cell maturation. It was also possible to identify Raman bands for atrial and ventricular CMs, and ESCs were successfully discriminated from their cardiac derivatives. Because of the supreme molecular resolution, Raman spectroscopy offered a distinct analytical characterization for differentiating cardiovascular cell populations.

Chiang et al. investigated osteosarcoma cells and the development of the differential production of mineral species, which allowed them to accurately assess the grades of osteosarcoma cells by evaluating their mineralization levels.[222] Hashimoto et al. used line-scanning Raman microscopy to determine mineralization in living cells and in a time-lapse fashion.[223] Fiber array-based Raman spectroscopic wide-field imaging was developed for chemical selective imaging of red blood cells. This new imaging approach was trained with a robust algorithm and allows a chemical selective analysis of the malaria pigment hemozoin in early ring stages of *Plasmodium*

https://doi.org/10.1021/acs.analchem.1c03235
Anal. Chem. 2022, 94, 86−119

falciparum infected erythrocytes.[97] FERS was also proven to be suitable for detecting blood cells. Khetani et al. reported the ability to monitor and differentiate between live, apoptotic, and necrotic leukemic cells,[40] whereas Yan et al. measured live erythrocytes.[43]

A common wisdom in Raman spectroscopy of biological samples is that the acquisition has to be performed at a very high spectral and spatial resolution to determine the precise molecular constituents of a sample. To satisfy those requirements, several sacrifices in terms of throughput have to be accepted, limiting the applicability of the method for a large-scale characterization of cells.[215] To investigate and reflect on the requirement of spectral resolution to differentiate different cell types on the basis of their molecular fingerprint, Schie et al. validated the classification performance for different degrees of spectral resolution.[224] In this publication, the researchers showed that low-resolution Raman spectroscopy (LRRS) can be used to differentiate different cell types, concluding that the spectral resolution does not significantly affect the performance of the classifiers to differentiate cells, and in many situations, a low spectral resolution, i.e., down to 60 cm^{-1}, can suffice. The advantage is eminent, as on the one hand, the signal gain through the reduced resolution can be significantly increased, up to 10-fold in the present publication, allowing one to significantly reduce the acquisition time. On the other hand, the reduced requirement for the spectral resolution also enables the implementation of cheaper and more compact devices, as was shown by Chen et al.[225] In another publication by Schie et al., the researchers characterized the influence of the spatial sampling of cells and the influence on the predictive model performance.[226] Most commonly, Raman images of entire cells are acquired, resulting in extended acquisition times on the order of minutes and reduced sample throughput. To overcome this issue, the researchers developed an approach for a rapid scanning of a diffraction-limited beam over a cell to rapidly determine the mean spectral information, showing that the mean spectra, which characterize the entire cell, can be acquired very rapidly and significant increase the throughput.

While there is potential for using Raman spectroscopy as a multifunctional and comprehensive method, which can be used for a large number of applications, the translation has rather been slow. Some of the key factors include the low sample size, the complex data acquisition procedure, and the frequently presented unrealistic application conditions. Additionally, complex and prolonging data preprocessing and analysis contribute to the slow translation. To overcome a few of those factors, Schie et al. have proposed a new fully automated data sampling strategy, which enabled them to sample a large number of cells, extending the potential applicability of the method and making it more attractive for unexperienced users, as depicted in Figure 6a–d.[227] The newly developed platform, befittingly coined high-throughput screening Raman spectroscopy (HTS-RS), enables the acquisition of thousands of cells in a short amount of time, significantly offsetting previously reported sample sizes. While traditional Raman devices always require a trained user to perform the experiments, the researchers fully automated the sampling of eukaryotic cells randomly distributed on a substrate. The potential of the novel platform was demonstrated by molecularly sampling of more than 100 000 cells of three different leucocyte classes to develop a model for the differentiation of leucocyte mixed populations. This model was applied to a mixed population of leukocytes from multiple healthy and diseased donors, achieving comparable results to standard staining-based approaches, but it is only based on intracellular molecular composition. In the same publication, the researchers also differentiated spiked tumor cells present in a mixture of leukocytes, precisely establishing the spiked-in ratios. This research shows that Raman spectroscopy can be used to sample a large number of cells and can provide characteristic molecular information from cells that can be used for a differentiation. In a follow-up publication, Rüger et al. applied the same approach for a large-scale sampling of diatom cells, characterizing the effect of pigment-modifying drugs.[228] Mondol et al. also showed that the newly proposed approach is also highly suitable for the characterization and differentiation of pollen; the researchers created a sample size of 37 different classes with each class containing more than 1000 samples.[229]

While the presented approach moves Raman spectroscopy closer to wider accessibility, it does not use the full potential of the methods as it cannot address a variety of possible and very common applications, for example, applications where cells are present under different physiological conditions, as is commonly occurring in studies investigating drug cell interaction, ionization, or any other physiological influence on cells. Here, an extension to the HTS-RS approach was proposed by Mondol et al., high-content screening Raman spectroscopy (HCS-RS), which allows the characterization of cells under different physiological conditions (see Figure 6f).[230] The application of this newly developed platform was demonstrated for the label-free determination of viable from nonviable acute monocytic leukemia derived THP1 cells. Here, measurements were performed in a mixed population and cell under four different drug−concentration treatments for two batches. For all measurements, the proposed Raman-based approach was able to reproduce nearly identical values as from parallel staining approaches. One has to keep in mind that the entire experiment was performed consecutively and fully automatically on all the batches, significantly reducing the hands-on requirement for the user and further moving the method closer to clinical laboratories. In another follow-up publication, the researchers used the same approach for predicting the drug−exposure concentration in individual cells exposed to panitumumab, a monoclonal antibody, which binds to the EFG-proliferation receptor.[231]

The recent developments indicate that Raman spectroscopy is currently in a state of transition, where the method finally becomes more applicable and operational not only by the experienced user but also by the everyday biomolecular researcher.

Spontaneous and Coherent Raman Microscopy in Cell and Tissue Imaging. Although single-point Raman spectra provide sufficient information to characterize biomedical samples for some applications, the study of heterogeneous samples such as single cells or histopathological tissue sections requires one to acquire images to assess cellular details or delineate tumor margins. Raman imaging acquisition strategies were comprehensively reviewed,[215] and details can be found therein. The applications of Raman imaging to biological cells and tissues were summarized with the focus on the period from 2012 to 2016.[216] Here, a brief overview of Raman imaging techniques and key papers in the context of tissue are given.

The first imaging approach, which is most commonly used, scans the laser spot along a predefined raster across the sample and collects a Raman spectrum at each point on a multichannel detector. A hyperspectral data set is generated with one dimension representing the spectral information and two or

https://doi.org/10.1021/acs.analchem.1c03235
Anal. Chem. 2022, 94, 86−119

three dimensions representing $x-y$ coordinates for a lateral raster or $x-y-z$ coordinates adding axial information in confocal collection geometries. Due to the typically small Raman scattering cross-section of tissues and the resulting low signal yield, the total exposure time to collect extended Raman images in this acquisition mode is relatively long. With one second exposure time per spectrum, images comprising up to 3600 data points can be collected. In real scenarios, the number is smaller because extra time should be added to read out the CCD and move the sample to the next position. One way to increase the acquisition speed of Raman imaging is to generate a laser line focus and collect Raman spectra in parallel at each pixel of a two-dimensional detector. As the laser intensity is distributed along the line, more intense lasers can be used without exceeding the damage threshold. The damage threshold depends on several factors including the type of tissue (with or without chromophores), the sampling geometry (dried or nondried in aqueous buffer), laser wavelength and the power density (W per cm^2), which is determined by the laser intensity, pulse duration, optical magnification, and the laser focus spot. Another way to increase the acquisition speed of Raman imaging is wide-field imaging, also known as global imaging. Here, the sample area is illuminated at once, and the Raman signal of a selected wavenumber interval is detected on a two-dimensional detector. The wavenumber interval can be selected by narrow band dielectric filters or tunable filters that enable one to collect consecutive spectral information. In addition, the concept of light sheet illumination was transferred to wide-field Raman imaging. Light sheet Raman microspectroscopy was realized with an imaging spectrometer, an interferometric principle for spectral registration, and a light sheet illumination microscope.[232] This technique was applied for three-dimensional (3D) imaging of a zebrafish eye. The 3D stack contained 50 hyperspectral images (17 min of exposure for each slice with a field of view $325 \times 325\ \mu m^2$) and was analyzed by a non-negative matrix factorization (NMF) algorithm. This method was more than 5 times faster than conventional approaches, while reducing the local excitation intensity over 300-fold. Selected slices are shown in Figure 7. Finally, Raman images were collected with a 20×20 array that were coupled to a multichannel spectrograph via fibers.[233] This modality enabled fast imaging of $1 \times 1\ mm^2$ without stepwise scanning. 400 fibers were arranged along a line, focused on the entrance slit, and dispersed on a 4096×4096 pixel CCD camera. A Raman image of porcine skins was acquired in less than 1 min.

The lateral resolution depends on the pixel size that is determined in the most common raster scan mode by the laser focus diameter and the step size. At a step size of 2 μm and 785 nm single mode laser excitation, cellular details including cell nuclei were resolved in Raman images of brain tumor tissue sections.[234] The nondried tissue sections were immersed in aqueous buffer, which prevented dehydration-induced denaturation of nucleic acids, proteins, and lipids and gave a higher contrast of cell nuclei due to more intense nucleic acid bands compared to Raman images of dried tissue sections. The data sets were decomposed by hyperspectral unmixing into endmember vectors that represent the spectral features and abundance images that represent the distribution and concentration of each component. Both morphological details and quantitative chemical parameters correlated well with the malignancy of glioma brain tumor specimens. A similar Raman spectroscopic imaging approach was applied to gain new insight into the depth-dependent arrangement of native and tissue

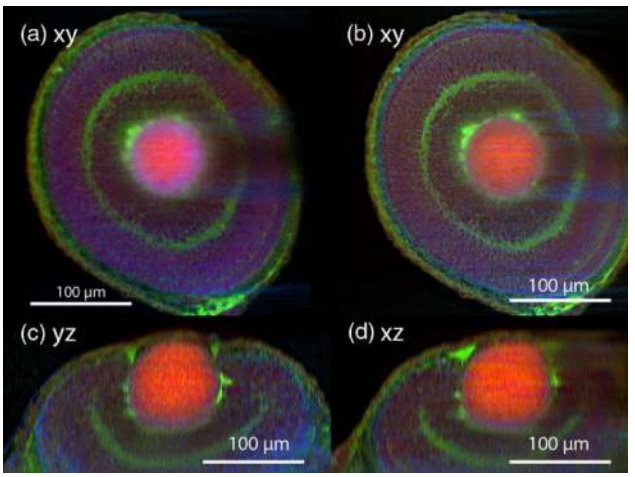

Figure 7. Unmixed 3D Raman image of a zebrafish eye. Corresponding color images of three NMF channels: (red) collagen-like fingerprint, (green) lipid-like fingerprint, and (blue) DNA-like fingerprint. (a) Image NMF result at 4.4 cm^{-1} spectral resolution. (b) Selected *xy* slice of the 3D hyperspectral image stack at 18 cm^{-1} resolution after NMF-based unmixing and 3D deconvolution of each color channel. (c) Selected *yz* slice. (d) Selected *xz* slice. Reprinted with permission from ref 232. Copyright 2016 The Optical Society.

engineered articular cartilage.[235] Raman imaging results at 2 μm step size reported tissue complexity into at least six zones on the basis of the analysis of the distribution and orientation of the main extracellular matrix (ECM) components. Further, Raman images revealed changes in the collagen, glycosaminoglycan, and water distributions in tissue engineered constructs over time. Raman imaging at 0.8 and 3 μm step sizes was used to study the interplay between atherosclerosis and medical calcification in the human aorta.[236] Raman images characterized the cross-sectional distributions of the predominant minerals, apatite and whitlockite, the associated ECM, and cellular changes between atherosclerotic and nonatherosclerotic aortic tissues.

At a step size of 10 μm, cellular details could not be resolved any more in dried tissue sections of brain tumor metastases.[237] As both x and y dimensions are reduced five times, the Raman image contains 25 times less spectra or Raman spectra with the same number of spectra covering larger regions of interest compared to imaging at 2 μm. A hierarchical classification scheme identified as the first step tumor tissue in the Raman image and determined the primary tumor of the brain metastases as the second step using the tumor tissue data as input. A multimodal spectral histopathology (MSH) approach was proposed to detect basal cell carcinoma at the surface of surgically resected skin tissue.[238] This approach combined tissue autofluorescence imaging for rapid prescreening of whole tissue sections and Raman microspectroscopy for sparse sampling of small regions, which is 1 or 2 orders of magnitude faster than collecting a full Raman image. A fully automated instrument was developed on the basis of MSH for clinical use.[239] Interinstrument transferability of diagnostic models was demonstrated as an important step on the clinical translation path. This technique can also diagnose the presence or absence of tumors in unsectioned tissue layers, thus eliminating the need for tissue sectioning.

Following the motto "an image tells more than 1000 words", Raman imaging provides thousands of spectra with thousands of data points. Raman imaging of large patient cohorts will result in big data that have been analyzed by chemometric algorithms.

https://doi.org/10.1021/acs.analchem.1c03235
Anal. Chem. 2022, 94, 86−119

Such data are also highly attractive for approaches using machine learning and artificial intelligence in the future. Advances in instrumentation such as dedicated lasers and large area electron-multiplying CCD (EMCCD) or CMOS detectors with rapid readout might reduce the exposure time by 1 order of magnitude, which still cannot be considered as high throughput. Sparse sampling of Raman spectra in combination with a rapid imaging modality would be the method of choice for clinical translation. Imaging modalities based on coherent Raman scattering are extremely promising in this context and will be presented next.

Coherent Raman scattering-based imaging methods are becoming routinely used in biomedical imaging applications due to the ability to visualize the distribution of label-free marker molecules. Taking advantage of the 3D-imaging capability of nonlinear microscopy in general, one can produce a 3D image of whole tissue volumes. When the 3D imaging method is combined with optical clearing, the penetration depth can be further increased to more than 1 mm in mouse brain.[240]

In order to selectively visualize marker molecules with high sensitivity, Raman labeling approaches are increasingly used. When deuterated glucose is applied, the metabolic dynamics of macromolecules synthesized using deuterated glucose can be studied in detail, specifically DNA, proteins, lipids, and glycogen. In a mouse model, a limit of detection of 10 mM for C−D bonds has been realized.[241] Similarly, heavy water D_2O or deuterated amino acids can be employed to visualize metabolic processes in animal models like mice, zebrafish, or *C. elegans*.[242] Raman labeling is, however, not always required to visualize a marker molecule. Recently, the spatial distribution and concentration of the neurotransmitter acetylcholine has been investigated by SRS directly in muscle tissue. The neurotransmitter relays neural excitation from motor neurons to muscles. In frog muscle, choline concentrations decrease after excitation from 12.9 to 5.7 mM.[243]

A major field of application of coherent Raman imaging to tissue is for the investigation of diseases of the brain. In the case of Alzheimer's disease, amyloid plaques play a key role. SRS has been shown to enable discriminating misfolded proteins by a characteristic spectral blue shift of ∼10 cm^{-1} of the amide I Raman band.[86] Human brain tumor infiltration has also been studied in detail using CRS imaging tools.[84,244] When parameters like axonal and nuclear density and the protein/lipid ratio are quantified, brain tumors can be automatically detected with 97.5% sensitivity and 98.5% specificity.[84] Also, the degradation of the peripheral nerve occurring in amyotrophic lateral sclerosis (ALS) has been analyzed using SRS imaging. Using a mouse model of ALS, the first signs of nerve degradation could be detected preceding any physiologically symptoms.[245]

CRS imaging also in combination with other nonlinear imaging tools like second harmonic generation (SHG) and two-photon excited fluorescence (TPEF) has been shown to be a valuable tool for cancer imaging, e.g., for head and neck cancers. A decrease in lipid signal is detected in head and neck cancer. In ovarian cancers, lipid desaturation has been detected in ovarian cancer stem cells, which not only is possibly a metabolic marker for this type of cancer but also can be used as a therapeutic target.[246] Also, in human prostate cancer, changes in the lipid metabolism have been detected using CRS. Here, cholesteryl ester accumulations were observed, which are induced by a loss of the tumor suppressor PTEN and the subsequent activation of PI3K/AKT.[247] For clinical use, it is beneficial to convert CRS false color images into images with a color scale similar to histologic images using digital staining. This approach was demonstrated for gastrointestinal cancer,[248] brain tumors,[85] and colon cancer.[249]

Driven by novel technical developments, e.g., robust and powerful laser sources and compact endoscopic probes, CRS imaging will soon enter routine clinical use. CRS is compatible with other nonlinear imaging tools like multiphoton fluorescence, fluorescence lifetime, second and third harmonic generation, and sum frequency generation, such that manifold information on native tissue structure and composition can be simultaneously obtained. In particular, spectrally resolved coherent Raman imaging using fast spectrally switchable light sources is the ideal tool for label-free monitoring of any molecular marker of interest and even to colocalize a combination of molecular markers in real time. In combination with vibrational labeling (see Stimulated Raman Scattering (SRS)), even the spatial distribution of molecular markers of low concentration can be analyzed, such that CRS imaging is the most versatile method for clinical use providing label-free imaging with diffraction limited spatial resolution at a video rate.

***In Vivo* Applications of Raman-Based Methods.** As outlined in the previous section, Raman modalities are promising techniques for investigating biological tissue *ex vivo* in the form of biopsies or thin sections. To transfer the benefit of Raman spectroscopy into the clinical environment, in the past two decades, efforts toward clinical *in vivo* studies have been made and are the focus of many researchers. Fiber-based endoscopic alternatives for the typically performed *ex vivo* microscopic work are necessary to reach inner organs and tissue sites. Hence, the design and development of fiber-optic Raman probes is receiving a lot of attention. Mostly, single-point acquisition is implemented although many studies are directed toward multimodal approaches to combine image visualization and guidance with the chemically sensitive Raman technique.[250] This section aims to review *in vivo* Raman studies over the past five years.

Raman probes are often tailored for a specific application, which leads to a large number of configurations as already outlined in a Linear, Spontaneous Raman-Spectroscopic Techniques. Due to the easy accessibility using routine clinical endoscopy systems, many studies can be found surrounding the investigation of the gastrointestinal tract.[251−253] Highly active in this field is the group of Huang, who developed a beveled fiber-optic Raman probe to measure the fingerprint and high-wavenumber region of Raman spectra in contact mode at 785 nm excitation.[254−256] In a large scale clinical study, 157 patients undergoing gastroscopy were investigated in order to discriminate intestinal metaplasia.[254] The authors detected Raman signal reductions of collagen, lipid, and aromatic amino acid bands, while typical protein bands at 1655, 1445, and 1335 cm^{-1} increased in intestinal metaplasia compared to normal gastric tissue. In a study of 191 gastric patients, Wang et al. investigated gastric dysplasia as a precursor for gastric cancer by measuring different *in vivo* locations including normal, dysplastic, and cancerous gastric tissue (adenocarcinoma).[255] Using a partial least-squares-discriminant analysis (PLS-DA) model, they reached a significantly higher specificity of 99.5% for classifying precancerous dysplasia from normal gastric tissue compared to standard white light reflectance endoscopy (WLR) with 51%, while having the same sensitivity of 90.9%. The same was found by Bergholt et al. for the diagnosis of adenomatous polyps during colonoscopy, where Raman endoscopy reached a specificity of 83.3% and WLR colonoscopy, only 16.7%.[256] A different

https://doi.org/10.1021/acs.analchem.1c03235
Anal. Chem. 2022, 94, 86−119

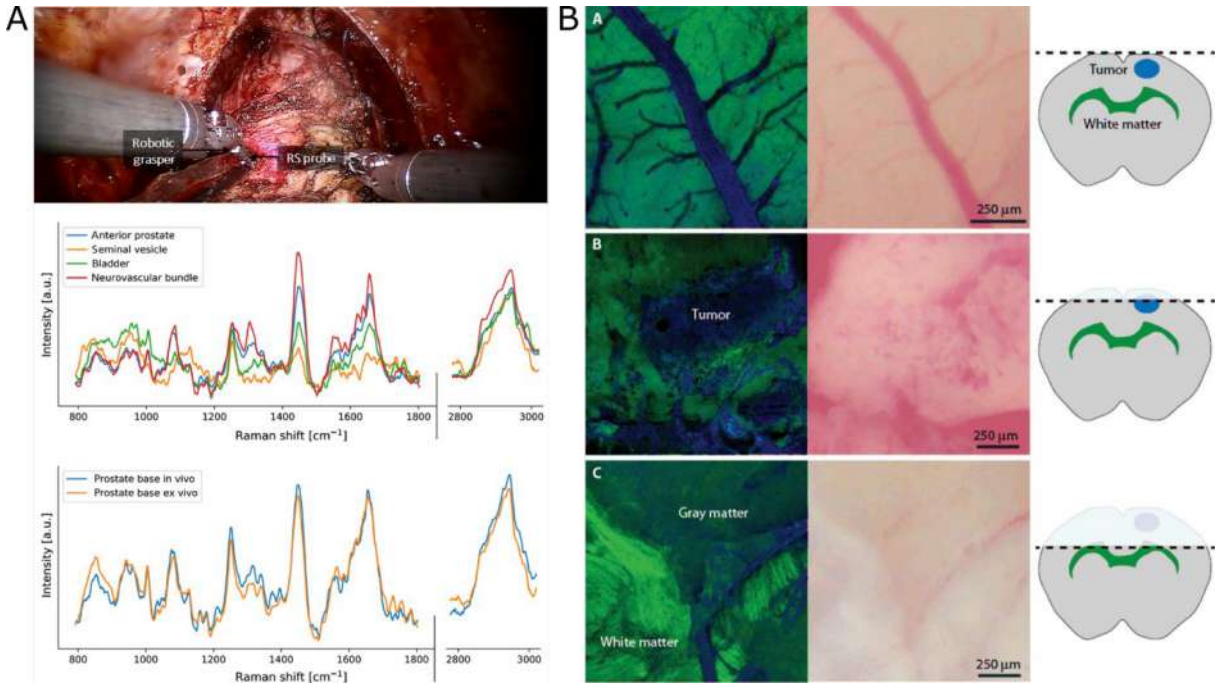

Figure 8. (A) Integrated Raman probe in a robotic-assisted surgical system during radical prostate resection with Raman spectra at different locations and comparison of spectra acquired *in vivo* and *ex vivo*. Reprinted under a Creative Commons Attribution 4.0 International License from ref 263. (B) SRS and brightfield images at different layers during *in vivo* simulated tumor resection in a human glioblastoma xenograft mouse model. From Ji, M.; Orringer, D. A.; Freudiger, C. W.; Ramkissoon, S.; Liu, X.; Lau, D.; Golby, A. J.; Norton, I.; Hayashi, M.; Agar, N. Y.; Young, G. S.; Spino, C.; Santagata, S.; Camelo-Piragua, S.; Ligon, K. L.; Sagher, O.; Xie, X. S., Rapid, Label-Free Detection of Brain Tumors with Stimulated Raman Scattering Microscopy, *Sci. Transl. Med.* **2013**, *5*, 201ra119 (ref 271). Reprinted with permission from AAAS.

approach to reach higher sensitivity and specificity was chosen by Lin et al., who combined four modalities into one endoscopic system to classify nasopharyngeal cancer.[257] The endoscopic system implemented white light and autofluorescence imaging to guide Raman as well as diffuse reflectance spectroscopy to obtain molecular specific information. The choice of a multimodal approach can speed up the measurement process by receiving an image-based overview, while selectively measuring the inherently weak Raman signal only at suspicious regions. A high potential was also demonstrated in the combination of optical coherence tomography and the Raman technique.[258,259]

Large patient data sets are needed to build robust algorithms for the identification and discrimination of cancerous lesions, but it is also important to consider variations between subjects, e.g., gender and age, and variations in anatomical sites of healthy tissue.[260,261] Although these studies showed anatomical variations in the Raman data of healthy tissue, Bergholt et al. further demonstrated that the transformation in cancerous colon tissue resulted in more pronounced differences, leading to an initial separation of cancerous vs healthy tissue.[262]

An important factor for the acceptance of new techniques in the clinical environment is the implementation in routinely used devices. Pinto et al. integrated a dual Raman system into a robotic-assisted surgical system (daVinci Xi, Intuitive Surgical), which is used in operating rooms for minimally invasive surgical procedures.[263] The Raman endoscope was designed so that the robotic arm can grasp, manipulate, and immobilize the probe, which was validated on a phantom. In an *ex vivo* and *in vivo* setting, Raman data during and after radical resection of the prostate were acquired and displayed in real time after spectral preprocessing (Figure 8A).

While most *in vivo* Raman studies analyze the difference between cancer and healthy tissue, another approach can be the time-dependent monitoring of biochemical changes. O'Brien et al. examined the cervix of 68 healthy women throughout pregnancy and postpartum repair to investigate significant changes during the preparation for delivery and develop a noninvasive risk assessment for preterm birth.[264] A commercial fiber probe with an excitation wavelength of 785 nm was used. During pregnancy, an increase in blood related bands between 1530 and 1600 cm^{-1} showed an increased vascularization, while extracellular matrix proteins (e.g., collagen) and carotenoids decreased. Postpartum, bands corresponding to extracellular matrix proteins returned to early pregnancy levels.

In vivo Raman studies on nonhollow organs are also conducted, where alternative approaches to endoscopy are tested, e.g., for spatially resolved skin examinations.[265,266] The implementation of other Raman modalities such as SERS,[267,268] resonance Raman spectroscopy,[269] or SRS,[270] which are mostly based on animal models, was performed. Especially for areas where imaging is an important factor, coherent Raman spectroscopy can be highly beneficial. The potential of SRS imaging of brain was demonstrated by Ji et al. using two band positions at 2845 and 2930 cm^{-1} in the CH-stretch Raman region.[271] In an in-depth study of a human glioblastoma xenograft mouse model, the authors demonstrated on *ex vivo* samples that SRS can effectively identify major histological features in the brain as well as tumor infiltration at low tumor density. Transferred to a first *in vivo* measurement during open brain surgery, they nicely demonstrated the capability of SRS to delineate cancerous areas not visible in the bright field image. Furthermore, they visualized blood vessel structures and simulated a 100 μm deep tumor resection (Figure 8B). The

https://doi.org/10.1021/acs.analchem.1c03235
Anal. Chem. 2022, 94, 86−119

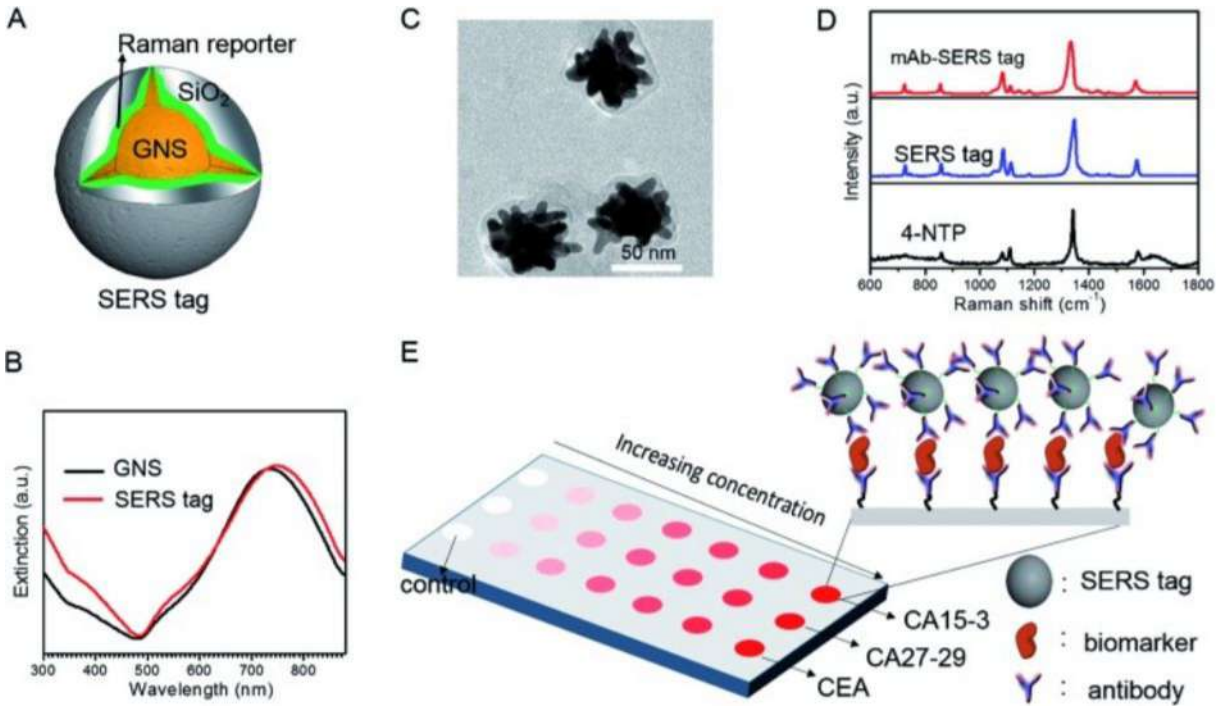

Figure 9. Multiplex SERS detection of three serological breast cancer biomarkers: (A) GNS SERS tag with integrated monoclonal antibodies and a Raman reporter molecule. (B) Extinction spectra of bare GNS and SERS tags in an aqueous solution. (C) Representative TEM image of SERS tags. (D) Raman and SERS spectra of 4-NTP, a SERS tag, and a CA15-3 mAb-modified SERS tag (SERS probe). (E) Schematic illustration of the SERS assay for the multiplex detection of biomarkers (Reproduced from Li, M.; Kang, J. W.; Sukumar, S.; Dasari, R. R.; Barman, I. *Chem. Sci.* **2015**, *6*, 3906−3914 (ref 287), with permission from The Royal Society of Chemistry).

superiority of SRS imaging over point-by-point Raman imaging lies in the fast detection of just 1 s per frame, where one spontaneous Raman spectrum alone takes between 0.5 and 2 s.[272] Therefore, spontaneous Raman imaging is not feasible *in vivo* and needs to be combined with other modalities. Jermyn et al. combined diffuse reflectance, spontaneous Raman, and intrinsic fluorescence spectroscopy for the resection of primary and metastatic brain tumors during open cranium surgery, during which all three modalities were measured within 8 s including three Raman acquisitions of each 50 ms.[273]

Although *in vivo* studies have not reached the state of *ex vivo* studies, efforts have been undertaken to investigate the feasibility of Raman spectroscopy for the clinical environment by creating close to *in vivo*-like conditions in an *ex vivo* setting, for example, to investigate the retina[274] or bone.[275]

To conclude, of high importance for Raman-based *in vivo* applications is the acceptance and easy implementation into the clinical workflow. The development of endoscopic fiber probes to detect and diagnose cancerous lesions in hollow organs is often researched. Here, spontaneous Raman spectroscopy in combination with imaging modalities, such as WLR or OCT, can highly benefit surgeons since structural and chemical information are obtained in a short time frame. For nonhollow organs or tissue sites, the faster coherent Raman scattering approach has shown promising results.

Application of Raman-Based Techniques in Liquid Biopsy. In the previous sections, the performance of Raman-based spectroscopic techniques for investigating different biological samples was summarized. Although the obtained clinical relevant information is very valuable, as it gives insight into the ongoing biological processes at the molecular level, the accessibility of these samples is low with few exceptions such as skin. Biofluids, such as urine, blood, saliva, or tears, on the other hand can be easily collected from all patients, and one can do multiple sampling. For liquid biopsies, normal Raman spectroscopy[74,276−283] or SERS[284−289] is mostly used as compared with the other Raman-based techniques. In the first case, the samples were investigated as collected or after some sample cleanup steps were performed. The obtained spectrum is a sum of the Raman active molecules present in the sample with stronger contributions from the molecules with a large scattering cross section. In the case of SERS, the molecules with high affinity toward the metallic structures used for signal enhancement will dominate the recorded spectrum. One can take advantage of this and enrich the targeted molecules on the metallic surface. For example, immunoassays where SERS is used as readout technique are suitable for such a purpose.

Most of the published studies rely on the comparison of spectroscopic data sets obtained by recording spectra on samples collected from healthy donors and patients. These data are subjected to multivariate statistical methods, and as a result, discrimination between the two data sets is achieved. Nonetheless, due to the high chemical complexity of blood or urine, the spectral differences were just in a few cases assigned to specific molecules.

For this section, one of the main criteria applied during literature research was the size of the included patient cohort. Most published studies rely on a small number of body fluid samples, up to 10, and most often, the method is not validated by an external data set. In order to transfer a technique from the lab into the clinics, first, a large number of patient samples (above 100) need to be investigated and the method needs to be tested for robustness, accuracy, and reliability. Furthermore, the costs need to be considerably reduced as compared with the standard

https://doi.org/10.1021/acs.analchem.1c03235
Anal. Chem. 2022, 94, 86−119

analytical tools, and fast turnaround times have to be achieved allowing for point-of-care testing.

Having this in mind, Jenkins et al.[276] developed a high-throughput Raman spectroscopy-based platform for serum analysis for use as a potential triage tool in primary care for symptomatic patients with suspected colorectal cancer. During development, different factors, such as the material of the supporting substrate and the sample handling procedure before and during the measurement, were optimized. In the end, a stainless steel well plate with a temperature stabilization stage for liquid serum spectral acquisition was proposed and tested on serum samples collected from 30 patients with colorectal cancer and from 30 healthy volunteers. Due to the temperature control, liquid evaporation was inhibited and the platform showed a low susceptibility to interuser variations. The recorded Raman spectra showed good reproducibility both with a 532 nm and a 785 nm laser. The main difference between the spectra of the sera of healthy and cancer individuals was found to be the two Raman bands at 1147 and 1518 cm^{-1} ascribed to carotenoids. Upon data evaluation with multivariate statistical models, a sensitivity and specificity of 83% was achieved for colorectal cancer diagnosis. A similar study was also published by Medipally et al.[277] They developed a rapid screening Raman-based platform for liquid blood plasma of prostate cancer patients. Here, a 96-well coverglass bottomed plate was used as the sample holder. Once again, the main difference between the Raman spectra of plasma samples of 10 prostate cancer patients and 10 healthy volunteers was the intensity distribution of the two Raman bands assigned to carotenoids, and a classification sensitivity of 96.5% was achieved. Now, in both studies, a good classification of healthy vs diseased patients was achieved, but the main question remains: is it possible to discriminate between samples originating from patients with different type of cancers? Unfortunately, to the best of our knowledge, no such study has been published yet with normal Raman spectroscopy. Nonetheless, Chen et al.[284] demonstrated that SERS is suitable for the identification of different stages of nasopharyngeal cancer using Au colloidal nanoparticles, 160 blood samples, and Lasso-partial least-squares-discrimination analysis. Au nanostars (GNSs) were also used to detect three serological cancer biomarkers for breast cancer.[287] The SERS chip with predefined wells patterned in quartz was functionalized with tailored SERS probes (Figure 9). These probes contained monoclonal antibodies (mAbs) specific for each of the three cancer biomarkers and the Raman reporter molecule 4-nitrothiophenol (4-NTP). The signal of this reporter transduces the presence (and concentration) of the tumor antigen at extremely low concentrations to a quantitative and reproducible spectral pattern. Furthermore, an automatic Raman scanner was also developed, and the detection of these cancer antigens was done by using just 2 μL of serum. Unfortunately, here, no clinical samples were used to assess the robustness of the system. The number of cancer diagnosis related Raman and SERS papers is high, and the interested reader is referred to further publications.[281,285,286,289]

The early and sensitive detection of a malaria infection is crucial for a positive patient outcome. Besides malaria, dengue infection is also very often encountered in tropical and subtropical regions. The two medical conditions have similar symptoms, and the correct diagnosis is very important in order to select the correct medication. A double-blinded test based on Raman spectroscopy was designed for the stratification of the two diseases based on 130 human sera, and results were confirmed by mass spectrometry (MS) for 16 individuals.[279] The principal component linear discriminant analysis (PC-LDA) resulted in a 16.7% overlap for the two diseases and a sensitivity/specificity of 95.29% for malaria vs healthy and 95.84% for dengue vs healthy controls. The Raman spectrum was dominated by contributions from amino acids, DNA, creatinine, and bilirubin. These components were also identified by MS, and their concentration showed the same trend among patient groups. Moreover, Amin et al. investigated serum samples of patients with confirmed dengue virus infection.[172] By comparing the Raman spectra of these samples to spectra from sera of healthy donors, they were able to identify six distinct bands, which only occur in the case of an infection with the dengue virus. Respectively, they also identified characteristic bands for the samples of healthy individuals. On the basis of these findings, they established a chemometric model based on principal component and linear discriminant analysis, which allowed them to distinguish between infected and noninfected samples with an accuracy of 96.5%. In a further study concerning the dengue virus, Mahmood et al. targeted blood plasma samples containing three biomarkers (nonstructural proteins (Ns1), immunoglobulin M (IgM), and immunoglobulin G (IgG)), which are associated with a corresponding infection.[173] At first, a quantitative serology test to determine the biomarker levels was performed in order to search for a correlation with features in the Raman spectra. Overall, the diagnosis solely based on the biomarkers was found to be ambiguous, and no typical pattern of biomarker concentrations or ratios could be established. However, by a multivariate analysis of the Raman spectra of dengue fever and control samples, a reliable differentiation between both groups was achieved. Ditta et al. employed blood plasma samples in order to investigate the potential of a Raman spectroscopic screening assay for hepatitis C infections.[174] They were able to identify several characteristic marker bands, which indicated the presence of the hepatitis C virus. By combining Raman spectroscopic measurements of blood plasma samples with a principal component analysis and an artificial neural network, Otange et al. were not only able to detect the presence of the human immunodeficiency virus type 1 (HIV-1) but could determine the viral load.[175] For a detailed discussion on the potential of spectroscopic methods combined with computational analysis for the exploration of virus related diseases, there is an excellent review by Santos et al. covering the period from 2006−2016.[290]

Alzheimer's disease (AD) diagnosis and differentiation from other dementia types is highly challenging. The scientific community has striven for years to find an analytical tool delivering reliable results. Several studies based on Raman and SERS have been published up to date.[74,278,280] In a recent report, Raman spectroscopy was used to diagnose AD and dementia with Lewy bodies (DLB) in blood plasma.[278] The patient cohort consisted of 11 early stage AD, 15 late stage AD, and 15 DLB patients and 15 healthy controls. Raman-based blood analysis provided an excellent diagnosis accuracy not only between diseased and nondiseased states but also between the two types of dementia. In the recorded Raman spectra, discriminatory Raman peaks were identified. For example, in the AD case, the band ascribed to amide II (~1530 cm^{-1}) showed a higher intensity as compared with the other groups and lower lipid contents were found on the basis of the Raman characteristic band at ~1432 cm^{-1}, while for DLB, phenylalanine content was higher as compared with AD. This study proves that Raman spectroscopy could be a good analytical tool. However, a

https://doi.org/10.1021/acs.analchem.1c03235
Anal. Chem. 2022, 94, 86−119

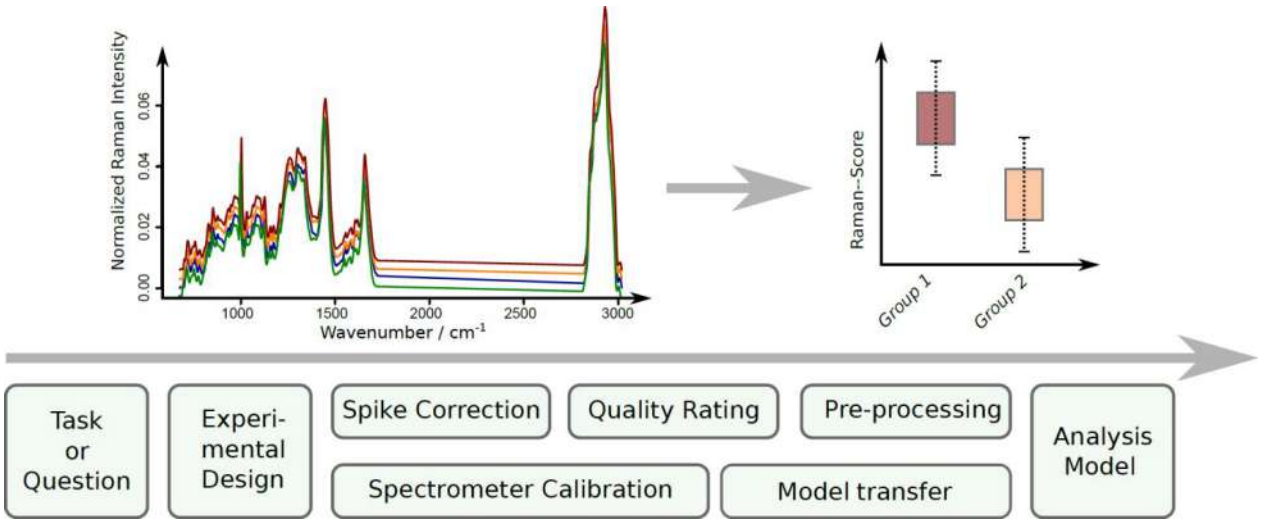

Figure 10. Data analysis pipelines for Raman spectra. This data pipeline starts with the data preprocessing of the spectra to correct for artifacts and standardize the spectral data, which is composed of a spike correction, spectrometer calibration, smoothing, background correction, normalization, and dimension reduction. Thereafter, a chemometric model, a machine learning model, or a deep learning model is used to translate the preprocessed data to meaningful information.

considerably large cohort size needs to be considered, and the model needs to be validated with independent data sets.

The root cause of relapse in hematological malignancies is the poor detection of malignant cells that remain in the human body after chemotherapy or bone marrow transplantation. This medical condition is also referred to as the minimal residual disease (MRD). In a recent study, a SERS assay was developed for the simultaneous detection of two MRD biomarkers: CD19 and CD20. Namely, the detection principle relies on the aqueous phase sandwich-type immunoassay realized in the presence of the target cells. The authors used magnetic beads modified with anti-CD45 protein to capture leukocytes out of the blood sample, and this was followed by the interaction of the as-captured cells with anti-CD19 or anti-CD20-functionalized SERS probes. The SERS probes were equipped with Raman marker molecules that served as optical signal sources. The SERS assay was used to analyze peripheral blood samples of B cell hematological malignancy patients with positive as well as negative MRD diagnosis. The gold standard for MRD detection is flow cytometry (FCM). 56 negative MRD clinical samples were measured by the SERS assay, and it was found that 5 of these blood samples produced significant SERS signals. This might indicate that this assay is more sensitive compared to FCM; however, the authors did not use any other analytical method to confirm these results. Finally, in order to test the long-term performance of these sensors, a follow-up study for 13 patients of B cell hematological malignancy was conducted and the results were in a good agreement with the FCM results.

In conclusion, both Raman and SERS spectroscopy are suitable for performing liquid biopsies. With the advent of portable Raman setups and the careful design of measurement protocols, Raman could be used in the clinics for cancer diagnosis, malaria detection, or AD identification.

DATA ANALYSIS CONCEPTS IN RAMAN-BASED METHODS IN BIOPHOTONICS

As Raman related spectra, like spontaneous Raman spectra, SERS spectra, and Raman related image data, like CARS images and SRS images, are typically measured in an unlabeled manner, the generated data needs to be translated into meaningful information in the application context. Such information might be diagnostic relevant information like a Raman marker band or a generated fingerprint in the Raman spectra, which correlate with some external variable. In order to extract such application related information, data analysis pipelines are utilized, which aim at correcting the data from artifacts, standardizing the data, and finally using chemometric or machine learning models to translate the preprocessed spectroscopic data into meaningful information. The review of all publications on such data analysis pipelines goes far beyond the scope of this section, but we want to highlight important research for data analysis pipelines in general. Thereafter, we will present publications that investigate the data analysis pipelines for Raman related spectra and images.

The first generic issue of data analysis pipelines is the sample size planning (SSP), which tries to estimate how many samples need to be measured for a reliable analysis. In contrast to univariate data, SSP for images and spectra is not a standard procedure. Recently, SSP methods for spectra based on the learning curve were reported using simulated data[291] and real measured Raman spectra.[292] Another generic part of the data analysis pipelines is the model visualization. This issue largely depends on the used chemometric or machine learning method, which should be visualized. For deep learning methods, Schuhmacher et al. developed a visualization method[293] by inferring a sematic segmentation from image/scan labels, which they demonstrated for IR spectra. Another approach presented in ref 294 aims to approximate the polynomial of the nonlinear classifier and subsequently visualize the parts of the polynomial approximation.[294] Maier et al. developed another approach where they replaced parts of the deep learning model with physical building blocks, which reduced the number of model parameters and the error rate.[295]

Besides these generic aspects of the data analysis pipelines, there are data specific issues of these data pipelines. Therefore, we will describe data analysis pipelines for Raman spectra and Raman related images separately, and we start with the data analysis pipelines for Raman spectra (see Figure 10). This data pipeline starts with the data preprocessing of the spectra to correct for artifacts and standardize the spectral data. Typically, a spike correction, a spectrometer calibration, a smoothing, a

https://doi.org/10.1021/acs.analchem.1c03235
Anal. Chem. 2022, 94, 86−119

background correction, normalization, and dimension reduction are applied. There are too many publications that demonstrate new algorithms for specific tasks, like spike correction, to be included in this section. Therefore, we only refer to comparisons of preprocessing approaches and reviews.

Two reviews of preprocessing techniques were conducted by Gautam et al.[296] and Byrne et al.,[297] which give an appropriate overview. Recent comparisons of Raman spectroscopic preprocessing techniques were conducted by Olmos et al.[298] and Schulze et al.[299] While Olmos et al. especially researched the influence of the normalization step on the outcome of PLS models, Schulze et al. introduced a fully automated method to establish data preprocessing. They developed a figures-of-merit that quantified the preprocessing quality. A similar merit of a quality-based approach was carried out by Guo et al.[300] to determine the background correction quality.

Besides preprocessing, which is performed to remove sample-dependent artifacts like a fluorescence background, device specific artifacts also need to be corrected. To do so, a wavenumber calibration, a wavelength calibration, and an intensity calibration are performed,[301] but it could be shown that these approaches do not yield setup independent Raman spectra.[302] This setup dependence of the Raman spectra was recently studied in a larger European ring trial.[303] In that regard, an improvement of setup calibration procedures was investigated by Bocklitz et al.[304] They could show that an improvement of the calibration quality could be achieved by incorporating the measured excitation wavelength into the calibration procedure.

Besides the preprocessing techniques, classification and regression methods are also the subject of investigations and comparisons. In ref 305, a support vector machine (SVM), linear discriminant analysis (LDA), and an artificial neural network (ANN) were investigated, and it turned out that ANN is superior for the investigated task. Nevertheless, this result is probably data set dependent, so there is no analysis method that is always superior. Pomrehn et al. compared different classifiers for Raman spectra, IR spectra, and their combination.[306] They could show that the combination of spectra yields the best results. Another recently addressed issue in Raman spectroscopy is the so-called model transfer, where a model (or the corresponding data) is changed so that the model performance on the data differing from the training data is improved. Guo et al. developed multiple possibilities to solve this model transfer issue including regularization-based approaches[307] and extended multiplicative signal correction (EMSC)-based approaches.[308]

Until now, the standard data analysis pipeline for Raman spectra was followed. In recent years, deep learning methods have been utilized to replace the classical machine learning/chemometric model at the end of the standard data analysis pipeline or to replace the whole data analysis pipeline. The results of these studies are that some researchers found that deep learning especially CNNs can replace the whole data analysis pipeline including the preprocessing step and other researchers found that preprocessing is important as the deep learning benefits from its application. For example, Acquarelli et al.[309] used a shallow CNN, which could outperform standard classification algorithms used in chemometrics even when applied to nonpreprocessed and also preprocessed test data. Zhang et al. also introduced a CNN-based model "Deep-Spectra"[310] and compared it to three other models. They also investigated the preprocessing dependency of the models and found that Deep-Spectra outperforms the other models on all data sets in most of the compared scenarios. Fukuhara et al.[311] used a CNN and could highlight wavenumber regions, which were important for the model. The approach was similar to saliency maps utilized in CNN-based image classification. They could show that parts of the model recognized peaks while other parts were performing data processing steps like baseline issues. Liu et al. also presented a CNN as a unified data analysis method for Raman spectra.[312] They used the RUFFT database to evaluate their method, showed that their method does not need spectral preprocessing, and achieved state-of-the-art performance. Nevertheless, the RUFTT database is a mineral database, where the device dependency overlaps with the group variance, which needs further investigation. Kirchberger-Tolstik et al.[313] constructed a 1D CNN for the diagnostics of inflammatory bowel disease (IBD) and the prediction of the Mayo score using tissue Raman spectra as the basis. Ho et al.[314] used deep learning to combine bacterial detection, identification, and antibiotic susceptibility testing. They tested 30 of the most common bacterial pathogens and achieved accuracies of around 99%, and they could also distinguish between methicillin-resistant and methicillin-susceptible isolates of *Staphylococcus aureus* (MRSA and MSSA). The authors also could discriminate isogenic MRSA and MSSA that are genetically identical apart from deletion of the mecA resistance gene. These results are impressive, and it would be nice to see which part in the Raman spectra corresponds to a single gene.

A second often utilized experimental setup for Raman-based measurements is the imaging approach, in which only a few bands are measured, but these bands are measured over a larger spatial area. The resulting Raman related images are also analyzed using data analysis pipelines, and its specific parts together with related publications will be described in the following. There are hardly any systematic investigations about these data pipelines in general. As an exception, Chernavskaia et al. researched a new uneven illumination correction (UI)/flat field correction method[315] for CARS images and other images related to nonlinear processes and compared this UI method to other UI approaches. Orringer et al. utilized SRS images of brain tissue in combination with deep learning to generate a histopathological tool.[85] Yarbakht et al.[316] in contrast utilized CARS, SHG, and TPEF images of liver tissue to characterize a septic liver injury using classical machine learning. Rodner et al. utilized similar images but also used deep learning techniques to generate a semantic segmentation of head and neck tissue sections.[317] Ji et al.[84] used classical machine learning of SRS images to identify human brain tumor infiltration by integrating SRS image attributes such as hypercellularity, axonal density, and protein/lipid ratio. The same authors showed that multicolor SRS[86] can detect amyloid plaques in brain tissue from a transgenic mouse model of AD. They utilized the spectral shift of the amide I band of β-sheets as discrimination criteria. Besides the direct extraction of diagnostic information, the stain modeling became popular in recent years. For nonlinear Raman techniques, this was done by Bocklitz et al. using classical machine learning of CARS, TPEF, and SHG images,[249] while Orringer et al.[85] utilized SRS in combination with deep learning techniques. Both models could generate artificial HE stained sections to link Raman related techniques to standard histopathological workflows.

These data pipelines are not fully researched yet, which is why there are open issues regarding these data analysis pipelines that need to be investigated. The first open issue is the sample size

https://doi.org/10.1021/acs.analchem.1c03235
Anal. Chem. 2022, 94, 86−119

planning for deep learning methods, which is not developed yet. Especially, the interplay between the number of learnable (model) parameters, number of groups to be differentiated, and the covariance structure of the data needs to be investigated. Another important point to be researched is the visualization of nonlinear classification and regression techniques, like deep learning methods. This is important to explain the outcome of these deep learning methods with respect to the data forming the basis of the model. Besides the visualization, also the evaluation, e.g., the estimation of the generalization performance, for small sample size scenarios is important and is an open issue. For classical machine learning, a cross validation[318] can be used, which is due to the numerical complexity not possible for deep learning. Another point worth investigating is the device dependency of the outcome of chemometric and deep learning-based analysis models, which leads to the model transfer issue discussed earlier. For deep learning procedures, this model transfer is an open issue.

CONCLUSION AND OUTLOOK

Raman spectroscopy is a powerful technique in bioanalytics as it provides molecular specificity for the identification and classification of biomolecules. Moreover, the technique allows for *in situ* measurements and quantification. Raman spectroscopy is known as a noninvasive technique, and only minimal sample preparation is required. Employing portable systems, Raman spectroscopy can be directly applied at the point-of-care. If additional signal enhancing processes are included, low detection limits down to the single molecule level can be achieved with short acquisition times ($\ll$1 s) per spectrum.

In the case of the detection of low molecular weight substances, SERS can be applied to reach trace sensitivity. When the measurements are performed in real matrices with high complexity, contributions from matrix components can interfere with the overall fingerprint spectrum of the target analyte. For molecules with a high affinity to the metallic surface, the signal originating from the background could be suppressed. For resonant molecules, the resonance Raman spectrum is dominated by contributions from the vibrational modes associated with the electronic transition, allowing the detection of target molecules in trace concentrations even in complex matrices such as cells and tissues.

In the case of nucleic acids and proteins, the structural or conformational changes can be monitored by Raman spectroscopy, allowing, for example, quality control in the synthesis of oligonucleotides. However, in SERS-based detection schemes, variations in the orientation of the macromolecules on the metallic surface can lead to different spectral profiles. Consequently, the need for reproducible interactions between the target and sensing surface becomes very important. As an example, SERS can be applied to observe hybridization events, quantification of modifications in amino acids, or the native state of proteins. A high potential for clinical practice in near future is demonstrated by using stable SERS labels in lateral flow assays for the detection of proteins in human body fluid samples. Using TERS, conformational changes during the formation of amyloid fibrils can be analyzed or nucleobases can be distinguished in single nucleic acid strands on the submolecular level. Finally, resonance Raman spectroscopy can be successfully employed to identify structural changes due to the complexation of hemoglobin with O_2 or CO_2. In malaria research studies, it was demonstrated that hemozoin in cells can be identified and the redox state of metalloproteins or metalloenzymes can be estimated.

When analyzing individual viruses, Raman spectroscopy is limited by the optical resolution limit. Therefore, SERS approaches are developed to enrich virus particles on metallic nanostructured surfaces to enhance the Raman fingerprint by several orders of magnitude. The spectroscopic characterization of individual virus particles becomes feasible by the application of TERS enabling the investigation with nanometer scale lateral resolution. Raman microscopic approaches have been developed for the analysis of single bacterial cells, and Raman spectral fingerprints are sensitive to variations in their cultivation or environment. Raman spectroscopy is applied to set up databases for the rapid and reliable identification of bacteria in clinical and bioanalytical detection schemes. The recent developments in the field of eukaryotic cells reveal that Raman spectroscopy is currently in a transition state, where the method finally becomes more applicable and operational not only by the experienced user but also by the everyday biomolecular researcher.

For the fast, specific, and sensitive screening of tissue samples, coherent Raman scattering imaging will soon be established in clinical routines. Since CRS is compatible with other nonlinear imaging methods, a wide range of information about the structure and composition of the native tissue can be obtained. In particular, spectrally resolved CRS imaging with fast, spectrally switchable light sources is an ideal tool for the label-free monitoring of any molecular markers of interest and even for the colocalization of a combination of molecular markers in real time. In combination with vibrational labeling, even the spatial distribution of molecular markers of low concentration can be analyzed, rendering CRS imaging the most versatile method for clinical use, offering label-free imaging with diffraction-limited spatial resolution at a video rate.

Moreover, the acceptance and easy implementation of Raman-based *in vivo* detection schemes are of high importance to incorporate the techniques into the clinical workflow. In the case of cancerous lesions in hollow organs, often, endoscopic fiber probes are developed for detection and diagnosis. Here, surgeons might benefit from spontaneous Raman spectroscopy in combination with imaging modalities, such as WLR or OCT, as structural and chemical information are obtained in a short time frame. For nonhollow organs or tissue sites, CRS approaches have shown promising results. Finally, Raman and SERS spectroscopy are applied to perform liquid biopsies. In the future, the application of portable Raman systems and standard operation procedures provides access for Raman-based methods in clinics for, i.e., cancer diagnosis, malaria detection, or AD identification.

Besides the improvement of Raman-based measurement techniques and the combination of these measurements with other data sources, the data analysis had a large boost in recent years. This boost can be assigned to machine learning techniques, namely, deep learning, which is nowadays applied to Raman data. Since these DL methods can only be trained with the large data sets, the compatibility between setups, laboratories, and conditions is becoming more important to combine different data sources. This compatibility was studied recently, which marks a starting point to combine data from different devices. Besides this study, methods were developed to deal with the model transfers from one device to another, and studies on the validation methods were performed. Further research is needed in this direction to create a unified understanding of model validation and facilitate the use of

https://doi.org/10.1021/acs.analchem.1c03235
Anal. Chem. 2022, 94, 86−119

Raman-based models for real world tasks like clinical diagnostics.

AUTHOR INFORMATION

Corresponding Author

Jürgen Popp − *Leibniz-Institute of Photonic Technology, Member of the Leibniz Research Alliance − Leibniz Health Technologies, 07745 Jena, Germany; Institute of Physical Chemistry and Abbe Center of Photonics, Friedrich Schiller University, 07743 Jena, Germany; InfectoGnostics Research Campus Jena, Center of Applied Research, 07743 Jena, Germany;* orcid.org/0000-0003-4257-593X; Email: juergen.popp@uni-jena.de

Authors

Dana Cialla-May − *Leibniz-Institute of Photonic Technology, Member of the Leibniz Research Alliance − Leibniz Health Technologies, 07745 Jena, Germany; Institute of Physical Chemistry and Abbe Center of Photonics, Friedrich Schiller University, 07743 Jena, Germany; InfectoGnostics Research Campus Jena, Center of Applied Research, 07743 Jena, Germany*

Christoph Krafft − *Leibniz-Institute of Photonic Technology, Member of the Leibniz Research Alliance − Leibniz Health Technologies, 07745 Jena, Germany;* orcid.org/0000-0003-1049-0560

Petra Rösch − *Institute of Physical Chemistry and Abbe Center of Photonics, Friedrich Schiller University, 07743 Jena, Germany;* orcid.org/0000-0001-6179-3719

Tanja Deckert-Gaudig − *Leibniz-Institute of Photonic Technology, Member of the Leibniz Research Alliance − Leibniz Health Technologies, 07745 Jena, Germany; Institute of Physical Chemistry and Abbe Center of Photonics, Friedrich Schiller University, 07743 Jena, Germany*

Torsten Frosch − *Leibniz-Institute of Photonic Technology, Member of the Leibniz Research Alliance − Leibniz Health Technologies, 07745 Jena, Germany; Institute of Physical Chemistry and Abbe Center of Photonics, Friedrich Schiller University, 07743 Jena, Germany*

Izabella J. Jahn − *Leibniz-Institute of Photonic Technology, Member of the Leibniz Research Alliance − Leibniz Health Technologies, 07745 Jena, Germany; Institute of Physical Chemistry and Abbe Center of Photonics, Friedrich Schiller University, 07743 Jena, Germany;* orcid.org/0000-0002-1186-0925

Susanne Pahlow − *Leibniz-Institute of Photonic Technology, Member of the Leibniz Research Alliance − Leibniz Health Technologies, 07745 Jena, Germany; Institute of Physical Chemistry and Abbe Center of Photonics, Friedrich Schiller University, 07743 Jena, Germany; InfectoGnostics Research Campus Jena, Center of Applied Research, 07743 Jena, Germany*

Clara Stiebing − *Leibniz-Institute of Photonic Technology, Member of the Leibniz Research Alliance − Leibniz Health Technologies, 07745 Jena, Germany*

Tobias Meyer-Zedler − *Leibniz-Institute of Photonic Technology, Member of the Leibniz Research Alliance − Leibniz Health Technologies, 07745 Jena, Germany; Institute of Physical Chemistry and Abbe Center of Photonics, Friedrich Schiller University, 07743 Jena, Germany*

Thomas Bocklitz − *Leibniz-Institute of Photonic Technology, Member of the Leibniz Research Alliance − Leibniz Health Technologies, 07745 Jena, Germany; Institute of Physical Chemistry and Abbe Center of Photonics, Friedrich Schiller University, 07743 Jena, Germany;* orcid.org/0000-0003-2778-6624

Iwan Schie − *Leibniz-Institute of Photonic Technology, Member of the Leibniz Research Alliance − Leibniz Health Technologies, 07745 Jena, Germany; Ernst-Abbe-Hochschule Jena, University of Applied Sciences, Department of Biomedical Engineering and Biotechnology, 07745 Jena, Germany;* orcid.org/0000-0003-0336-3168

Volker Deckert − *Leibniz-Institute of Photonic Technology, Member of the Leibniz Research Alliance − Leibniz Health Technologies, 07745 Jena, Germany; Institute of Physical Chemistry and Abbe Center of Photonics, Friedrich Schiller University, 07743 Jena, Germany;* orcid.org/0000-0002-0173-7974

Complete contact information is available at: https://pubs.acs.org/10.1021/acs.analchem.1c03235

Notes

The authors declare no competing financial interest.

Biographies

Dana Cialla-May studied chemistry at the Friedrich Schiller University of Jena (Germany) where she received her Diploma and Ph.D. degrees in 2006 and 2010, respectively, under the supervision of Prof. Jürgen Popp. Since 2011, she has been a research group leader within the department of Spectroscopy and Imaging at the Leibniz Institute of Photonic Technology in Jena (Germany). Her research interest is in the field of surface-enhanced Raman spectroscopy and its application in bioanalytical detection schemes, e.g., the detection of drugs and metabolites in complex biological matrices.

Christoph Krafft studied physics at the University Oldenburg (Germany) and received his Ph.D. in biophysics from the Humboldt University Berlin in 1998 (Germany). He went to the University of Missouri Kansas City (USA) and University Trieste (Italy) for postgraduate studies. He led the research group "Molecular Endo-spectroscopy" at the Dresden University of Technology (Germany) where he finished his habilitation. Since 2008, he has led a research group at Leibniz IPHT in Jena. His research is focused on Raman- and infrared-based studies of biomolecules, tissues, and cells for bioanalytical and medical diagnostic applications.

Petra Rösch received her Ph.D. in chemistry from the University of Würzburg in 2002. She is a research associate for Jürgen Popp. Her research interests are focused on the investigation of all kinds of biological, medical, and pharmaceutical relevant problems with various vibrational spectroscopic methods. Her main focus is on the characterization and identification of blood samples, tissues, and microorganisms with Raman microscopy and UV-resonance Raman spectroscopy.

Tanja Deckert-Gaudig studied chemistry at the University of Stuttgart, Würzburg, and the University College of Swansea (Wales). During her Ph.D. thesis in organic chemistry in the group of Prof. S. Hünig, she was awarded a scholarship to spend six months at the University of Tokyo (Japan), and she received her degree in 1997. After her parental leave, she started working in the field of plasmon-enhanced Raman spectroscopy and scanning probe microscopy at the Dresden University of Technology in 2002. She continued her research at the Leibniz Institute of Analytical Sciences (ISAS) in Dortmund and moved to Jena in 2009. Since then, she has worked at the Leibniz Institute of Photonic Technology (IPHT). Her research includes the nanoscopic structural characterization of organic materials (core−shell particles, self-

assembled monolayers) and biological surfaces (amyloid fibrils, viruses) using tip-enhanced Raman scattering.

Torsten Frosch is a Full Professor in the Biophotonics−Biomedical Engineering department at the Technical University Darmstadt and head of the Fiber Spectroscopic Sensing Group at the Leibniz Institute of Photonic Technology Jena. He studied physics and received the award of the Friedrich Schiller University Jena and the STIFT award for his Ph.D. in physical chemistry. After postdoctoral work at Monash University in Melbourne and Imperial College in London, he started to establish a junior group at the IPHT. His habilitation work regarding enhanced Raman spectroscopy of complex biogenic multigas compositions and fiber enhanced Raman spectroscopy of pharmaceuticals was recognized with the Bunsen-Kirchhoff award (DAAS/GDCh). His current research activities include the development and application of flexible and sensitive Raman spectroscopic techniques for interdisciplinary biomedical, pharmaceutical, and environmental research.

Izabella J. Jahn studied physics at the Babes-Bolyai University in Cluj-Napoca, Romania. In 2012, she joined the group of Prof. Popp, and she received her Ph.D. in 2016. During this time, she focused on assessing the potential and limitation of lab-on-a-chip SERS devices to determine and quantify antibiotics in human urine samples with the aim of therapeutic drug monitoring. Currently, she is a postdoctoral researcher at the Leibniz Institute of Photonic Technology, Jena, and focuses on the development and assessment of Raman spectroscopy platforms for biosensor applications.

Susanne Pahlow obtained her diploma in chemistry in 2010 at the Friedrich Schiller University in Jena. Afterwards, she joined the biophotonics group of Prof. Dr. Jürgen Popp at the Leibniz Institute of Photonic Technologies (IPHT) and worked in the field of Raman microspectroscopy, specializing in the identification of bacteria. In 2016, she defended her Ph.D. thesis with the topic "Innovative Sample Preparation Strategies and Detection Methods for Microorganisms", and she currently works as a postdoctoral researcher at the IPHT. Her main research interests are establishing Raman compatible sample preparation strategies and investigating new capture probes for microorganisms and chemical surface modification techniques.

Clara Stiebing studied physics at the Goethe University, Frankfurt/Main, Germany, during which she spent a semester at the Stockholm University, Sweden. She received her Ph.D. from the Friedrich Schiller University Jena, Germany, in 2017. She currently works as a postdoctoral researcher at the Leibniz Institute of Photonic Technology in Jena within the spectroscopy and imaging research department. Her interests include the research and development of Raman spectroscopic techniques.

Tobias Meyer-Zedler studied physics at the Friedrich Schiller University of Jena and at Lancaster University, UK, focusing on optics. He graduated in 2006 and received his Ph.D. in the research group of Prof. Popp working on CARS microscopy in 2013. Since then, he has been working at the Leibniz Institute of Photonic Technology on biomedical applications of multimodal nonlinear imaging. His main expertise is the use of fiber lasers for realizing compact microscopes and endoscopes for CRS and investigating other nonlinear imaging methods as well as sample manipulation techniques. Currently, he is heading the research group for molecular imaging at the Leibniz Institute of Photonic Technology in Jena.

Thomas Bocklitz studied physics at the University of Jena, and he received his Ph.D. in physical chemistry/chemometrics from the same university in 2011. In 2013, he became the head of a junior research group "Statistical Modelling and Image Analysis" at the University of Jena. Since 2019, he has been head of the research department "Photonic data science" at the Leibniz IPHT. His main research area is closely connected with the photonic data life cycle, which contains machine learning and chemometrics-based modeling of photonic data. He has published more than 110 publications in peer reviewed journals and given more than 50 invited talks at conferences. His work has been granted prestigious awards such as the Kaiser-Friedrich-Forschungspreis in 2018 and the Bruce Kowalski in 2015.

Iwan Schie received his Ph.D. in biomedical engineering from the University of California, Davis. Since 2014, he has been a postdoctoral researcher at the Leibniz-IPHT, and he established the group for "Multimodal Instrumentation" in 2017, focusing on high-throughput RS for cells, multimodal optical systems for tissue characterization, development of fiber probes, and high TRL-level instrumentation for medical *in vivo* applications. In 2019, he became a professor in the Biomedical Engineering department at the University of Applied Science, Jena.

Volker Deckert, currently a research fellow at the IQSE at Texas A&M, is a Full Professor in the Physical Chemistry department at the Friedrich Schiller University in Jena and jointly heads the Nanoscopy department at the Leibniz Institute of Photonic Technology also in Jena. He obtained his Diploma and his Ph.D. from the University of Würzburg (Germany) working in the field of Raman spectroscopy. After a postdoc at the University of Tokyo and his habilitation at the ETH Zurich, he worked at the TU Dresden and the ISAS in Dortmund before starting in Jena (2009). His research focuses on near-field optical spectroscopy, namely, in tip-enhanced Raman techniques, to investigate the limits of optical and spectroscopic resolution.

Jürgen Popp holds a chair in the Physical Chemistry department at the Friedrich-Schiller University Jena and is also the scientific director of the Leibniz Institute of Photonic Technology, Jena. His research interests are mainly concerned with biophotonics. In particular, his expertise in the development and application of innovative Raman techniques for biomedical diagnosis should be emphasized. In 2012, he received an honorary doctoral degree from Babeş-Bolyai University in Cluj-Napoca, Romania, and he is, among others, the recipient of the prestigious 2016 Pittsburgh Spectroscopy Award.

■ ACKNOWLEDGMENTS

Financial support of the EU, the "Thüringer Ministerium für Wirtschaft, Wissenschaft und Digitale Gesellschaft", the "Thüringer Aufbaubank", the Federal Ministry of Education and Research, Germany (BMBF), the German Science Foundation, the Fonds der Chemischen Industrie, and the Carl-Zeiss Foundation are greatly acknowledged.

■ REFERENCES

(1) Long, D. A. *Int. Rev. Phys. Chem.* **1988**, *7*, 317−349.
(2) Kano, H.; Segawa, H.; Leproux, P.; Couderc, V. *Opt. Rev.* **2014**, *21*, 752−761.
(3) Clark, R. J. H.; Hester, R. E. *Advances in Infrared and Raman Spectroscopy*; Heyden, 1975.
(4) Lord, R. C.; Yu, N.-t. *J. Mol. Biol.* **1970**, *50*, 509−524.
(5) Schmitt, M.; Popp, J. *J. Raman Spectrosc.* **2006**, *37*, 20−28.
(6) Auner, G. W.; Koya, S. K.; Huang, C.; Broadbent, B.; Trexler, M.; Auner, Z.; Elias, A.; Mehne, K. C.; Brusatori, M. A. *Cancer Metastasis Rev.* **2018**, *37*, 691−717.
(7) Chaichi, A.; Prasad, A.; Gartia, M. R. *Biosensors* **2018**, *8*, 107.
(8) Devitt, G.; Howard, K.; Mudher, A.; Mahajan, S. *ACS Chem. Neurosci.* **2018**, *9*, 404−420.
(9) Perez-Guaita, D.; Marzec, K. M.; Hudson, A.; Evans, C.; Chernenko, T.; Matthäus, C.; Miljkovic, M.; Diem, M.; Heraud, P.; Richards, J. S.; Andrew, D.; Anderson, D. A.; Doerig, C.; Garcia-Bustos, J.; McNaughton, D.; Wood, B. R. *Chem. Rev.* **2018**, *118*, 5330−5358.

https://doi.org/10.1021/acs.analchem.1c03235
Anal. Chem. 2022, 94, 86−119

(10) Leal, L. B.; Nogueira, M. S.; Canevari, R. A.; Carvalho, L. F. C. S. *Photodiagn. Photodyn. Ther.* **2018**, *24*, 237−244.
(11) Chisanga, M.; Muhamadali, H.; Ellis, D. I.; Goodacre, R. *Appl. Spectrosc.* **2018**, *72*, 987−1000.
(12) Ermakov, I.; Gellermann, W. *Arch. Biochem. Biophys.* **2015**, *572*, 101−111.
(13) Hollon, T. C.; Pandian, B.; Adapa, A. R.; Urias, E.; Save, A. V.; Khalsa, S. S. S.; Eichberg, D. G.; D'Amico, R. S.; Farooq, Z. U.; Lewis, S.; Petridis, P. D.; Marie, T.; Shah, A. H.; Garton, H. J. L.; Maher, C. O.; Heth, J. A.; McKean, E. L.; Sullivan, S. E.; Hervey-Jumper, S. L.; Patil, P. G.; Thompson, B. G.; Sagher, O.; McKhann, G. M.; Komotar, R. J.; Ivan, M. E.; Snuderl, M.; Otten, M. L.; Johnson, T. D.; Sisti, M. B.; Bruce, J. N.; Muraszko, K. M.; Trautman, J.; Freudiger, C. W.; Canoll, P.; Lee, H.; Camelo-Piragua, S.; Orringer, D. A. *Nat. Med.* **2020**, *26*, 52−58.
(14) Ralbovsky, N. M.; Lednev, I. K. *Spectrochim. Acta, Part A* **2019**, *219*, 463−487.
(15) Everall, N. J. *Analyst* **2010**, *135*, 2512−2522.
(16) Smith, G. P. S.; McGoverin, C. M.; Fraser, S. J.; Gordon, K. C. *Adv. Drug Delivery Rev.* **2015**, *89*, 21−41.
(17) Cordero, E.; Latka, I.; Matthäus, C.; Schie, I.; Popp, J. *J. Biomed. Opt.* **2018**, *23*, No. 071210.
(18) Shim, M. G.; Wilson, B. C.; Marple, E.; Wach, M. *Appl. Spectrosc.* **1999**, *53*, 619−627.
(19) Wang, J.; Bergholt, M. S.; Zheng, W.; Huang, Z. *Opt. Lett.* **2013**, *38*, 2321−2323.
(20) Katagiri, T.; Yamamoto, Y. S.; Ozaki, Y.; Matsuura, Y.; Sato, H. *Appl. Spectrosc.* **2009**, *63*, 103−107.
(21) Mo, J.; Zheng, W.; Huang, Z. *Biomed. Opt. Express* **2010**, *1*, 17−30.
(22) Day, J. C. C.; Bennett, R.; Smith, B.; Kendall, C.; Hutchings, J.; Meaden, G. M.; Born, C.; Yu, S.; Stone, N. *Phys. Med. Biol.* **2009**, *54*, 7077−7087.
(23) Agenant, M.; Grimbergen, M.; Draga, R.; Marple, E.; Bosch, R.; van Swol, C. *Biomed. Opt. Express* **2014**, *5*, 1203−1216.
(24) Yang, W.; Mondol, A. S.; Stiebing, C.; Marcu, L.; Popp, J.; Schie, I. W. *J. Biophotonics* **2019**, *12*, No. e201800447.
(25) Dochow, S.; Fatakdawala, H.; Phipps, J. E.; Ma, D.; Bocklitz, T.; Schmitt, M.; Bishop, J. W.; Margulies, K. B.; Marcu, L.; Popp, J. J. *Biophotonics* **2016**, *9*, 958−966.
(26) Huang, Z.; Bergholt, M. S.; Zheng, W.; Lin, K.; Ho, K. Y.; Teh, M.; Yeoh, K. G. *J. Biomed. Opt.* **2010**, *15*, No. 037017.
(27) Bergholt, M. S.; Zheng, W.; Lin, K.; Ho, K. Y.; Teh, M.; Yeoh, K. G.; So, J. B. Y.; Huang, Z. *Technol. Cancer Res. Treat.* **2011**, *10*, 103−112.
(28) Schmälzlin, E.; Moralejo, B.; Bodenmüller, D.; Darvin, M. E.; Thiede, G.; Roth, M. M. J. *J. Sens. Sens. Syst.* **2016**, *5*, 261−271.
(29) Konorov, S. O.; Addison, C. J.; Schulze, R. F.; Turner, R. F.; Blades, M. W. *Opt. Lett.* **2006**, *31*, 1911−1913.
(30) Ghenuche, P.; Rammler, S.; Joly, N. Y.; Scharrer, M.; Frosz, M.; Wenger, J.; Russell, P. S. J.; Rigneault, H. *Opt. Lett.* **2012**, *37*, 4371−4373.
(31) Russell, P. *Science* **2003**, *299*, 358−362.
(32) Knebl, A.; Yan, D.; Popp, J.; Frosch, T. *TrAC, Trends Anal. Chem.* **2018**, *103*, 230−238.
(33) Frosch, T.; Yan, D.; Popp, J. *Anal. Chem.* **2013**, *85*, 6264−6271.
(34) Bogozi, T.; Popp, J.; Frosch, T. *Bioanalysis* **2015**, *7*, 281−284.
(35) Hanf, S.; Keiner, R.; Yan, D.; Popp, J.; Frosch, T. *Anal. Chem.* **2014**, *86*, 5278−5285.
(36) Hanf, S.; Bogozi, T.; Keiner, R.; Frosch, T.; Popp, J. *Anal. Chem.* **2015**, *87*, 982−988.
(37) Knebl, A.; Domes, R.; Yan, D.; Popp, J.; Trumbore, S.; Frosch, T. *Anal. Chem.* **2019**, *91*, 7562.
(38) Jochum, T.; Rahal, L.; Suckert, R. J.; Popp, J.; Frosch, T. *Analyst* **2016**, *141*, 2023−2029.
(39) Liu, Y.; Wang, J.; Li, Z.; Wang, J.; Ning, Y.; Liu, T.; Grattan, K. T. V. *IEEE Sens. J.* **2019**, *19*, 560−566.
(40) Khetani, A.; Momenpour, A.; Alarcon, E. I.; Anis, H. *Biomed. Opt. Express* **2015**, *6*, 4599−4609.
(41) Yan, D.; Popp, J.; Pletz, M. W.; Frosch, T. *Anal. Methods* **2018**, *10*, 586−592.
(42) Khetani, A.; Tiwari, V. S.; Momenpour, A.; Anis, H. Monitoring of Adenosine within Hollow Core Photonic Crystal Fiber by Surface Enhanced Raman Scattering (SERS). In *IEEE Nanotechnology (IEEE-NANO) 2011 Conference*, 2011; pp 973−977.
(43) Yan, D.; Domes, C.; Domes, R.; Frosch, T.; Popp, J.; Pletz, M. W.; Frosch, T. *Analyst* **2016**, *141*, 6104−6115.
(44) Eravuchira, P. J.; Banchelli, M.; D'Andrea, C.; Angelis, M. D.; Matteini, P.; Gannot, I. Fiber-enhanced Raman spectroscopy as a tool for an early detection of Alzheimer's disease biomarkers. In *Proc. SPIE 10872, Optical Fibers and Sensors for Medical Diagnostics and Treatment Applications XIX*; 2019; 10872; DOI: 10.1117/12.2516545.
(45) Yan, D.; Popp, J.; Pletz, M. W.; Frosch, T. *ACS Photonics* **2017**, *4*, 138−145.
(46) Khetani, A.; Tiwari, V. S.; Harb, A.; Anis, H. *Opt. Express* **2011**, *19*, 15244−15254.
(47) Yan, D.; Frosch, T.; Kobelke, J.; Bierlich, J.; Popp, J.; Pletz, M. W.; Frosch, T. *Anal. Chem.* **2018**, *90*, 13243−13248.
(48) Sieburg, A.; Knebl, A.; Jacob, J. M.; Frosch, T. *Anal. Bioanal. Chem.* **2019**, *411*, 7399−7408.
(49) Knebl, A.; Domes, R.; Wolf, S.; Domes, C.; Popp, J.; Frosch, T. *Anal. Chem.* **2020**, *92*, 12564−12571.
(50) Yan, D.; Popp, J.; Frosch, T. *Anal. Chem.* **2017**, *89*, 12269−12275.
(51) Wolf, S.; Frosch, T.; Popp, J.; Pletz, M. W.; Frosch, T. *Molecules* **2019**, *24*, 4512.
(52) Filho, I.; Nguyen, N.; Jivani, R.; Terner, J.; Romfh, P.; Vakhshoori, D.; Ward, K. *J. Surg. Res.* **2016**, *201*, 425−431.
(53) Kakita, M.; Okuno, M.; Hamaguchi, H.-o. *Journal of Biophotonics* **2013**, *6*, 256−259.
(54) Thomas, G. J., Jr. *Annu. Rev. Biophys. Biomol. Struct.* **1999**, *28*, 1−27.
(55) Russell, M. P.; Vohník, S.; Thomas, G. J. *Biophys. J.* **1995**, *68*, 1607−1612.
(56) Wen, Z. Q.; Thomas, G. J., Jr. *Biopolymers* **1998**, *45*, 247−256.
(57) Kitahama, Y.; Ozaki, Y. *Analyst* **2016**, *141*, 5020−5036.
(58) Schlücker, S. *Angew. Chem., Int. Ed.* **2014**, *53*, 4756−4795.
(59) Cialla, D.; März, A.; Böhme, R.; Theil, F.; Weber, K.; Schmitt, M.; Popp, J. *Anal. Bioanal. Chem.* **2012**, *403*, 27−54.
(60) Cardinal, M. F.; Vander Ende, E.; Hackler, R. A.; McAnally, M. O.; Stair, P. C.; Schatz, G. C.; Van Duyne, R. P. *Chem. Soc. Rev.* **2017**, *46*, 3886−3903.
(61) Langer, J.; Jimenez de Aberasturi, D.; Aizpurua, J.; Alvarez-Puebla, R. A.; Auguié, B.; Baumberg, J. J.; Bazan, G. C.; Bell, S. E. J.; Boisen, A.; Brolo, A. G.; Choo, J.; Cialla-May, D.; Deckert, V.; Fabris, L.; Faulds, K.; García de Abajo, F. J.; Goodacre, R.; Graham, D.; Haes, A. J.; Haynes, C. L.; Huck, C.; Itoh, T.; Käll, M.; Kneipp, J.; Kotov, N. A.; Kuang, H.; Le Ru, E. C.; Lee, H. K.; Li, J.-F.; Ling, X. Y.; Maier, S. A.; Mayerhöfer, T.; Moskovits, M.; Murakoshi, K.; Nam, J.-M.; Nie, S.; Ozaki, Y.; Pastoriza-Santos, I.; Perez-Juste, J.; Popp, J.; Pucci, A.; Reich, S.; Ren, B.; Schatz, G. C.; Shegai, T.; Schlücker, S.; Tay, L.-L.; Thomas, K. G.; Tian, Z.-Q.; Van Duyne, R. P.; Vo-Dinh, T.; Wang, Y.; Willets, K. A.; Xu, C.; Xu, H.; Xu, Y.; Yamamoto, Y. S.; Zhao, B.; Liz-Marzán, L. M. *ACS Nano* **2020**, *14*, 28−117.
(62) Lane, L. A.; Qian, X.; Nie, S. *Chem. Rev.* **2015**, *115*, 10489−10529.
(63) Le Ru, E. C.; Meyer, S. A.; Artur, C.; Etchegoin, P. G.; Grand, J.; Lang, P.; Maurel, F. *Chem. Commun.* **2011**, *47*, 3903−3905.
(64) Ayars, E. J.; Hallen, H. D.; Jahncke, C. L. *Phys. Rev. Lett.* **2000**, *85*, 4180−4183.
(65) Zong, C.; Xu, M.; Xu, L.-J.; Wei, T.; Ma, X.; Zheng, X.-S.; Hu, R.; Ren, B. *Chem. Rev.* **2018**, *118*, 4946−4980.
(66) Cialla-May, D.; Zheng, X. S.; Weber, K.; Popp, J. *Chem. Soc. Rev.* **2017**, *46*, 3945−3961.
(67) Laing, S.; Gracie, K.; Faulds, K. *Chem. Soc. Rev.* **2016**, *45*, 1901−1918.

(68) Szlag, V. M.; Rodriguez, R. S.; He, J.; Hudson-Smith, N.; Kang, H.; Le, N.; Reineke, T. M.; Haynes, C. L. *ACS Appl. Mater. Interfaces* **2018**, *10*, 31825−31844.
(69) Li, J.-F.; Zhang, Y.-J.; Ding, S.-Y.; Panneerselvam, R.; Tian, Z.-Q. *Chem. Rev.* **2017**, *117*, 5002−5069.
(70) Kumar, N.; Weckhuysen, B. M.; Wain, A. J.; Pollard, A. J. *Nat. Protoc.* **2019**, *14*, 1169−1193.
(71) Deckert-Gaudig, T.; Taguchi, A.; Kawata, S.; Deckert, V. *Chem. Soc. Rev.* **2017**, *46*, 4077−4110.
(72) Pozzi, E. A.; Goubert, G.; chiang, N.; Jiang, N.; Chapman, C. T.; McAnally, M. O.; Henry, A.-I.; Seideman, T.; Schatz, G. C.; Hersam, M. C.; Van Duyne, R. *Chem. Rev.* **2017**, *117*, 4961−4982.
(73) Richard-Lacroix, M.; Zhang, Y.; Dong, Z.; Deckert, V. *Chem. Soc. Rev.* **2017**, *46*, 3922−3944.
(74) Wang, X.; Huang, S.-C.; Huang, T.-X.; Su, H.-S.; Zhong, J.-H.; Zeng, Z.-C.; Ren, B. *Chem. Soc. Rev.* **2017**, *46*, 4020−4041.
(75) Zrimsek, A. B.; Chaing, N.; Mattei, M.; Zaleski, S.; McAnally, M. O.; Chapman, C. T.; Henry, A.-I.; Schatz, G. C.; Van Duyne, R. P. *Chem. Rev.* **2017**, *117*, 7583−7613.
(76) Sonntag, M. D.; Klingsporn, J. M.; Garbay, L. K.; Roberts, J. M.; Dieringer, J. A.; Seideman, T.; Scheidt, K. A.; Jensen, L.; Schatz, G. C.; Van Duyne, R. J. *J. Phys. Chem. C* **2012**, *116*, 478−483.
(77) Zumbusch, A.; Holtom, G. R.; Xie, X. S. *Phys. Rev. Lett.* **1999**, *82*, 4142−4145.
(78) Freudiger, C. W.; Min, W.; Saar, B. G.; Lu, S.; Holtom, G. R.; He, C.; Tsai, J. C.; Kang, J. X.; Xie, X. S. *Science* **2008**, *322*, 1857−1861.
(79) Freudiger, C. W.; Roeffaers, M. B. J.; Zhang, X.; Saar, B. G.; Min, W.; Xie, X. S. *J. Phys. Chem. B* **2011**, *115*, 5574−5581.
(80) Cui, M.; Bachler, B. R.; Ogilvie, J. P. *Opt. Lett.* **2009**, *34*, 773−775.
(81) Gottschall, T.; Meyer, T.; Baumgartl, M.; Jauregui, C.; Schmitt, M.; Popp, J.; Limpert, J.; Tünnermann, A. *Laser & Photonics Reviews* **2015**, *9*, 435−451.
(82) Lu, F. K.; Basu, S.; Igras, V.; Hoang, M. P.; Ji, M.; Fu, D.; Holtom, G. R.; Neel, V. A.; Freudiger, C. W.; Fisher, D. E.; Xie, X. S. *Proc. Natl. Acad. Sci. U. S. A.* **2015**, *112*, 11624−11629.
(83) Hu, F.; Shi, L.; Min, W. *Nat. Methods* **2019**, *16*, 830−842.
(84) Ji, M.; Lewis, S.; Camelo-Piragua, S.; Ramkissoon, S. H.; Snuderl, M.; Venneti, S.; Fisher-Hubbard, A.; Garrard, M.; Fu, D.; Wang, A. C.; Heth, J. A.; Maher, C. O.; Sanai, N.; Johnson, T. D.; Freudiger, C. W.; Sagher, O.; Xie, X. S.; Orringer, D. A. *Sci. Transl. Med.* **2015**, *7*, 309ra163.
(85) Orringer, D. A.; Pandian, B.; Niknafs, Y. S.; Hollon, T. C.; Boyle, J.; Lewis, S.; Garrard, M.; Hervey-Jumper, S. L.; Garton, H. J. L.; Maher, C. O.; Heth, J. A.; Sagher, O.; Wilkinson, D. A.; Snuderl, M.; Venneti, S.; Ramkissoon, S. H.; McFadden, K. A.; Fisher-Hubbard, A.; Lieberman, A. P.; Johnson, T. D.; Xie, X. S.; Trautman, J. K.; Freudiger, C. W.; Camelo-Piragua, S. *Nature biomedical engineering* **2017**, *1*, 0027.
(86) Ji, M.; Arbel, M.; Zhang, L.; Freudiger, C. W.; Hou, S. S.; Lin, D.; Yang, X.; Bacskai, B. J.; Xie, X. S. *Sci. Adv.* **2018**, *4*, eaat7715.
(87) Slipchenko, M. N.; Oglesbee, R. A.; Zhang, D.; Wu, W.; Cheng, J.-X. *Journal of Biophotonics* **2012**, *5*, 801−807.
(88) Lin, H.; Liao, C.-S.; Wang, P.; Kong, N.; Cheng, J.-X. *Light: Sci. Appl.* **2018**, *7*, 17179−17179.
(89) Wei, L.; Hu, F.; Shen, Y.; Chen, Z.; Yu, Y.; Lin, C.-C.; Wang, M. C; Min, W. *Nat. Methods* **2014**, *11*, 410.
(90) Wei, L.; Chen, Z.; Shi, L.; Long, R.; Anzalone, A. V.; Zhang, L.; Hu, F.; Yuste, R.; Cornish, V. W.; Min, W. *Nature* **2017**, *544*, 465−470.
(91) Xiong, H.; Shi, L.; Wei, L.; Shen, Y.; Long, R.; Zhao, Z.; Min, W. *Nat. Photonics* **2019**, *13*, 412−417.
(92) Camp, C. H., Jr.; Lee, Y. J.; Heddleston, J. M.; Hartshorn, C. M.; Walker, A. R. H.; Rich, J. N.; Lathia, J. D.; Cicerone, M. T. *Nat. Photonics* **2014**, *8*, 627−634.
(93) Zirak, P.; Matz, G.; Messerschmidt, B.; Meyer, T.; Schmitt, M.; Popp, J.; Uckermann, O.; Galli, R.; Kirsch, M.; Winterhalder, M. J.; Zumbusch, A. *APL Photonics* **2018**, *3*, No. 092409.
(94) Lukic, A.; Dochow, S.; Bae, H.; Matz, G.; Latka, I.; Messerschmidt, B.; Schmitt, M.; Popp, J. *Optica* **2017**, *4*, 496−501.
(95) Lombardini, A.; Mytskaniuk, V.; Sivankutty, S.; Andresen, E. R.; Chen, X.; Wenger, J.; Fabert, M.; Joly, N.; Louradour, F.; Kudlinski, A.; Rigneault, H. *Light: Sci. Appl.* **2018**, *7*, 10.
(96) Satoh, S.; Otsuka, Y.; Ozeki, Y.; Itoh, K.; Hashiguchi, A.; Yamazaki, K.; Hashimoto, H.; Sakamoto, M. *Pathol. Int.* **2014**, *64*, 518−526.
(97) Brückner, M.; Becker, K.; Popp, J.; Frosch, T. *Anal. Chim. Acta* **2015**, *894*, 76−84.
(98) Frosch, T.; Wyrwich, E.; Yan, D.; Popp, J.; Frosch, T. *Molecules* **2019**, *24*, 4381.
(99) Frosch, T.; Wyrwich, E.; Yan, D.; Domes, C.; Domes, R.; Popp, J.; Frosch, T. *Molecules* **2019**, *24*, 3229.
(100) Saleh, T. A.; Al-Shalalfeh, M. M.; Al-Saadi, A. A. *Sens. Actuators, B* **2018**, *254*, 1110−1117.
(101) Hidi, I. J.; Jahn, M.; Pletz, M. W.; Weber, K.; Cialla-May, D.; Popp, J. *J. Phys. Chem. C* **2016**, *120*, 20613−20623.
(102) Hidi, I. J.; Jahn, M.; Weber, K.; Bocklitz, T.; Pletz, M. W.; Cialla-May, D.; Popp, J. *Anal. Chem.* **2016**, *88*, 9173−9180.
(103) Ranc, V.; Markova, Z.; Hajduch, M.; Prucek, R.; Kvitek, L.; Kaslik, J.; Safarova, K.; Zboril, R. *Anal. Chem.* **2014**, *86*, 2939−2946.
(104) Han, G.; Liu, R.; Han, M.-Y.; Jiang, C.; Wang, J.; Du, S.; Liu, B.; Zhang, Z. *Anal. Chem.* **2014**, *86*, 11503−11507.
(105) Hu, Y.; Cheng, H.; Zhao, X.; Wu, J.; Muhammad, F.; Lin, S.; He, J.; Zhou, L.; Zhang, C.; Deng, Y.; Wang, P.; Zhou, Z.; Nie, S.; Wei, H. *ACS Nano* **2017**, *11*, 5558−5566.
(106) Frosch, T.; Knebl, A.; Frosch, T. *Nanophotonics* **2019**, *9*, 19−37.
(107) Azkune, M.; Frosch, T.; Arrospide, E.; Aldabaldetreku, G.; Bikandi, I.; Zubia, J.; Popp, J.; Frosch, T. *J. Lightwave Technol.* **2019**, *37*, 2981−2988.
(108) Jiang, Y.; Sun, D.-W.; Pu, H.; Wei, Q. *Trends Food Sci. Technol.* **2018**, *75*, 10−22.
(109) Xu, M.-L.; Gao, Y.; Han, X. X.; Zhao, B. *J. Agric. Food Chem.* **2017**, *65*, 6719−6726.
(110) Li, J.-L.; Sun, D.-W.; Pu, H.; Jayas, D. *Food Chem.* **2017**, *218*, 543−552.
(111) Wang, K.; Sun, D.-W.; Pu, H.; Wei, Q. *Talanta* **2019**, *191*, 449−456.
(112) Li, D.; Ma, Y.; Duan, H.; Deng, W.; Li, D. *Biosens. Bioelectron.* **2018**, *99*, 389−398.
(113) Giovannozzi, A. M.; Rolle, F.; Sega, M.; Abete, M. C.; Marchis, D.; Rossi, A. M. *Food Chem.* **2014**, *159*, 250−256.
(114) Qiu, Y.; Deng, D.; Deng, Q.; Wu, P.; Zhang, H.; Cai, C. *J. Mater. Chem. B* **2015**, *3*, 4487−4495.
(115) Xu, Y.; Kutsanedzie, F. Y. H.; Hassan, M. M.; Li, H.; Chen, Q. *Spectrochim. Acta, Part A* **2019**, *206*, 405−412.
(116) Qi, M.; Huang, X.; Zhou, Y.; Zhang, L.; Jin, Y.; Peng, Y.; Jiang, H.; Du, S. *Food Chem.* **2016**, *197*, 723−729.
(117) Withnall, R.; Chowdhry, B. Z.; Silver, J.; Edwards, H. G. M.; de Oliveira, L. F. C. *Spectrochim. Acta, Part A* **2003**, *59A*, 2207−2212.
(118) Kumar, B. N. V.; Kampe, B.; Rosch, P.; Popp, J. *Analyst* **2015**, *140*, 4584−4593.
(119) Gehse, S.; Knorr, F.; Patzelt, A.; Zastrow, L.; Meinke, M. C.; Lademann, J.; Darvin, M. E. *Laser Phys.* **2018**, *28*, 105602.
(120) Koch, M.; Zagermann, S.; Kniggendorf, A. K.; Meinhardt-Wollweber, M.; Roth, B. J. *J. Raman Spectrosc.* **2017**, *48*, 686−691.
(121) Rüger, J.; Mondol, A. S.; Schie, I.; Popp, J.; Krafft, C. *Analyst* **2019**, *144*, 4488−4492.
(122) Thompson, C. M.; North, E. W.; White, S. N.; Gallager, S. M. J. *J. Raman Spectrosc.* **2014**, *45*, 349−358.
(123) Kumar, B. N. V.; Kampe, B.; Rösch, P.; Popp, J. *Environ. Sci. Pollut. Res.* **2015**, *22*, 19317−19325.
(124) Gracie, K.; Pang, S.; Jones, G. M.; Faulds, K.; Braybrook, J.; Graham, D. *Anal. Methods* **2017**, *9*, 1589−1594.
(125) Darvin, M.; Gersonde, I.; Meinke, M.; Sterry, W.; Lademann, J. J. *J. Phys. D: Appl. Phys.* **2005**, *38*, 2696−2700.
(126) Caspers, P. J.; Nico, C.; de Sterke, J.; Pudney, P. D.; Curto, P. R.; Illand, A.; Puppels, G. J. *Translational Biophotonics* **2019**, *1*, e201900004.

https://doi.org/10.1021/acs.analchem.1c03235
Anal. Chem. 2022, 94, 86−119

(127) Jahns, L.; Johnson, L. K.; Conrad, Z.; Bukowski, M.; Raatz, S. K.; Jilcott Pitts, S.; Wang, Y.; Ermakov, I. V.; Gellermann, W. *Nutr. J.* **2019**, *18*, 78.
(128) Domes, C.; Domes, R.; Popp, J.; Pletz, M. W.; Frosch, T. *Anal. Chem.* **2017**, *89*, 9997−10003.
(129) D'Elia, V.; Montalvo, G.; Ruiz, C. G.; Ermolenkov, V. V.; Ahmed, Y.; Lednev, I. K. *Spectrochim. Acta, Part A* **2018**, *188*, 338−340.
(130) Bhunia, S.; Donfack, P.; Materny, A.; Ojha, A. K. *J. Raman Spectrosc.* **2016**, *47*, 1086−1094.
(131) Marini, M.; Allione, M.; Torre, B.; Moretti, M.; Limongi, T.; Tirinato, L.; Giugni, A.; Das, G.; di Fabrizio, E. *Microelectron. Eng.* **2017**, *175*, 38−42.
(132) Friedman, S. J.; Terentis, A. C. *J. Raman Spectrosc.* **2016**, *47*, 259−268.
(133) Muntean, C. M.; Bratu, I.; Tripon, C.; Nalpantidis, K.; Purcaru, M. A.; Deckert, V. *Rev. Chim.* **2017**, *68*, 2471−2476.
(134) Rydzak, J. W.; White, D. E.; Airiau, C. Y.; Sterbenz, J. T.; York, B. D.; Clancy, D. J.; Dai, Q. *Org. Process Res. Dev.* **2015**, *19*, 203−214.
(135) Chen, D.; Li, Y.; Tan, Z.; Huang, Z.-x.; Zong, J.; Li, Q.-f. *Int. Dairy J.* **2019**, *96*, 132−137.
(136) Jiao, X.; Meng, Y.; Wang, K.; Huang, W.; Li, N.; Liu, T. C. Y. *Molecules* **2019**, *24*, 1889.
(137) Singh, R.; Wrobel, T. P.; Mukherjee, P.; Gryka, M.; Kole, M.; Harrison, S.; Bhargava, R. *Appl. Spectrosc.* **2019**, *73*, 687−697.
(138) Mandrile, L.; Amato, G.; Marchis, D.; Martra, G.; Rossi, A. M. *Food Chem.* **2017**, *229*, 268−275.
(139) Torres-Nuñez, A.; Faulds, K.; Graham, D.; Alvarez-Puebla, R. A.; Guerrini, L. *Analyst* **2016**, *141*, 5170−5180.
(140) Xu, L.-J.; Lei, Z.-C.; Li, J.; Zong, C.; Yang, C. J.; Ren, B. *J. Am. Chem. Soc.* **2015**, *137*, 5149−5154.
(141) Morla-Folch, J.; Xie, H.-n.; Gisbert-Quilis, P.; Pedro, S. G.-d.; Pazos-Perez, N.; Alvarez-Puebla, R. A.; Guerrini, L. *Angew. Chem., Int. Ed.* **2015**, *54*, 13650−13654.
(142) Morla-Folch, J.; Xie, H.-n.; Alvarez-Puebla, R. A.; Guerrini, L. *ACS Nano* **2016**, *10*, 2834−2842.
(143) Garcia-Rico, E.; Alvarez-Puebla, R. A.; Guerrini, L. *Chem. Soc. Rev.* **2018**, *47*, 4909−4923.
(144) Su, J.; Wang, D.; Nörbel, L.; Shen, J.; Zhao, Z.; Dou, Y.; Peng, T.; Shi, J.; Mathur, S.; Fan, C.; Song, S. *Anal. Chem.* **2017**, *89*, 2531−2538.
(145) Ma, W.; Fu, P.; Sun, M.; Xu, L.; Kuang, H.; Xu, C. *J. Am. Chem. Soc.* **2017**, *139*, 11752−11759.
(146) Bruzas, I.; Lum, W.; Gorunmez, Z.; Sagle, L. *Analyst* **2018**, *143*, 3990−4008.
(147) Matteini, P.; Cottat, M.; Tavanti, F.; Panfilova, E.; Scuderi, M.; Nicotra, G.; Menziani, M. C.; Khlebtsov, N.; de Angelis, M.; Pini, R. *ACS Nano* **2017**, *11*, 918−926.
(148) Farka, Z.; Juřík, T.; Kovář, D.; Trnková, L.; Skládal, P. *Chem. Rev.* **2017**, *117*, 9973−10042.
(149) Wang, Z.; Zong, S.; Wu, L.; Zhu, D.; Cui, Y. *Chem. Rev.* **2017**, *117*, 7910−7963.
(150) Zhang, D.; Huang, L.; Liu, B.; Ni, H.; Sun, L.; Su, E.; Chen, H.; Gu, Z.; Zhao, X. *Biosens. Bioelectron.* **2018**, *106*, 204−211.
(151) Tran, V.; Walkenfort, B.; König, M.; Salehi, M.; Schlücker, S. *Angew. Chem., Int. Ed.* **2019**, *58*, 442−446.
(152) Wood, B. R.; Ashgari-Khiavi, M.; Bailo, E.; McNaughton, D.; Deckert, V. *Nano Lett.* **2012**, *12*, 1555−1560.
(153) Rusciano, G.; Isticato, R.; Sirec, T.; Ricca, E.; Bailo, E.; Sasso, A. *ACS Nano* **2014**, *8*, 12300−12309.
(154) Olschewski, K.; Kämmer, E.; Stöckel, S.; Bocklitz, T.; Deckert-Gaudig, T.; Zell, R.; Cialla-May, D.; Weber, K.; Deckert, V.; Popp, J. *Nanoscale* **2015**, *7*, 4545−4552.
(155) Hermann, P.; Fabian, H.; Naumann, D.; Hermelink, A. J. *J. Phys. Chem. C* **2011**, *115*, 24512−24520.
(156) Cialla, D.; Deckert-Gaudig, T.; Budich, C.; Laue, M.; Möller, R.; Naumann, D.; Deckert, V.; Popp, J. J. *J. Raman Spectrosc.* **2009**, *40*, 240−243.
(157) Lipiec, E.; Perez-Guaita, D.; Kaderli, J.; Wood, B. R.; Zenobi, R. *Angew. Chem., Int. Ed.* **2018**, *57*, 8519−8524.
(158) Tabatabaei, M.; Caetano, F. A.; Pashee, F.; Ferguson, S. S. G.; Lagugne-Labarthet, F. *Analyst* **2017**, *142*, 4415−4421.
(159) vandenAkker, C.; Deckert-Gaudig, T.; Schleeger, M.; Velikov, K. P.; Deckert, V.; Bonn, M.; Koenderink, G. H. *Small* **2015**, *11*, 4131−4139.
(160) Kurouski, D.; Deckert-Gaudig, T.; Deckert, V.; Lednev, I. K. *Biophys. J.* **2013**, *104*, 49A.
(161) He, Z.; Han, Z.; Kizer, M.; Linhardt, R. J.; Wang, X.; Sinyukov, A. M.; Wang, J.; Deckert, V.; Sokolov, A. V.; Hu, J.; Scully, M. O. *J. Am. Chem. Soc.* **2019**, *141*, 753−757.
(162) Lin, X.; Deckert-Gaudig, T.; Singh, P.; Siegmann, M.; Kupfer, S.; Zhang, Z.; Gräfe, S.; Deckert, V. Direct Base-to-Base Transitions in ssDNA Revealed by Tip-Enhanced Raman Scattering. *arXiv*, **2016**, 1604.06598.
(163) Japaridze, A.; Vobronik, D.; Lipiec, E.; Cerreta, A.; Szczerbinski, J.; Zenobi, R.; Dieter, G. *Macromolecules* **2016**, *49*, 643−652.
(164) Najjar, S.; Talaga, D.; Schué, L.; Coffinier, Y.; Szunerits, S.; Boukherroub, R.; Servant, L.; Rodriguez, V.; Bonhommeau, S. J. *J. Phys. Chem. C* **2014**, *118*, 1174−1181.
(165) Bonhommeau, S.; Lecomte, S. *ChemPhysChem* **2018**, *19*, 8−18.
(166) Lipiec, E.; Sekine, R.; Bielecki, J.; Kwiatek, W. M.; Wood, B. R. *Angew. Chem., Int. Ed.* **2014**, *53*, 169−172.
(167) López-Peña, I.; Leigh, B. S.; Schlamadinger, D. E.; Kim, J. E. *Biochemistry* **2015**, *54*, 4770−4783.
(168) Kakita, M.; Okuno, M.; Hamaguchi, H. o. *J. Biophotonics* **2013**, *6*, 256−259.
(169) Okotrub, K. A.; Surovtsev, N. V. *J. Photochem. Photobiol., B* **2014**, *141*, 269−274.
(170) Domes, R.; Domes, C.; Albert, C. R.; Bringmann, G.; Popp, J.; Frosch, T. *Phys. Chem. Chem. Phys.* **2017**, *19*, 29918−29926.
(171) Todorovic, S.; Teixeira, M. *JBIC, J. Biol. Inorg. Chem.* **2018**, *23*, 647−661.
(172) Amin, A.; Ghouri, N.; Ali, S.; Ahmed, M.; Saleem, M.; Qazi, J. *J. Raman Spectrosc.* **2017**, *48*, 705−710.
(173) Mahmood, T.; Nawaz, H.; Ditta, A.; Majeed, M.; Hanif, M.; Rashid, N.; Bhatti, H.; Nargis, H.; Saleem, M.; Bonnier, F. *Spectrochim. Acta, Part A* **2018**, *200*, 136−142.
(174) Ditta, A.; Nawaz, H.; Mahmood, T.; Majeed, M.; Tahir, M.; Rashid, N.; Mudassar, M.; Alsaadi, A.; Byrne, H. *Spectrochim. Acta, Part A* **2019**, *221*, 117173.
(175) Otange, B.; Birech, Z.; Rop, R.; Oyugi, J. *J. Raman Spectrosc.* **2019**, *50*, 620−628.
(176) Pang, Y.; Wang, J.; Xiao, R.; Wang, S. *Biosens. Bioelectron.* **2014**, *61*, 460−465.
(177) Lee, K. Y. J.; Wang, Y.; Nie, S. *RSC Adv.* **2015**, *5*, 65651−65659.
(178) Lee, J.-H.; Kim, B.-C.; Byeung-Keun, O. H.; Choi, J.-W. *J. Biomed. Nanotechnol.* **2015**, *11*, 2223−2230.
(179) Sinha, S. S.; Jones, S.; Pramanik, A.; Ray, P. C. *Acc. Chem. Res.* **2016**, *49*, 2725−2735.
(180) Sivashanmugan, K.; Liao, J.-D.; You, J.-W.; Wu, C.-L. *Sens. Actuators, B* **2013**, *181*, 361−367.
(181) Luo, Z.; Chen, L.; Liang, C.; Wei, Q.; Chen, Y.; Wang, J. *Microchim. Acta* **2017**, *184*, 3505−3511.
(182) Durmanov, N. N.; Guliev, R. R.; Eremenko, A. V.; Boginskaya, I. A.; Ryzhikov, I. A.; Trifonova, E. A.; Putlyaev, E. V.; Mukhin, A. N.; Kalnov, S. L.; Balandina, M. V.; Tkachuk, A. P.; Gushchin, V. A.; Sarychev, A. K.; Lagarkov, A. N.; Rodionov, I. A.; Gabidullin, A. R.; Kurochkin, I. N. *Sens. Actuators, B* **2018**, *257*, 37−47.
(183) Lorenz, B.; Wichmann, C.; Stöckel, S.; Rösch, P.; Popp, J. *Trends Microbiol.* **2017**, *25*, 413−424.
(184) Stöckel, S.; Kirchhoff, J.; Neugebauer, U.; Rösch, P.; Popp, J. J. *J. Raman Spectrosc.* **2016**, *47*, 89−109.
(185) Pahlow, S.; Meisel, S.; Cialla-May, D.; Weber, K.; Rösch, P.; Popp, J. *Adv. Drug Delivery Rev.* **2015**, *89*, 105−120.
(186) Ren, Y.; Ji, Y. T.; Teng, L.; Zhang, H. P. *Microb. Cell Fact.* **2017**, *16*, 233.
(187) Stöckel, S.; Stanca, A. S.; Helbig, J.; Rösch, P.; Popp, J. *Anal. Bioanal. Chem.* **2015**, *407*, 8919−8923.

(188) Zeiri, L.; Bronk, B. V.; Shabtai, Y.; Eichler, J.; Efrima, S. *Appl. Spectrosc.* **2004**, *58*, 33−40.
(189) Witkowska, E.; Nicinski, K.; Korsak, D.; Szymborski, T.; Kaminska, A. *Anal. Bioanal. Chem.* **2019**, *411*, 2001−2017.
(190) Efrima, S.; Zeiri, L. J. *J. Raman Spectrosc.* **2009**, *40*, 277−288.
(191) Premasiri, W. R.; Lee, J. C.; Sauer-Budge, A.; Théberge, R.; Costello, C. E.; Ziegler, L. D. *Anal. Bioanal. Chem.* **2016**, *408*, 4631−4647.
(192) Premasiri, W. R.; Chen, Y.; Williamson, P. M.; Bandarage, D. C.; Pyles, C.; Ziegler, L. D. *Anal. Bioanal. Chem.* **2017**, *409*, 3043−3054.
(193) Pahlow, S.; Stöckel, S.; Pollok, S.; Cialla-May, D.; Rösch, P.; Weber, K.; Popp, J. *Anal. Chem.* **2016**, *88*, 1570−1577.
(194) Kusić, D.; Rösch, P.; Popp, J. *Syst. Appl. Microbiol.* **2016**, *39*, 132−140.
(195) Lorenz, B.; Rösch, P.; Popp, J. *Anal. Bioanal. Chem.* **2019**, *411*, 5445−5454.
(196) Ghebremedhin, M.; Heitkamp, R.; Yesupriya, S.; Clay, B.; Crane, N. J. J. *J. Clin. Microbiol.* **2017**, *55*, 2480−2490.
(197) Stöckel, S.; Meisel, S.; Lorenz, B.; Kloß, S.; Henk, S.; Dees, S.; Richter, E.; Andres, S.; Merker, M.; Labugger, I.; Rösch, P.; Popp, J. J. *Biophotonics* **2017**, *10*, 727−734.
(198) Baron, V. O.; Chen, M. Z.; Clark, S. O.; Williams, A.; Hammond, R. J. H.; Dholakia, K.; Gillespie, S. H. *Sci. Rep.* **2017**, *7*, 9844.
(199) Stöckel, S.; Meisel, S.; Elschner, M.; Melzer, F.; Rösch, P.; Popp, J. *Anal. Bioanal. Chem.* **2015**, *407*, 787−794.
(200) Moawad, A. A.; Silge, A.; Bocklitz, T.; Fischer, K.; Rösch, P.; Roesler, U.; Elschner, M. C.; Popp, J.; Neubauer, H. *Molecules* **2019**, *24*, 4516.
(201) Kirchhoff, J.; Glaser, U.; Bohnert, J. A.; Pletz, M. W.; Popp, J.; Neugebauer, U. *Anal. Chem.* **2018**, *90*, 1811−1818.
(202) Wang, Y.; Huang, W. E.; Cui, L.; Wagner, M. *Curr. Opin. Biotechnol.* **2016**, *41*, 34−42.
(203) Taubert, M.; Stöckel, S.; Geesink, P.; Girnus, S.; Jehmlich, N.; von Bergen, M.; Rösch, P.; Popp, J.; Küsel, K. *Environ. Microbiol.* **2018**, *20*, 369−384.
(204) Olaniyi, O. O.; Yang, K.; Zhu, Y. G.; Cui, L. *Appl. Microbiol. Biotechnol.* **2019**, *103*, 1455−1464.
(205) Li, H. Z.; Bi, Q. F.; Yang, K.; Zheng, B. X.; Pu, Q.; Cui, L. *Anal. Chem.* **2019**, *91*, 2239−2246.
(206) Cui, L.; Yang, K.; Li, H. Z.; Zhang, H.; Su, J. Q.; Paraskevaidi, M.; Martin, F. L.; Ren, B.; Zhu, Y. G. *Anal. Chem.* **2018**, *90*, 5082−5089.
(207) Kumar, B. N. V.; Guo, S.; Bocklitz, T.; Rosch, P.; Popp, J. *Anal. Chem.* **2016**, *88*, 7574−7582.
(208) Wang, Y.; Song, Y.; Tao, Y.; Muhamadali, H.; Goodacre, R.; Zhou, N.-Y.; Preston, G. M.; Xu, J.; Huang, W. E. *Anal. Chem.* **2016**, *88*, 9443−9450.
(209) Ghita, A.; Pascut, F. C.; Sottile, V.; Denning, C.; Notingher, I. *EPJ. Techniques and Instrumentation* **2015**, *2*, 6.
(210) Schie, I. W.; Alber, L.; Gryshuk, A. L.; Chan, J. W. *Analyst* **2014**, *139*, 2726−2733.
(211) Farhane, Z.; Bonnier, F.; Maher, M. A.; Bryant, J.; Casey, A.; Byrne, H. J. J. *Biophotonics* **2017**, *10*, 151−165.
(212) Kann, B.; Offerhaus, H. L.; Windbergs, M.; Otto, C. *Adv. Drug Delivery Rev.* **2015**, *89*, 71−90.
(213) Schie, I. W.; Nolte, L.; Pedersen, T. L.; Smith, Z.; Wu, J.; Yahiatene, I.; Newman, J. W.; Huser, T. *Analyst* **2013**, *138*, 6662−6670.
(214) Stiebing, C.; Matthäus, C.; Krafft, C.; Keller, A.-A.; Weber, K.; Lorkowski, S.; Popp, J. *Anal. Bioanal. Chem.* **2014**, *406*, 7037−7046.
(215) Krafft, C.; Schie, I.; Meyer, T.; Schmitt, M.; Popp, J. *Chem. Soc. Rev.* **2016**, *45*, 1819−1849.
(216) Krafft, C.; Schmitt, M.; Schie, I.; Cialla-May, D.; Matthaeus, C.; Bocklitz, T.; Popp, J. *Angew. Chem., Int. Ed.* **2017**, *56*, 4392−4430.
(217) Schie, I. W.; Huser, T. *Appl. Spectrosc.* **2013**, *67*, 813−828.
(218) Huser, T.; Chan, J. *Adv. Drug Delivery Rev.* **2015**, *89*, 57−70.
(219) Ilin, Y.; Choi, J. S.; Harley, B. A. C.; Kraft, M. L. *Anal. Chem.* **2015**, *87*, 11317−11324.
(220) Ichimura, T.; Chiu, L.-d.; Fujita, K.; Kawata, S.; Watanabe, T. M.; Yanagida, T.; Fujita, H. *PLoS One* **2014**, *9*, e84478.
(221) Brauchle, E.; Knopf, A.; Bauer, H.; Shen, N.; Linder, S.; Monaghan, M. G.; Ellwanger, K.; Layland, S. L.; Brucker, S. Y.; Nsair, A.; Schenke-Layland, K. *Stem Cell Rep.* **2016**, *6*, 188−199.
(222) Chiang, Y.-H.; Wu, S. H.; Kuo, Y.-C.; Chen, H.-F.; Chiou, A.; Lee, O. K. *Stem Cell Res. Ther.* **2015**, *6*, 81.
(223) Hashimoto, A.; Yamaguchi, Y.; Chiu, L.-d.; Morimoto, C.; Fujita, K.; Takedachi, M.; Kawata, S.; Murakami, S.; Tamiya, E. *Sci. Rep.* **2015**, *5*, 12529.
(224) Schie, I. W.; Krafft, C.; Popp, J. *J. Biophotonics* **2016**, *9*, 994−1000.
(225) Chen, H.; Li, X.; Broderick, N.; Liu, Y.; Zhou, Y.; Han, J.; Xu, W. *J. Biophotonics* **2018**, *11*, No. e201800016.
(226) Schie, I. W.; Kiselev, R.; Krafft, C.; Popp, J. *Analyst* **2016**, *141*, 6387−6395.
(227) Schie, I. W.; Rüger, J.; Mondol, A. S.; Ramoji, A.; Neugebauer, U.; Krafft, C.; Popp, J. *Anal. Chem.* **2018**, *90*, 2023−2030.
(228) Rüger, J.; Mondol, A. S.; Schie, I. W.; Popp, J.; Krafft, C. *Analyst* **2019**, *144*, 4488−4492.
(229) Mondol, A. S.; Patel, M. D.; Rüger, J.; Stiebing, C.; Kleiber, A.; Henkel, T.; Popp, J.; Schie, I. W. *Sensors* **2019**, *19*, 4428.
(230) Mondol, A. S.; Töpfer, N.; Rüger, J.; Neugebauer, U.; Popp, J.; Schie, I. W. *Sci. Rep.* **2019**, *9*, 12653.
(231) Mondol, A. S.; El-Mashtoly, S. F.; Frick, T.; Gerwert, K.; Popp, J.; Schie, I. W. *Analyst* **2019**, *144*, 6098−6107.
(232) Muller, W.; Kielhorn, M.; Schmitt, M.; Popp, J.; Heintzmann, R. *Optica* **2016**, *3*, 452−457.
(233) Schmälzlin, E.; Moralejo, B.; Bodenmüller, D.; Darvin, M.; Thiede, G.; Roth, M. M. *J. Sens. Sens. Syst.* **2016**, *5*, 261−271.
(234) Bergner, N.; Medyukhina, A.; Geiger, K. D.; Kirsch, M.; Schackert, G.; Krafft, C.; Popp, J. *Anal. Bioanal. Chem.* **2013**, *405*, 8719−8728.
(235) Bergholt, M. S.; St-Pierre, J.-P.; Offeddu, G. S.; Parmar, P. A.; Albro, M. B.; Puetzer, J. L.; Oyen, M. L.; Stevens, M. M. *ACS Cent. Sci.* **2016**, *2*, 885−895.
(236) You, A. Y.; Bergholt, M. S.; St-Pierre, J.-P.; Kit-Anan, W.; Pence, I. J.; Chester, A. H.; Yacoub, M. H.; Bertazzo, S.; Stevens, M. M. *Science advances* **2017**, *3*, No. e1701156.
(237) Bergner, N.; Bocklitz, T.; Romeike, B. F. M.; Reichart, R.; Kalff, R.; Krafft, C.; Popp, J. *Chemom. Intell. Lab. Syst.* **2012**, *117*, 224−232.
(238) Kong, K.; Rowlands, C. J.; Varma, S.; Perkins, W.; Leach, I. H.; Koloydenko, A. A.; Williams, H. C.; Notingher, I. *Proc. Natl. Acad. Sci. U. S. A.* **2013**, *110*, 15189−15194.
(239) Boitor, R.; Kong, K.; Shipp, D.; Varma, S.; Koloydenko, A.; Kulkarni, K.; Elsheikh, S.; Schut, T. B.; Caspers, P.; Puppels, G.; van der Wolf, M.; Sokolova, E.; Nijsten, T. E. C.; Salence, B.; Williams, H.; Notingher, I. *Biomed. Opt. Express* **2017**, *8*, 5749−5766.
(240) Wei, M.; Shi, L.; Shen, Y.; Zhao, Z.; Guzman, A.; Kaufman, L. J.; Wei, L.; Min, W. *Proc. Natl. Acad. Sci. U. S. A.* **2019**, *116*, 6608−6617.
(241) Zhang, L.; Shi, L.; Shen, Y.; Miao, Y.; Wei, M.; Qian, N.; Liu, Y.; Min, W. *Nature biomedical engineering* **2019**, *3*, 402−413.
(242) Shi, L.; Zheng, C.; Shen, Y.; Chen, Z.; Silveira, E. S.; Zhang, L.; Wei, M.; Liu, C.; de Sena-Tomas, C.; Targoff, K.; Min, W. *Nat. Commun.* **2018**, *9*, 2995.
(243) Fu, D.; Yang, W.; Xie, X. S. *J. Am. Chem. Soc.* **2017**, *139*, 583−586.
(244) Uckermann, O.; Galli, R.; Tamosaityte, S.; Leipnitz, E.; Geiger, K. D.; Schackert, G.; Koch, E.; Steiner, G.; Kirsch, M. *PLoS One* **2014**, *9*, No. e107115.
(245) Tian, F.; Yang, W.; Mordes, D. A.; Wang, J.-Y.; Salameh, J. S.; Mok, J.; Chew, J.; Sharma, A.; Leno-Duran, E.; Suzuki-Uematsu, S.; Suzuki, N.; Han, S. S.; Lu, F.-K.; Ji, M.; Zhang, R.; Liu, Y.; Strominger, J.; Shneider, N. A.; Petrucelli, L.; Xie, X. S.; Eggan, K. *Nat. Commun.* **2016**, *7*, 13283.
(246) Li, J.; Condello, S.; Thomes-Pepin, J.; Ma, X.; Xia, Y.; Hurley, T. D.; Matei, D.; Cheng, J.-X. *Cell Stem Cell* **2017**, *20*, 303−314.E5.
(247) Yue, S.; Li, J.; Lee, S.-Y.; Lee, H. J.; Shao, T.; Song, B.; Cheng, L.; Masterson, T. A.; Liu, X.; Ratliff, T. L.; Cheng, J.-X. *Cell Metab.* **2014**, *19*, 393−406.

https://doi.org/10.1021/acs.analchem.1c03235
Anal. Chem. 2022, 94, 86−119

(248) Sarri, B.; Canonge, R.; Audier, X.; Simon, E.; Wojak, J.; Caillol, F.; Cador, C.; Marguet, D.; Poizat, F.; Giovannini, M.; Rigneault, H. *Sci. Rep.* **2019**, *9*, 10052.
(249) Bocklitz, T. W.; Salah, F. S.; Vogler, N.; Heuke, S.; Chernavskaia, O.; Schmidt, C.; Waldner, M. J.; Greten, F. R.; Brauer, R.; Schmitt, M.; Stallmach, A.; Petersen, I.; Popp, J. *BMC Cancer* **2016**, *16*, 534.
(250) Cordero, E.; Latka, I.; Matthaus, C.; Schie, I.; Popp, J. *J. Biomed. Opt.* **2018**, *23*, 1−23.
(251) Pence, I. J.; Beaulieu, D. B.; Horst, S. N.; Bi, X.; Herline, A. J.; Schwartz, D. A.; Mahadevan-Jansen, A. *Biomed. Opt. Express* **2017**, *8*, 524−535.
(252) Zuvela, P.; Lin, K.; Shu, C.; Zheng, W.; Lim, C. M.; Huang, Z. *Anal. Chem.* **2019**, *91*, 8101−8108.
(253) Lin, K.; Zheng, W.; Lim, C. M.; Huang, Z. *Theranostics* **2017**, *7*, 3517−3526.
(254) Lin, K.; Wang, J.; Zheng, W.; Ho, K. Y.; Teh, M.; Yeoh, K. G.; Huang, Z. *Cancer Prev. Res.* **2016**, *9*, 476−483.
(255) Wang, J.; Lin, K.; Zheng, W.; Ho, K. Y.; Teh, M.; Yeoh, K. G.; Huang, Z. *Faraday Discuss.* **2016**, *187*, 377−392.
(256) Bergholt, M. S.; Lin, K.; Wang, J.; Zheng, W.; Xu, H.; Huang, Q.; Ren, J.-l.; Ho, K. Y.; Teh, M.; Srivastava, S.; Wong, B.; Yeoh, K. G.; Huang, Z. *J. Biophotonics* **2016**, *9*, 333−342.
(257) Lin, D.; Qiu, S.; Huang, W.; Pan, J.; Xu, Z.; Chen, R.; Feng, S.; Chen, G.; Li, Y.; Short, M.; Zhao, J.; Fawzy, Y.; Zeng, H. *J. Biophotonics* **2018**, *11*, No. e201700251.
(258) Matthaus, C.; Dochow, S.; Egodage, K. D.; Romeike, B. F.; Brehm, B. R.; Popp, J. *J. Biomed. Opt.* **2018**, *23*, 1−6.
(259) Wang, J.; Zheng, W.; Lin, K.; Huang, Z. *J. Biophotonics* **2018**, *11*, e201700113.
(260) Ding, H.; Dupont, A. W.; Singhal, S.; Scott, L. D.; Guha, S.; Younes, M.; Ye, Y.; Bi, X. *J. Raman Spectrosc.* **2017**, *48*, 902−909.
(261) Carvalho, L.; Nogueira, M. S.; Bhattacharjee, T.; Neto, L. P. M.; Daun, L.; Mendes, T. O.; Rajasekaran, R.; Chagas, M.; Martin, A. A.; Soares, L. E. S. *Clin Oral Investig* **2019**, *23*, 3021−3031.
(262) Bergholt, M. S.; Zheng, W.; Lin, K.; Wang, J.; Xu, H.; Ren, J.-l.; Ho, K. Y.; Teh, M.; Yeoh, K. G.; Huang, Z. *Anal. Chem.* **2015**, *87*, 960−966.
(263) Pinto, M.; Zorn, K. C.; Tremblay, J. P.; Desroches, J.; Dallaire, F.; Aubertin, K.; Marple, E.; Kent, C.; Leblond, F.; Trudel, D.; Lesage, F. *J. Biomed. Opt.* **2019**, *24*, 1−10.
(264) O'Brien, C. M.; Vargis, E.; Rudin, A.; Slaughter, J. C.; Thomas, G.; Newton, J. M.; Reese, J.; Bennett, K. A.; Mahadevan-Jansen, A. *Am. J. Obstet. Gynecol.* **2018**, *218*, 528.e1−528.e18.
(265) Wu, Z.; Jiang, L.; Wang, W.; Zhao, J.; Lui, H.; Zeng, H. *Opt. Lett.* **2019**, *44*, 1383−1386.
(266) Schmalzlin, E.; Moralejo, B.; Gersonde, I.; Schleusener, J.; Darvin, M. E.; Thiede, G.; Roth, M. M. *J. Biomed. Opt.* **2018**, *23*, 1−11.
(267) Dinish, U. S.; Balasundaram, G.; Chang, Y. T.; Olivo, M. *Sci. Rep.* **2015**, *4*, 4075.
(268) Kang, H.; Jeong, S.; Jo, A.; Chang, H.; Yang, J. K.; Jeong, C.; Kyeong, S.; Lee, Y. W.; Samanta, A.; Maiti, K. K.; Cha, M. G.; Kim, T. K.; Lee, S.; Jun, B. H.; Chang, Y. T.; Chung, J.; Lee, H. Y.; Jeong, D. H.; Lee, Y. S. *Adv. Healthcare Mater.* **2018**, *7*, 1700870.
(269) Brazhe, N. A.; Thomsen, K.; Lonstrup, M.; Brazhe, A. R.; Nikelshparg, E. I.; Maksimov, G. V.; Lauritzen, M.; Sosnovtseva, O. *J. Biophotonics* **2018**, *11*, No. e201700311.
(270) Chen, Y.; Liu, S.; Liu, H.; Tong, S.; Tang, H.; Zhang, C.; Yan, S.; Li, H.; Yang, G.; Zhu, D.; Wang, K.; Wang, P. *Anal. Chem.* **2019**, *91*, 9371−9375.
(271) Ji, M.; Orringer, D. A.; Freudiger, C. W.; Ramkissoon, S.; Liu, X.; Lau, D.; Golby, A. J.; Norton, I.; Hayashi, M.; Agar, N. Y.; Young, G. S.; Spino, C.; Santagata, S.; Camelo-Piragua, S.; Ligon, K. L.; Sagher, O.; Xie, X. S. *Sci. Transl. Med.* **2013**, *5*, 201ra119.
(272) Desroches, J.; Jermyn, M.; Pinto, M.; Picot, F.; Tremblay, M. A.; Obaid, S.; Marple, E.; Urmey, K.; Trudel, D.; Soulez, G.; Guiot, M. C.; Wilson, B. C.; Petrecca, K.; Leblond, F. *Sci. Rep.* **2018**, *8*, 1792.
(273) Jermyn, M.; Mercier, J.; Aubertin, K.; Desroches, J.; Urmey, K.; Karamchandiani, J.; Marple, E.; Guiot, M.-C.; Leblond, F.; Petrecca, K. *Cancer Res.* **2017**, *77*, 3942−3950.
(274) Stiebing, C.; Schie, I. W.; Knorr, F.; Schmitt, M.; Keijzer, N.; Kleemann, R.; Jahn, I. J.; Jahn, M.; Kiliaan, A. J.; Ginner, L.; Lichtenegger, A.; Drexler, W.; Leitgeb, R. A.; Popp, J. *Neurophotonics* **2019**, *6*, 1−9.
(275) Dooley, M.; Prasopthum, A.; Liao, Z.; Sinjab, F.; McLaren, J.; Rose, F.; Yang, J.; Notingher, I. *Biomed. Opt. Express* **2019**, *10*, 1678−1690.
(276) Jenkins, C. A.; Jenkins, R. A.; Pryse, M. M.; Welsby, K. A.; Jitsumura, M.; Thornton, C. A.; Dunstan, P. R.; Harris, D. A. *Analyst* **2018**, *143*, 6014−6024.
(277) Medipally, D. K. R.; Maguire, A.; Bryant, J.; Armstrong, J.; Dunne, M.; Finn, M.; Lyng, F. M.; Meade, A. D. *Analyst* **2017**, *142*, 1216−1226.
(278) Paraskevaidi, M.; Morais, C. L. M.; Halliwell, D. E.; Mann, D. M. A.; Allsop, D.; Martin-Hirsch, P. L.; Martin, F. L. *ACS Chem. Neurosci.* **2018**, *9*, 2786−2794.
(279) Patel, S. K.; Rajora, N.; Kumar, S.; Sahu, A.; Kochar, S. K.; Krishna, C. M.; Srivastava, S. *Anal. Chem.* **2019**, *91*, 7054−7062.
(280) Ryzhikova, E.; Kazakov, O.; Halamkova, L.; Celmins, D.; Malone, P.; Molho, E.; Zimmerman, E. A.; Lednev, I. K. J. *Biophotonics* **2015**, *8*, 584−596.
(281) Jenkins, C. A.; Lewis, P. D.; Dunstan, P. R.; Harris, D. A. *World J. Gastrointest. Oncol.* **2016**, *8*, 427−438.
(282) Elumalai, B.; Prakasarao, A.; Ganesan, B.; Dornadula, K.; Ganesan, S. *J. Raman Spectrosc.* **2015**, *46*, 84−93.
(283) Kerr, L. T.; Lynn, T. M.; Cullen, I. M.; Daly, P. J.; Shah, N.; O'Dea, S.; Malkin, A.; Hennelly, B. M. *Anal. Methods* **2016**, *8*, 4991−5000.
(284) Chen, G. N.; Lin, X. L.; Lin, D.; Ge, X. S.; Feng, S. Y.; Pan, J. J.; Lin, J. Q.; Huang, Z. F.; Huang, X.; Chen, R. *RSC Adv.* **2016**, *6*, 7760−7764.
(285) Chen, N.; Rong, M.; Shao, X. G.; Zhang, H.; Liu, S. P.; Dong, B. J.; Xue, W.; Wang, T. Y.; Li, T. H.; Pan, J. H. *Int. J. Nanomed.* **2017**, *12*, 5399−5407.
(286) Guo, L.; Li, Y. P.; Huang, F. R.; Dong, J.; Li, F. C.; Yang, X. H.; Zhu, S. Q.; Yang, M. X. *J. Innovative Opt. Health Sci.* **2019**, *12*, 1950003.
(287) Li, M.; Kang, J. W.; Sukumar, S.; Dasari, R. R.; Barman, I. *Chem. Sci.* **2015**, *6*, 3906−3914.
(288) Wang, Y. J.; Zong, S. F.; Li, N.; Wang, Z. Y.; Chen, B. A.; Cui, Y. P. *Nanoscale* **2019**, *11*, 2460−2467.
(289) Zhang, Y. Y.; Mi, X.; Tan, X. Y.; Xiang, R. *Theranostics* **2019**, *9*, 491−525.
(290) Santos, M. C.; Morais, C. L.; Nascimento, Y. M.; Araujo, J. M.; Lima, K. M. *TrAC, Trends Anal. Chem.* **2017**, *97*, 244−256.
(291) Beleites, C.; Neugebauer, U.; Bocklitz, T.; Krafft, C.; Popp, J. *Anal. Chim. Acta* **2013**, *760*, 25−33.
(292) Ali, N.; Girnus, S.; Roesch, P.; Popp, J.; Bocklitz, T. W. *Anal. Chem.* **2018**, *90*, 12485−12492.
(293) Schuhmacher, D.; Gerwert, K.; Mosig, A. A Generic Neural Network Approach to Infer Segmenting Classifiers for Disease-Associated Regions in Medical Images. *medRxiv* **2020**; DOI: 10.1101/2020.02.27.20028845.
(294) Bocklitz, T. Understanding of Non-linear Parametric Regression and Classification Models: A Taylor Series based Approach. In *Proceedings of the 8th International Conference on Pattern Recognition Applications and Methods*; 2019; Vol. *1*, pp 874−880 DOI: 10.5220/0007682008740880.
(295) Maier, A. K.; Syben, C.; Stimpel, B.; Würfl, T.; Hoffmann, M.; Schebesch, F.; Fu, W.; Mill, L.; Kling, L.; Christiansen, S. *Nature machine intelligence* **2019**, *1*, 373−380.
(296) Gautam, R.; Vanga, S.; Ariese, F.; Umapathy, S. *EPJ. Techniques and Instrumentation* **2015**, *2*, 8.
(297) Byrne, H. J.; Knief, P.; Keating, M. E.; Bonnier, F. *Chem. Soc. Rev.* **2016**, *45*, 1865−1878.
(298) Olmos, V.; Bedia, C.; Tauler, R. a.; de Juan, A. *Appl. Spectrosc.* **2018**, *72*, 489−500.

(299) Schulze, H. G.; Rangan, S.; Piret, J. M.; Blades, M. W.; Turner, R. F. B. *Appl. Spectrosc.* **2018**, *72*, 1322−1340.
(300) Guo, S.; Bocklitz, T.; Popp, J. u. *Analyst* **2016**, *141*, 2396−2404.
(301) McCreery, R. L. *Raman Spectroscopy for Chemical Analysis*; Wiley-Interscience, 2000; Vol. *157*.
(302) Dörfer, T.; Bocklitz, T.; Tarcea, N.; Schmitt, M.; Popp, J. *Z. Phys. Chem.* **2011**, *225*, 753.
(303) Guo, S.; Beleites, C.; Neugebauer, U.; Abalde-Cela, S.; Afseth, N. K.; Alsamad, F.; Anand, S.; Araujo-Andrade, C.; Aškrabić, S.; Avci, E.; Baia, M.; Baranska, M.; Baria, E.; Batista de Carvalho, L. A. E.; de Bettignies, P.; Bonifacio, A.; Bonnier, F.; Brauchle, E. M.; Byrne, H. J.; Chourpa, I.; Cicchi, R.; Cuisinier, F.; Culha, M.; Dahms, M.; David, C.; Duponchel, L.; Duraipandian, S.; El-Mashtoly, S. F.; Ellis, D. I.; Eppe, G.; Falgayrac, G.; Gamulin, O.; Gardner, B.; Gardner, P.; Gerwert, K.; Giamarellos-Bourboulis, E. J.; Gizurarson, S.; Gnyba, M.; Goodacre, R.; Grysan, P.; Guntinas-Lichius, O.; Helgadottir, H.; Grošev, V. M.; Kendall, C.; Kiselev, R.; Kölbach, M.; Krafft, C.; Krishnamoorthy, S.; Kubryck, P.; Lendl, B.; Loza-Alvarez, P.; Lyng, F. M.; Machill, S.; Malherbe, C.; Marro, M.; Marques, M. P. M.; Matuszyk, E.; Morasso, C. F.; Moreau, M.; Muhamadali, H.; Mussi, V.; Notingher, I.; Pacia, M. Z.; Pavone, F. S.; Penel, G.; Petersen, D.; Piot, O.; Rau, J. V.; Richter, M.; Rybarczyk, M. K.; Salehi, H.; Schenke-Layland, K.; Schlücker, S.; Schosserer, M.; Schütze, K.; Sergo, V.; Sinjab, F.; Smulko, J.; Sockalingum, G. D.; Stiebing, C.; Stone, N.; Untereiner, V.; Vanna, R.; Wieland, K.; Popp, J.; Bocklitz, T. *Anal. Chem.* **2020**, *92*, 15745−15756.
(304) Bocklitz, T. W.; Dörfer, T.; Heinke, R.; Schmitt, M.; Popp, J. *Spectrochim. Acta, Part A* **2015**, *149*, 544−549.
(305) Bocklitz, T.; Putsche, M.; Stüber, C.; Käs, J.; Niendorf, A.; Rösch, P.; Popp, J. u. *J. Raman Spectrosc.* **2009**, *40*, 1759−1765.
(306) Pomrehn, C.; Klein, D.; Kolb, A.; Kaul, P.; Herpers, R. *Chemom. Intell. Lab. Syst.* **2019**, *184*, 112−122.
(307) Guo, S.; Heinke, R.; Stöckel, S.; Rösch, P.; Popp, J. u.; Bocklitz, T. *J. Raman Spectrosc.* **2018**, *49*, 627−637.
(308) Guo, S.; Kohler, A.; Zimmermann, B.; Heinke, R.; Stöckel, S.; Rösch, P.; Popp, J. u.; Bocklitz, T. W. *Anal. Chem.* **2018**, *90*, 9787−9795.
(309) Acquarelli, J.; van Laarhoven, T.; Gerretzen, J.; Tran, T. N.; Buydens, L. M. C.; Marchiori, E. *Anal. Chim. Acta* **2017**, *954*, 22−31.
(310) Zhang, X.; Lin, T.; Xu, J.; Luo, X.; Ying, Y. *Anal. Chim. Acta* **2019**, *1058*, 48−57.
(311) Fukuhara, M.; Fujiwara, K.; Maruyama, Y.; Itoh, H. *Anal. Chim. Acta* **2019**, *1087*, 11−19.
(312) Liu, J.; Osadchy, M.; Ashton, L.; Foster, M.; Solomon, C. J.; Gibson, S. J. *Analyst* **2017**, *142*, 4067−4074.
(313) Kirchberger-Tolstik, T.; Pradhan, P.; Vieth, M.; Grunert, P.; Popp, J.; Bocklitz, T. W.; Stallmach, A. *Anal. Chem.* **2020**, *92*, 13776−13784.
(314) Ho, C.-S.; Jean, N.; Hogan, C. A.; Blackmon, L.; Jeffrey, S. S.; Holodniy, M.; Banaei, N.; Saleh, A. A. E.; Ermon, S.; Dionne, J. *Nat. Commun.* **2019**, *10*, 4927.
(315) Chernavskaia, O.; Bocklitz, T.; Meyer, T.; Vogler, N.; Akimov, D.; Heuke, S.; Guo, S.; Heintzmann, R.; Popp, J. u. *J. Chemom.* **2017**, *31*, e2901.
(316) Yarbakht, M.; Pradhan, P.; Köse-Vogel, N.; Bae, H.; Stengel, S.; Meyer, T.; Schmitt, M.; Stallmach, A.; Popp, J.; Bocklitz, T. W.; Bruns, T. *Anal. Chem.* **2019**, *91*, 11116−11121.
(317) Rodner, E.; Bocklitz, T.; von Eggeling, F.; Ernst, G.; Chernavskaia, O.; Popp, J.; Denzler, J.; Guntinas-Lichius, O. *Head Neck* **2019**, *41*, 116−121.
(318) Guo, S.; Bocklitz, T.; Neugebauer, U.; Popp, J. u. *Anal. Methods* **2017**, *9*, 4410−4417.

https://doi.org/10.1021/acs.analchem.1c03235
Anal. Chem. 2022, 94, 86−119